APPROVAL SHEET

Title of Dissertation: Satellite simulator studies of the impact of cloud inhomogeneity on passive cloud remote sensing retrievals

Name of Candidate: Daniel J. Miller
Doctor of Philosophy, 2017

Dissertation and Abstract Approved: Zhibo Zhang

Dr. Zhibo Zhang
Associate Professor
Department of Physics

Date Approved: 11/3/2017

Daniel J. Miller

Contact Information

UMBC Physics Dept.
1000 Hilltop Circle
Baltimore, Maryland 21250

email: DJ-Miller@UMBC.edu

Education

Michigan Technological University, Houghton, Michigan USA

Bachelor of Science, Physics, 2011

University of Maryland, Baltimore County, Baltimore, Maryland USA

Master of Science, Atmospheric Physics, 2013
Doctor of Philosophy, Atmospheric Physics, 2017

Research Interests

cloud and aerosol remote sensing, cloud and aerosol microphysics, polarized radiative transfer, global climate change, and aerosol-cloud Physical and radiative interactions.

Research Experience

Undergraduate Research Experience

Summer Research Project *2009*
Advisor: Dr. Raymond Shaw, Ph.D. `rashaw@mtu.edu`
Designed and built a prototype magnified digital in-line holography instrument for in situ measurement of cloud droplet positions and instantaneous velocities. Conducted a three week field campaign on a mountain in Germany.

Senior Research Project *2009 – 2010*
Advisor: Dr. Raymond Shaw, Ph.D. `rashaw@mtu.edu`
Applied magnified digital in-line holography methods to study of brownian motion of 2μm spherical glass particles in a 1mm deep cylindrical test cell. Depth resolution of the holograms after magnification was insufficient to draw any conclusions regarding brownian motion in three dimensions although two dimensional tracking was still possible.

Graduate Research Experience

Graduate Research Assistant *2012 – 2017*
Advisor: Dr. Zhibo Zhang, Ph.D. `zhibo.zhang@umbc.edu`
Studied the scattering of from atmospheric particles (aerosols and clouds droplets/ice) for applications in remote sensing. Using a satellite simulator, built by coupling radiative transfer models with the ouput of a cloud LES model we evaluated the cloud microphysical retrieval capabilities and limitations of satellite instruments such as POLDER, MODIS and future atmospheric remote sensing instruments.

Teaching Experience

Undergraduate Teaching Assistant *2007-2011*
Electricity and Magnetism Lab for Engineers, Introductory Physics Lab for Physics Majors, Optics Lab, Modern Physics Lab
Graduate Teaching Assistant *2011-2012* Electricity and Magnetism for Honors Students and Majors

Publications

- Miller, D. J. (2009), Thermo and Fluid Dynamics of a Homemade Lava Lamp, NASA Practical Uses of Math and Science, <https://pumas.gsfc.nasa.gov/files/05_05_09_1.pdf>
- Miller, D. J., Z. Zhang, A. S. Ackerman, S. Platnick, and B. A. Baum (2016), The impact of cloud vertical profile on liquid water path retrieval based on the bispectral method: A theoretical study based on large-eddy simulations of shallow marine boundary layer clouds, J. Geophys. Res., 121(8), 4122-4141, doi:10.1002/2015JD024322.
- Miller, D. J., Zhang, Z., Platnick, S., Ackerman, A. S., Werner, F., Cornet, C., and Knobelspiesse, K.: Comparisons of bispectral and polarimetric cloud microphysical retrievals using LES-Satellite retrieval simulator, Atmos. Meas. Tech. Discuss., doi:10.5194/amt-2017-325, in review, 2017.

Recent Presentations

- Miller, D. J., Z. Zhang, S. Platnick, A. S. Ackerman, C. Cornet, and B. A. Baum (2013), Exploring the effects of cloud vertical and horizontal structure on cloud microphysics retrievals based on polarized reflectances, presented at the 2013 AGU Fall Meeting, San Francisco, doi:10.13140/2.1.2948.7043.
- Miller, D. J., Z. Zhang, S. Platnick, A. S. Ackerman (2014), An assessment of cloud liquid water path and droplet number concentration retrievals derived from MODIS-like observations: Comparison with large-eddy simulation (LES) and implications for aerosol indirect effects, presented at the AMS Cloud Physics and Atmospheric Radiation Joint Meeting, Boston, doi:10.13140/2.1.1343.0727.
- Miller, D. J., Z. Zhang, S. Platnick, A. S. Ackerman (2014), Cloud vertical structure and the impact of MODIS liquid water path retrieval assumptions: Developing a theoretical framework and evaluating retrievals using large-eddy simulations, presented at the 2014 AGU Fall Meeting, San Francisco, doi:10.13140/2.1.4882.3363.
- Miller, D. J., Z. Zhang, C. Cornet, S. Platnick, A. S. Ackerman (2015), An Exploration of 3-D Radiative Effects on Polarimetric Cloud Microphysical Retrievals: Results from idealized case studies and an LES satellite simulator, presented at the 2015 AGU Fall Meeting, San Francisco, doi:10.13140/RG.2.1.1865.7361.
- Miller, D. J., Z. Zhang, A. S. Ackerman, S. Platnick (2016), Comparing Polarimetric and Spectral Retrievals of Cloud Properties: Lessons from LES cloud satellite simulator studies, presented at the 2016 AGU Fall Meeting,

San Francisco, doi:10.13140/RG.2.2.20149.68321.

Awards

- AAPT Outstanding Teaching Assistant - 2008
- NASA Earth and Space Science Fellowship (NESSF) 2014-2017
- NASA Postdoctoral Program Fellowship (NPP) 2017-

ABSTRACT

Title of dissertation: SATELLITE SIMULATOR STUDIES OF THE IMPACT OF CLOUD INHOMOGENEITY ON PASSIVE CLOUD REMOTE SENSING RETRIEVALS

Daniel J. Miller, Doctor of Philosophy, 2017

Dissertation directed by: Professor Zhibo Zhang
Department of Physics

Satellite cloud remote sensing provides us the opportunity to study the spatial and temporal distributions of marine boundary layer clouds, as well as their connections with environments on a global scale. However, cloud remote sensing is not without difficulties; retrievals require numerous simplifying assumptions, placing limits on our understanding of cloud processes. Passive remote sensing retrievals often assume that clouds are homogeneous slabs, when in reality, these clouds often have complex inhomogeneous vertical and horizontal structures. Enhancing our understanding of how cloud inhomogeneity influences passive cloud remote sensing requires comparison between cloud retrievals and the underlying cloud properties. In observational data-sets this can become problematic, as it is difficult to compare satellite and airborne measurements because they have both different observed spatial scales and sensitivities to cloud properties. To avoid these complications, this work is based on a satellite retrieval simulator – a Large-Eddy Simulation (LES) cloud model coupled to radiative transfer and retrieval algorithms. The LES-satellite

simulator can be used to study the source of retrieval biases. It provides the underlying realistic cloud structure as a reference, informing conclusions about its impact on various cloud retrieval methods. In the first step we focus on cloud vertical profile, finding that the selection of appropriate vertical profile assumptions for the retrieval of cloud liquid water path. Confirming previous studies, drizzle and cloud top entrainment of dry air are identified as physical features that bias liquid water path retrievals away from adiabatic and toward homogeneous profile assumptions. The mean bias induced by drizzle-influenced profiles was shown to be on the order of 5–10 $\mathrm{g/m^2}$. In contrast, the influence of cloud top entrainment was found to be smaller by about a factor of 2. A theoretical framework is also developed to explain variability in LWP retrievals by introducing modifications to the adiabatic effective radius profile. The second step focuses on horizontal inhomogeneity and exploring a comparison of both the bispectral and polarimetric cloud retrieval techniques. Using the satellite retrieval simulator we are able to verify that at high spatial resolution (50 m) the bispectral and polarimetric retrievals are indeed highly correlated with one another. The small differences at high spatial resolution can be attributed to different sensitivity limitations of the two retrievals. In contrast, a systematic difference between the two effective radius retrievals emerges at coarser resolution. This bias largely stems from differences related to sensitivity of the two retrievals to unresolved inhomogeneities in effective variance and optical thickness. The influence of coarse angular resolution is found to increase uncertainty in the polarimetric effective radius retrieval, but generally maintains a constant mean value. The third study focuses on 3-D radiative effects influencing both total and polarized

reflectances and retrievals. Comparisons between the 1-D and 3-D reflectances are made in order to study horizontal photon transfer and radiative smoothing. We find noticeable differences between the total and polarized reflectance 3-D effects, with radiative smoothing and roughening occurring at different scales as well as viewing geometry dependence. Despite these apparently strong 3-D effects on polarized reflectances, the polarimetric retrieval is robust to the influence of 3-D effects – with only sub-micron biases in the retrieval of effective radius.

SATELLITE SIMULATOR STUDIES OF THE IMPACT OF CLOUD INHOMOGENEITY ON PASSIVE CLOUD REMOTE SENSING RETRIEVALS

by

Daniel J. Miller

Dissertation submitted to the Faculty of the Graduate School of the
University of Maryland, Baltimore County in partial fulfillment
of the requirements for the degree of
Doctor of Philosophy
2017

Advisory Committee:
Professor Zhibo Zhang, Advisor
Professor Vanderlei Martins
Professor Pengwang Zhai
Professor Markos Georganopoulos
Dr. Steven Platnick

Acknowledgments

I owe my gratitude to all the people who have made this dissertation possible and because of whom my graduate experience has been one that I will cherish forever. First and foremost I'd like to thank my advisor, Professor Zhibo Zhang for providing me the opportunity to work on challenging and extremely interesting projects over the past six years. Without his enthusiastic support I would not be where I am today. It has been a pleasure to work with and learn from such an extraordinary individual. I would also like to thank each of my committee members, who provided extensive feedback on my research direction throughout my time at UMBC. I am also indebted to the coauthors of my first paper, their guidance through my first foray into the scientific writing process proved invaluable.

My colleagues at UMBC have enriched my graduate life in many ways and deserve a special mention. Members of my research group, ACROS, for helpful and productive discussions. In particular I want to highlight the significant research support I received from Frank Werner and Chamara Rajapakshe. Their support and feedback helped to hone and focus the presentation of my research results. The support of my fellow graduate students, including Matthew Margotta, Edward Strobach, Barry Baker, Roy Prouty, and Kyle Cox to name a few. The welcoming graduate student community at UMBC, which provided a fostering environment that allowed me to develop my leadership skills by participating in the Graduate Student Association. Without the travel funding provided by the Graduate Student Association I would not have had numerous opportunities to share my research with the community and establish my reputation.

I owe my deepest thanks to my family, for calling me almost every day during the final weeks of dissertation writing and making sure that I felt supported. In addition, I would also like to recognize the support and kindness of all of the friends I have made here in Baltimore, which I now proudly call home.

Additionally I would like to acknowledge to support from the NASA Earth and Space Science fellowship program, which allowed me to pursue these research questions and helped me develop my proposal writing skills. This work also would not have been possible without the computational resources of the UMBC High Performance Computing facility overseen by Dr. Matthias Gobbert.

Table of Contents

List of Tables

List of Figures

List of Abbreviations

	General Abbreviations
MBL cloud	Marine Boundary Layer cloud
TOA	Top of Atmosphere
BOA	Bottom of Atmosphere
ext	Extinction
scat	Scattering
pol	Polarized or Polarimetric
unpol	Unpolarized
IPA	Independent Pixel Approximation
PPA	Plane-Parallel Approximation
LUT	Look-Up Table
LES	Large-Eddy Simulation
2WT	Two-way Transmittance
SS	Single-Scattering
PSD	Power Spectral Density
NASA	National Aeronautics and Space Administration
ESA	European Space Agency
	Cloud Microphysical Properties
DSD	Droplet Size Distribution
r_e	Effective Radius (μm)
v_e	Effective Variance (unitless)
k	Dispersion of the Droplet Size Distribution
LWC	Liquid Water Content (g/m^3)
LWP	Liquid Water Path (g/m^2)
	Cloud Optical Properties
I	Total Reflectance (unitless)
I_{pol}	Polarized Reflectance (unitless)
τ	Cloud Optical Depth anchored to $\lambda = 0.865\,\mu$m (unitless)
τ_{tot}	Cloud Optical Thickness anchored to $\lambda = 0.865\,\mu$m (unitless)
$-P_{12}$	Polarized Phase Function (unitless)
VNIR	Visible to Near Infrared (spectral range)
SWIR	Shortwave Infrared (spectral range)

	Satellite Instruments
MODIS	Moderate Resolution Imaging Spectro-radiometer
NPP VIIRS	National Polar-orbiting Partnership Visible Infrared Imaging Radiometer Suite
SEVIRI	Spinning Enhanced Visible and Infrared Imager
POLDER	Polarization and Directionality of Earth Reflectance
APS	Aerosol Polarimetry Sensor
MAIA	Multi-Angle Imager for Aerosols
HARP	Hyper-angular Rainbow Polarimeter
	Airborne Instruments
RSP	Research Scanning Polarimeter
AirMSPI	Airborne Multi-angle Spectro-Polarimetric Imager
AMS	Autonomous Modular Sensor
	Field Campaigns
DYCOMS-II	Dynamics and Chemistry of Marine Stratocumulus Project II
ATEX	Atlantic Trade Wind Experiment
PODEX	Polarimeter Definition Experiment
PACE	Plankton Aerosols Clouds and Ecosystems

Chapter 1: Introduction

1.1 Why do marine boundary layer clouds matter?

Marine boundary layer (MBL) clouds constantly cover approximately one-fifth of the Earths ocean surface [*Warren et al.*, 1988; *Wood*, 2012]. These clouds reflect significantly more sunlight than the dark underlying ocean and therefore have a strong cooling effect on the climate system [*Klein and Hartmann*, 1993]. Moreover, the prevalence of drizzle in MBL clouds according to recent CloudSat observations suggesting they play an important role in both the water and energy cycles by contributing precipitation and latent heat respectively [*Kubar and Hartmann*, 2009; *Behrangi et al.*, 2012]. Additionally, as demonstrated by ship tracks, MBL clouds are susceptible to changes in aerosol concentrations, indicating a sensitivity to aerosol indirect effects [*Twomey*, 1977; *Oreopoulos and Platnick*, 2008].

All of the facts above suggest that MBL clouds have an important role in the climate system. However, at present we only have a limited understanding of this role. Our ability to simulate MBL clouds and their interactions with environment factors in climate models is awkwardly inadequate [*Zhang et al.*, 2005]. As a result, the interactions between aerosols and clouds have been repeatedly identified as one of the primary sources of uncertainty in estimates of the human impact on climate

change [*IPCC*, 2013]. It is not just the magnitude of the MBL cloud feedback which is unknown, but even whether they contribute to or dampen the effects of global warming [*Bony and Dufresne*, 2005]. There is a pressing need for a better understanding of the varied impacts of MBL clouds on both the present climate system and their role in climate change.

1.2 Satellite Remote Sensing

Providing a better scientific picture of the impact of MBL clouds on climate requires long-term continuous observations of the spatial and temporal distributions of MBL clouds, as well as their connections with environments on a global scale. At present, satellite-based cloud remote sensing is the only means to achieve such observations. Many remote sensing techniques have been developed over the past several decades for monitoring cloud properties from both orbital and sub-orbital instruments [*Stephens and Kummerow*, 2007]. Among these techniques, the bispectral reflectance method of *Nakajima and King* [1990] and the multi-angular polarimetric method *Bréon and Goloub* [1998] are two of the most widely used methods for remote sensing of cloud optical and microphysical properties from passive satellite observations. The former is the theoretical basis for the operational algorithm for the MODIS (Moderate Resolution Spectroradiometer) cloud product and the latter is used for retrieving the cloud droplet size of MBL clouds from POLDER (Polarization and Directionality of the Earths Reflectances) observations. For simplicity hereafter we refer these two methods as the spectral and polarimetric methods re-

spectively. The MODIS and POLDER cloud products have been utilized to address numerous important open research questions: aerosol-cloud interactions (e.g., [*Kaufman et al.*, 2005; *Quaas and Boucher*, 2005; *Lebsock et al.*, 2008; *Jiang*, 2009; *Quaas et al.*, 2009]), radiative effects of aerosols (e.g., [*Wilcox*, 2012; *Costantino and Breon*, 2013a; *Meyer et al.*, 2013; *Zhang et al.*, 2013; *Min and Zhang*, 2014]), validation of cloud parameterization schemes in climate models (e.g., [*Donner et al.*, 2011; *Jiang et al.*, 2012; *Kay et al.*, 2012; *Pincus et al.*, 2012]), and the cloud feedback to climate change (e.g., [*Zhou et al.*, 2013]) to list a few. The wide use and broad impact of these cloud products make it important to understand their limitations and uncertainties.

1.3 Limitations of Passive Satellite Remote Sensing

One of the greatest issues facing passive remote sensing is that realistic cloud structure can be significantly inhomogeneous. This creates difficulties for remote sensing techniques without prior information about such inhomogeneity. Realistic 3-D cloud structure can be complex, with both vertical and horizontal variability driven by a variety of physical processes. However, most cloud retrieval algorithms cannot account for the actual cloud structure and instead assume various cloud homogeneity conditions. To that end, passive retrievals typically assume that all cloudy pixels are homogeneous, plane-parallel, and infinitely homogeneous slabs. This assumption leads to numerous consequences for the sensitivity of remotely sensed cloud properties to the presence of realistically inhomogeneous clouds.

For (shortwave) passive satellite remote sensing cloud vertical inhomogeneity can cause issues because it is difficult to probe cloud properties in specific layers or volumes of a cloud. This difficulty stems from the fact that light is scattered throughout the vertical extent of the cloud and thus the information from particular layers is vertically averaged. The particulars of this vertical averaging or smoothing depends vertical variability of the absorption and scattering properties of cloud water droplets. This leads some cloud retrievals to make assumptions about the cloud vertical profile in order to obtain cloud properties in specific layers (like cloud top) or column properties.

Cloud horizontal inhomogeneity can cause a number of difficulties as well. At high spatial resolutions, this horizontal variability can lead to significant horizontal radiative flux, violating the plane-parallel infinite assumption. These situations can produce artifacts referred to as "3-D radiative effects", which are discrepancies in the observed reflectances and their retrievals. At coarse spatial resolutions, biases can be induced by unresolved, inhomogeneous or broken clouds and surface contamination. As a consequence of these two extremes, there is a always a resolution trade off. High resolutions are susceptible to 3-D effects, whereas low resolution reflectances do not clearly resolve the cloud scale are susceptible to unresolved inhomogeneity biases.

1.4 Objectives and Significance of this Study

Enhancing our understanding of how cloud inhomogeneity influences passive cloud remote sensing requires comparison between cloud retrievals and the underlying cloud properties. In observational data sets this can become problematic – it is difficult to compare satellite and *in-situ* airborne measurements because they have both different observed spatial scales and sensitivities to cloud properties [*Henrich et al.*, 2010]. To avoid these complications, this work is based on a satellite retrieval simulator - an LES cloud model coupled to radiative transfer and retrieval algorithms. The LES-satellite simulator can be used to study the source of retrieval biases, providing the underlying realistic cloud structure as a reference, informing conclusions about its impact on various cloud retrieval methods. These results can then be used in future observational studies, providing guidance on the interpretation of various cloud properties.

The LES-satellite simulator will allow us to investigate the following scientific questions:

- What impact does inhomogeneity of the cloud vertical profile have on both spectral and polarimetric-based cloud property retrievals?
- How do the bispectral and polarimetric retrievals compare to one another and how does cloud inhomogeneity influence differences between these retrievals?
- How do cloud horizontal inhomogeneity and 3-D radiative effects impact both the total and polarized reflectances, and how do these impacts influence the

bispectral and polarimetric retrievals?

The structure of this dissertation is as follows: In chapter 2 we provide background information about cloud optical properties, remote sensing, retrieval techniques and the satellite simulator that will used throughout this work. Then in chapter 3 we use the passive cloud remote sensing simulator to explore the impact of cloud vertical profile assumptions on passive retrievals of cloud liquid water path. The focus of chapter 4 is on the use of the satellite simulator to compare bispectral and polarimetric cloud remote sensing techniques. Within the framework of a simulator study we can isolate the influence of differences in retrieval sensitivity, spatial and angular resolution. Finally, in chapter 5 we present case studies of 3-D effects in total and polarized reflectances and their influence on cloud microphysical retrievals.

Chapter 2: Background and Theory

2.1 Cloud Microphysics and Optical Properties

2.1.1 Cloud Droplet Size Distribution

The cloud droplet size distribution (DSD) is an important microphysical property of liquid-phase clouds. Given the cloud water content, it largely determines the shortwave radiative effects of clouds [*Twomey*, 1977]. It also plays a critical role in cloud-precipitation processes [*Pruppacher and Klett*, 1978]. As a result, anthropogenic perturbation to the DSD could lead to a variety of cloud property changes with significant climate implications [*Lohmann et al.*, 2007]. Typical MBL clouds have been observed to have a cloud droplet number concentration (N_0, CDNC) on the order of a few tens to hundreds of droplets per cm^3, depending on availability of condensation nuclei and meteorological conditions [*Martin et al.*, 1994; *Miles et al.*, 2000]. The CDNC is usually not mono-disperse, with droplet sizes varying throughout the cloud due to a number of size dependent droplet growth, dissipation, and precipitation processes. Cloud droplet radii range from a few μm to tens of μm. In satellite remote sensing cloud droplet size distributions (DSD) are often described using theoretical distributions that fit well with *in situ* observations [*Deirmendjian*,

1964; *Tampieri and Tomasi*, 1976], in addition to being mathematically convenient. To that end, a popular theoretical DSD is the gamma distribution proposed by *Hansen and Travis* [1974][1]:

$$N(r; r_e, v_e) = N_0 C r^{(1-3v_e)/v_e} \exp\left[-\frac{r}{r_e v_e}\right], \tag{2.1}$$

$$C \equiv \left((r_e v_e)^{-2+1/v_e}\, \Gamma\left[(1-2v_e)/v_e\right]\right)^{-1}, \tag{2.2}$$

where the independent variable r is the cloud droplet radius, $N(r)$ is the droplet size distribution, N_0 is the droplet number concentration, and C is the distribution normalization constant defined in 2.2, where Γ is the gamma-function. Note that throughout this paper, the fully normalized form of this distribution (i.e., without N_0) will be written as $n(r)$. The two gamma-distribution parameters are the effective radius (r_e) and the effective variance (v_e), defined mathematically in 2.3 and 2.4.

$$r_e = \frac{\int_0^\infty r^3 n(r; r_e, v_e) dr}{\int_0^\infty r^2 n(r; r_e, v_e) dr}, \tag{2.3}$$

$$v_e = \frac{1}{r_e^2} \frac{\int_0^\infty (r - r_e)^2 r^2 n(r; r_e, v_e) dr}{\int_0^\infty r^2 n(r; r_e, v_e) dr}. \tag{2.4}$$

Which can also be conveniently recast in terms of moments of the DSD itself:

$$r_e = \frac{\langle r^3 \rangle}{\langle r^2 \rangle}, \tag{2.5}$$

$$v_e = \frac{\langle r^4 \rangle \langle r^2 \rangle}{\langle r^3 \rangle^2} - 1, \tag{2.6}$$

[1]The gamma distribution specifically describes a non-precipitating cloud droplet distribution. Further modifications need to be made to this distribution to include the effects of precipitation.

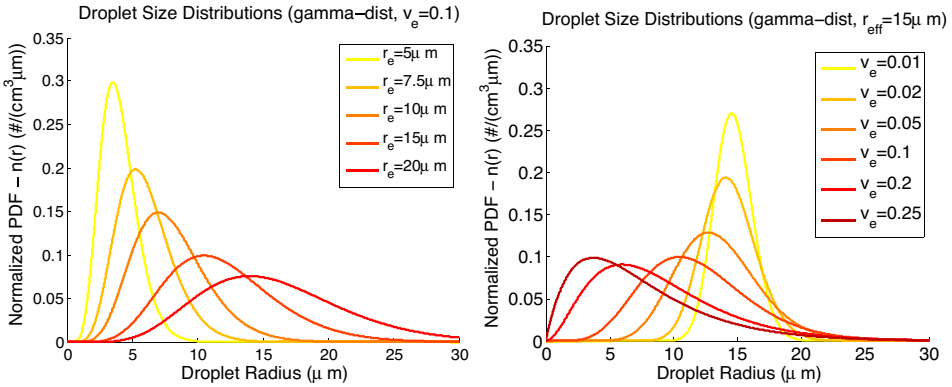

Figure 2.1: The gamma-distribution (PDF) of cloud droplets under various r_e and v_e conditions. In (a) the effective radius is varied for a constant effective variance of 0.1. A fixed effective radius of 15 μm and varied effective variances is depicted in (b). Neither one of these distributions parameters describe "the peak or "the width of the distribution alone.

However, in a practical sense the value of r_e influences the median radius as well as the broadness of the tail of the distribution. Whereas the value of v_e also influences the broadness of the tail and the asymmetry of the distribution. This is clearly demonstrated in Figure 2.1. This distribution also has some interesting and important mathematical properties, in particular the moments of the normalized gamma distribution are useful to state:

$$\left\langle r^1 \right\rangle = r_e - 2r_e v_e \,, \tag{2.7}$$

$$\left\langle r^2 \right\rangle = r_e^2 \left(v_e - 1\right)\left(2v_e - 1\right) \,, \tag{2.8}$$

$$\left\langle r^3 \right\rangle = r_e^3 \left(v_e - 1\right)\left(2v_e - 1\right) \,, \tag{2.9}$$

$$\left\langle r^4 \right\rangle = r_e^4 \left(v_e - 1\right)\left(2v_e - 1\right)\left(v_e + 1\right) \,, \tag{2.10}$$

$$\left\langle r^n \right\rangle = \left(r_e v_e\right)^n \frac{\Gamma\left[n + \frac{1}{v_e} - 2\right]}{\Gamma\left[\frac{1}{v_e} - 2\right]} \,. \tag{2.11}$$

The relationships between r_e, v_e, and these various distribution moments are useful for creating simple relationships between physical and optical properties of a cloud. For example the mass of liquid water in a parcel of air is expressed in terms of Liquid Water Content (LWC), with units of gm^{-3}. For a known size distribution it is possible to define the LWC in terms of the droplet volume and density of liquid water. The same expression can also be recast in terms of the effective radius,

$$\mathrm{LWC} \equiv \frac{4}{3}\pi\rho_l \int_0^\infty r^3 N(r)\mathrm{d}r\,, \tag{2.12}$$

$$\mathrm{LWC} = \frac{4}{3}\pi\rho_l r_e \int_0^\infty r^2 N(r)\mathrm{d}r\,. \tag{2.13}$$

In addition to the LWC, it is also common to define the dispersion of the DSD (k) which is used as a conversion factor, relating the droplet volume radius ($r_v = \langle r^3\rangle^{1/3}$) to the effective radius [*Brenguier et al.*, 2011],

$$k \equiv \frac{\langle r^3\rangle}{r_e^3} = (v_e - 1)\,(2v_e - 1)\,. \tag{2.14}$$

2.1.2 Optical Properties of Cloud Droplets and Clouds

The optical properties of individual cloud droplets can be obtained from first principle applications of Maxwell's equations for the interaction of a plane wave with spherical droplets. A general analytic solution to this problem for a dielectric sphere of size parameter ($X \equiv (2\pi r)/\lambda$) with real ($\tilde{n}_r(\lambda)$) and complex refractive index ($\tilde{n}_c(\lambda)$) was obtained by *Mie* [1908][2]. The resulting series solutions for the optical properties of single droplets are all defined on pg. 79-80 of *Wendisch and Yang* [2012]. The numerical solution to these equations is non-trivial, and an efficient and popular algorithm for obtaining these scattering properties was developed through the efforts of *Wiscombe* [1979].

Using this numerical solution results in the following optical properties: $Q_{\text{ext}}(X)$, the extinction efficiency (the fractional area of the beam both absorbed or scattered); $Q_{\text{scat}}(X)$, the scattering efficiency (the fractional area of the incident beam scattered). Additionally, it is common to express the absorption properties using the single-scattering albedo ($\omega = Q_{\text{scat}}/Q_{\text{ext}}$), where values closer to 1 indicate significant scattering and smaller values indicate increasing absorption. In addition to the above properties, the angular distributions of scattered light are also obtained in the form of the amplitude scattering matrix elements, S_{ij}. The scattering matrix is used to describe how the intensity and polarization state of light is scattered into different directions. It is conventional to normalize the amplitude scattering

[2]This problem has a vast scientific history, despite often being dubbed solely "Mie Theory" [*Logan*, 1965]. As noted by Warren Wiscombe: "[It is] by an odd twist of fate, [that] Mie's name has come to be exclusively associated with the problem; we shall adhere to this convention, but with full awareness that a misnomer is involved." [*Wiscombe*, 1979]

matrix with respect to the scattering cross section, converting them into phase matrix elements, P_{ij}, which describe the angular probability density function (PDF) of scattered light.

The cloud DSD is not monodisperse, so for these optical properties to appropriately represent the scattering in a cloud we need to account for this size variability. To accomplish this we compute an scattering and extinction cross section weighted averages of these single size properties to obtain bulk optical properties,

$$Q_{\text{scat,blk}}\left(r_e, v_e, \lambda\right) = \frac{\int_0^\infty \pi r^2 \omega\left(r,\lambda\right) Q_{\text{ext}}(r,\lambda) n(r) \mathrm{d}r}{\int_0^\infty \pi r^2 (r,\lambda) n(r) \mathrm{d}r}, \tag{2.15}$$

$$Q_{\text{ext,blk}}\left(r_e, v_e, \lambda\right) = \frac{\int_0^\infty \pi r^2 Q_{\text{ext}}\left(r,\lambda\right) n(r) \mathrm{d}r}{\int_0^\infty \pi r^2 n(r) \mathrm{d}r}, \tag{2.16}$$

$$P_{ij,\text{blk}}\left(\Theta, r_e, v_e, \lambda\right) = \frac{\int_0^\infty \pi r^2 \omega(r,\lambda) Q_{\text{ext}}\left(r,\lambda\right) P_{ij}\left(\Theta, r_e, v_e, \lambda\right) n(r) \mathrm{d}r}{\int_0^\infty \pi r^2 \omega(r,\lambda) Q_{\text{ext}}\left(r,\lambda\right) n(r) \mathrm{d}r}. \tag{2.17}$$

In addition to size, passive remote sensing techniques are sensitive across spectral band according to a spectral response function (SRF) as well as the wavelength distribution of the incident source (i.e., solar blackbody Planck function). The SRF, and the solar source function (SSF) are then convoluted and re-normalized to create a spectral weighting function, $f(\lambda)$, that is used to create the bulk optical

properties observed by an instrument:

$$\bar{Q}_{\text{scat}}\left(r_e, v_e, \lambda_{\text{band}}\right) = \int_0^\infty Q_{\text{scat,blk}}(r,\lambda) f(\lambda) \mathrm{d}\lambda \,, \tag{2.18}$$

$$\bar{Q}_{\text{ext}}\left(r_e, v_e, \lambda_{\text{band}}\right) = \int_0^\infty Q_{\text{ext,blk}}(r,\lambda) f(\lambda) \mathrm{d}\lambda \,, \tag{2.19}$$

$$\bar{P}_{ij}\left(\Theta, r_e, v_e, \lambda_{\text{band}}\right) = \frac{\int_0^\infty P^{\text{num.}}_{ij,\text{blk}}\left(\Theta, r_e, v_e, \lambda\right) f(\lambda) \mathrm{d}\lambda}{\bar{Q}_{\text{scat}}} \,. \tag{2.20}$$

Note that $P^{\text{num.}}_{ij,\text{blk}}$ is simply defined as the numerator of equation 2.17. These optical properties make up the microphysical optical property library used throughout this work. Similar to the optical properties below, the cloud DSD information that can be obtained from remote sensing is dependent on the scattering cross section and not directly on the cloud droplet sizes. Thus the droplet size that scattered light is sensitive to can be described as an scattering cross section weighted size, known as the mean radius for scattering,

$$r_{\text{scat}} = \frac{\int_{\lambda_0}^{\lambda_f} \int_0^\infty r \left[Q_{\text{scat}}\left(r,\lambda\right) r^2\right] n(r; r_e, v_e) \mathrm{d}r \, f(\lambda) \mathrm{d}\lambda}{\int_{\lambda_0}^{\lambda_f} \int_0^\infty \left[Q_{\text{scat}}\left(r,\lambda\right) r^2\right] n(r; r_e, v_e) \mathrm{d}r \, f(\lambda) \mathrm{d}\lambda} \,, \tag{2.21}$$

$$v_{\text{scat}} = \frac{1}{r^2_{\text{scat}}} \frac{\int_{\lambda_0}^{\lambda_f} \int_0^\infty \left(r - r_{\text{scat}}\right)^2 \left[Q_{\text{scat}}\left(r,\lambda\right) r^2\right] n(r; r_e, v_e) \mathrm{d}r \, f(\lambda) \mathrm{d}\lambda}{\int_{\lambda_0}^{\lambda_f} \int_0^\infty \left[Q_{\text{scat}}\left(r,\lambda\right) r^2\right] n(r; r_e, v_e) \mathrm{d}r \, f(\lambda) \mathrm{d}\lambda} \,. \tag{2.22}$$

These equations resemble the distribution definitions of r_e and v_e in Equation 2.3 and Equation 2.4, with the difference being their dependence on $Q_{\text{scat}}(r,\lambda)$. Fortunately,

due to the the large size of cloud droplets relative to the spectral bands important for passive cloud remote sensing we can approximate $\bar{Q}_{\text{ext}}(r,\lambda) \approx \text{const.} = 2$. Thus the scattering equivalent properties in Equation 2.21 and Equation 2.22 can be conveniently approximated as $r_{\text{scat}} \approx r_e$ and $v_{\text{scat}} \approx v_e$.

It is additionally important for the purposes of radiative transfer to define the optical path length, used to define the amount of light removed from the incident beam of light by scattering and absorption through radiative transfer. This optical path is usually defined relative to a vertically oriented coordinate system simply for geometric convenience, resulting in the optical depth,

$$\tau(z,\lambda) \equiv \int_{Z_{\text{TOA}}}^{z} \left[\int_{0}^{\infty} Q_{\text{ext}}(r,\lambda)\pi r^2 N(r,z)\mathrm{d}r \right] \mathrm{d}z\,, \tag{2.23}$$

where the optical depth is defined as being integrated from the top of atmosphere (Z_{TOA}) downward to a variable vertical depth (z). The optical depth at the bottom of the atmosphere (or the optical depth integrated throughout a particular atmospheric layer) is often redefined as the optical thickness,

$$\tau_{\text{tot}}(\lambda) \equiv \int_{Z_{\text{TOA}}}^{Z_{BOA}} \left[\int_{0}^{\infty} \bar{Q}_{\text{ext}}\pi r^2 N(r,z)\mathrm{d}r \right] \mathrm{d}z \tag{2.24}$$

Despite the dependence on wavelength, it is common to sometimes state the optical thickness and depth without denoting the wavelength or band it is "anchored" to. Unless otherwise stated, the optical depths and thicknesses discussed in this work are all anchored to a spectral band centered around $\lambda = 0.865\,\mu m$.

2.1.3 Radiative Transfer in Cloudy Atmospheres

The description of how light scatters through an optically dense medium requires us to define the radiative transfer equation (RTE). In general the radiative transfer equation (for total radiance) takes the following differential form *Thomas and Stamnes* [1999],

$$\frac{\mathrm{d}I(s,\lambda,\hat{\Omega})}{\mathrm{d}s} = -I(s,\lambda,\hat{\Omega}) + J(s,\lambda,\hat{\Omega})\,, \tag{2.25}$$

where the incident radiance I is diminished after passing through the medium along distance s in solid-angle direction Ω. The source term, J, describes how additional radiance is added into the beam direction Ω either through emission or scattering processes. In the absence of additional sources the analytical solution to this differential equation is known as the Beer-Lambert law,

$$I(s,\lambda,\hat{\Omega}) = I(s_0,\lambda,\hat{\Omega})\exp^{-\tau_s}\,, \tag{2.26}$$

where τ_s is the optical path length along path s. This optical path can also be redefined relative to the optical depth coordinate as, $\tau_s = \frac{\tau}{\mu}$, where $\mu = cos(\theta)$ and θ is an angle measured relative to the zenith.

The development a more complete representation of RTE requires the introduction of the polarization state of light. The representation of the intensity and polarization state is often conveniently expressed using the stokes vector, $\mathbf{I}$, which

decomposes a light source into different polarization angles and phase shifts [*Hansen and Travis*, 1974].

$$\mathbf{I} = \begin{bmatrix} I \\ Q \\ U \\ V \end{bmatrix} = \begin{bmatrix} I(0°, 0) + I(90°, 0) \\ I(0°, 0) - I(90°, 0) \\ I(45°, 0) - I(135°, 0) \\ I(45°, \pi/2) - I(135°, \pi/2) \end{bmatrix}. \tag{2.27}$$

Where I represents the total intensity, while Q and U each represent the intensity of orthogonal linear polarization states, and V is the intensity of the circularly polarized light. For example, fully polarized light and unpolarized light can be decomposed as follows.

$$I_{\text{pol}} = \sqrt{Q^2 + U^2 + V^2} \tag{2.28}$$

$$I_{\text{unpol}} = I - \sqrt{Q^2 + U^2 + V^2} \tag{2.29}$$

For shortwave radiative transfer in a conservative scattering medium (i.e. elastic scattering) the vector RTE is,

$$\mu \frac{\mathrm{d}\mathbf{I}(\lambda, \hat{\Omega})}{\mathrm{d}\tau} = -\mathbf{I}(\lambda, \hat{\Omega}) + \frac{\omega}{4\pi} \int_{4\pi} \mathbf{L}(-\sigma_f)\mathbf{P}(\lambda, \hat{\Omega}', \hat{\Omega})\mathbf{L}(-\sigma_i)\mathrm{I}(\lambda, \hat{\Omega}')\mathrm{d}\hat{\Omega}'. \tag{2.30}$$

The first term of this equation represents the portion of the radiance remaining in the beam after passing through the optical path. The integral term describes the scattering of light from all directions (Ω') scattered into the direction (Ω). Note that

the matrix, $\mathbf{L}(-\sigma_i)$ is a rotation matrix intended to rotate the orientation of the polarization state vector $\mathbf{I}$ from the observation plane into the scattering plane where the phase matrix $\mathbf{P}$ describes scattering. After the scattering plane transformation, the result is rotated back to observation plane with another rotational transformation using $\mathbf{L}(-\sigma_i)$. In general the form of this equation can take on a number of additional terms depending on boundary conditions and methods of obtaining a solution (chapter 6 of *Thomas and Stamnes* [1999]). Generalizable analytical solutions to this equation are difficult to obtain except under idealized and highly symmetric conditions [*van de Hulst*, 1980]. Typically the RTE is solved via various different numerical methods (chapter 8 of *Thomas and Stamnes* [1999]). Numerous numerical approaches exist to solve this problem (chapter 7 of *Thomas and Stamnes* [1999]). Several different RTE solvers are used throughout this work. Each of them will be discussed in section 2.4.

2.2 Cloud Inhomogeneity

2.2.1 Inhomogeneity of Cloud Vertical Profile

The vertical profile of MBL clouds is a remarkable macrophysical cloud feature due in large part because it is effectively determined by droplet growth and development processes on microphysical scales. From a remote sensing perspective the cloud vertical profile plays an important role in retrievals of cloud droplet sizes [*Platnick*, 2000] and the total amount of cloud water [*Seethala and Horváth*, 2010]. With (shortwave) passive satellite remote sensing it is difficult, if not impossible, to

probe cloud properties in very specific layers or volumes of a cloud. This difficulty stems from the fact that light is scattered throughout the vertical extent of the cloud and thus the information from particular layers is vertically averaged. The particulars of this vertical averaging or smoothing depends vertical variability of the absorption and scattering properties of cloud water droplets. Thus, it is common to recast profile properties, like the LWC profile, in terms of a column total quantities like the cloud liquid water path (LWP),

$$\text{LWP} = \int_{Z_{\text{base}}}^{Z_{\text{top}}} LWC(z)\mathrm{d}z\,, \tag{2.31}$$

$$\text{LWP} = \frac{4}{3}\pi\rho_l \int_{Z_{\text{base}}}^{Z_{\text{top}}} \left[\int_0^\infty r^3 N(r,z)\mathrm{d}r\right] \mathrm{d}z\,. \tag{2.32}$$

This equation can be further simplified by substituting in Equation 2.13 and Equation 2.23 to create relationship linking the cloud LWP with the vertical profiles of $r_e(z)$, and $\tau(z)$:

$$\text{LWP} = \frac{4}{3}\pi\rho_l \frac{1}{\bar{Q}_{\text{ext}}} \int_{Z_{\text{base}}}^{Z_{\text{top}}} r_e(z)\tau(z)\mathrm{d}z\,. \tag{2.33}$$

Note that this substitution implicitly assumes that the size parameter is sufficiently large such that $\bar{Q}_{\text{ext}} \approx$ const. $= 2$ and can be removed from the size distribution integral (refer to subsection 2.1.2). Additionally, a change of variable can be made, expressing Equation 2.33 with respect to optical depth, resulting a more convenient

relationship for the purposes of remote sensing.

$$\mathrm{LWP} = \frac{2}{3}\pi\rho_l \int_0^{\tau_{\mathrm{tot}}} r_e(\tau)\mathrm{d}\tau\,. \tag{2.34}$$

In the end, it is evident that the LWP is highly dependent on the vertical profile of $r_e(z)$ and $\tau(z)$. Typically, remote sensing techniques assume that cloud are vertically homogeneous in order to simplify cloud property retrievals [*Platnick et al.*, 2003]. Under this assumption the $r_e(\tau) = \text{const.}$ and the homogeneous LWP relationship ($\mathrm{LWP_h}$) are reduced to,

$$\mathrm{LWP_h} = \frac{2}{3}\rho_l r_e \tau_{\mathrm{tot}} \tag{2.35}$$

Beyond the simplified homogeneous cloud vertical profile, the implementation of a more realistic cloud vertical profile requires an understanding of fundamental cloud development processes. To that end, the adiabatic cloud model, which describes cloud vertical profile in terms of condensational droplet growth, could potentially introduce more realistic assumptions for some MBL cloud regimes [*Wood and Hartmann*, 2006; *Bennartz*, 2007]. Adiabatic cloud formation begins when a moist air parcel becomes supersaturated with respect to liquid water and the condensation of water vapor into the liquid phase begins. Buoyant vertical transport of warm moist parcels from the surface upward through the atmosphere drives this process [*Wallace and Hobbs*, 2006]. The buoyant parcel begins to cool adiabatically, resulting in the condensation of water vapor onto available cloud condensation nuclei (CCN). The

classic adiabatic model of cloud formation assumes that all CCN activation occurs at cloud base and thus the N_0 profile remains constant[3] throughout the adiabatic cloud vertical profile [*Boers and Mitchell*, 1994]. In-situ observations of cloud vertical profiles of $N_0(z)$ in MBL clouds have been found to support this assumption [*Slingo et al.*, 1982; *Martin et al.*, 1994; *Miles et al.*, 2000]. After droplet activation the cloudy air parcel continues to be lifted and cooled adiabatically as it rises causing droplets in the parcel to grow rapidly. This growth occurs at a rate such that the LWC of the parcel increases linearly moving upward through the column,

$$\mathrm{LWC}_{\mathrm{ad}}(z) = f\Gamma_l z\,, \tag{2.36}$$

This linear relationship is expressed in terms of the adiabatic LWC lapse rate (Γ_l, $\mathrm{g\,m^{-3}\,km^{-1}}$) and degree of adiabaticity (f , unitless). The adiabatic lapse rate can be analytically defined as in Equation 2.37 and is dependent on temperature and weakly dependent pressure [*Bennartz*, 2007]. The degree of adiabaticity introduces sub-adiabatic profiles to this definition.

$$\Gamma_l = -\frac{1}{R_v T}\frac{\mathrm{d}e_s}{\mathrm{d}T}\frac{\mathrm{d}T}{\mathrm{d}z}\,. \tag{2.37}$$

[3]This assumption also makes it possible to obtain closure in terms of the coupled relationship between the condensation rate, N_0 and r_e. By fixing N_0 the condensation rate only contributes to growth in droplet sizes.

Integrating over the vertical profile of LWC(z) from cloud base to the cloud top height (H) results in the adiabatic cloud liquid water path ($\mathrm{LWP_{ad}}$),

$$\mathrm{LWP_{ad}}(H) = \int_0^H \mathrm{LWC_{ad}}(z)dz = \frac{1}{2} f \Gamma_l H^2, \tag{2.38}$$

As the LWC increases linearly, the r_e and τ are also increasing [*Boers and Mitchell*, 1994; *Martin et al.*, 1994; *Miles et al.*, 2000; *Brenguier et al.*, 2011].

$$r_{e,\mathrm{ad}}(z) = \left(\frac{4}{3}\pi\rho_l \frac{1}{f\Gamma_l}\right)^{1/3} (kN_0)^{-1/3} z^{1/3}, \tag{2.39}$$

$$\tau_{\mathrm{ad}}(z) = \frac{3}{5}\bar{Q}_{\mathrm{ext}} \left(\frac{4}{3}\pi\rho_l \frac{1}{f\Gamma_l}\right)^{-2/3} (kN_0)^{1/3} z^{5/3}, \tag{2.40}$$

where a simplified form of $r_{e,\mathrm{ad}}(\tau)$ can be defined,

$$r_e(\tau) = r_e^{\mathrm{top}} \left(\frac{\tau_{\mathrm{tot}} - \tau}{\tau_{\mathrm{tot}}}\right)^{1/5} \tag{2.41}$$

These relationships, coupled with Equation 2.34, lead to an expression for adiabatic $\mathrm{LWP_{ad}}$ that differs from the vertically homogeneous relationships Equation 2.35 by a multiplicative factor and recast in terms of the droplet size specifically at cloud top [*Bennartz*, 2007].

$$\mathrm{LWP_{ad}} = \frac{5}{9}\rho_l r_e^{\mathrm{top}} \tau_{\mathrm{tot}} \tag{2.42}$$

It is important to note that the cloud vertical profile can also be altered as the cloud develops by precipitation and mixing processes leading to further natural variability

in observed cloud profiles. Observations of the in-situ cloud vertical profile, like those in Figure 2.2, often deviates from the predicted adiabatic cloud structure, especially near cloud top. While the overall structure of LWC in Figure 2.2(a) does appear to be linearly increasing, as indicated by the adiabatic theory, the observations have a reduced lapse rate (slope) throughout the lower region of the cloud. This cloud profile is said to be sub-adiabatic, because the amount of water condensing from vapor into the liquid phase is reduced. This reduction is presumed to be due to an overall increase in evaporation due to the mixing of dry air into the cloud. More importantly, at cloud top (Figure 2.2(c)) the discrepancies between the theoretical and observed structures become even more dramatic. This disagreement between the theoretical adiabatic cloud vertical structure and observations indicates that there are still other physical processes at play in real clouds. For example, precipitation and mixing processes could lead to more complicated cloud vertical structures. Droplets cannot grow large enough to precipitate through condensational processes alone because it becomes increasingly inefficient with increasing droplet size [*Pruppacher and Klett*, 1978; *Salby*, 1996]. Further droplet growth can occur through collisional-coalescence processes, or the growth of large droplets by colliding with and collecting other droplets. Collisional growth increases in efficiency as droplets become larger and their increased cross sectional area leads to an increased probability of colliding and collecting smaller droplets. The likely explanation for the asymmetry of droplet size distributions stems from the existence of this size dependent difference in efficiency between two growth processes [*Tampieri and Tomasi*, 1976]. Some aspects of cloud vertical structure depend on

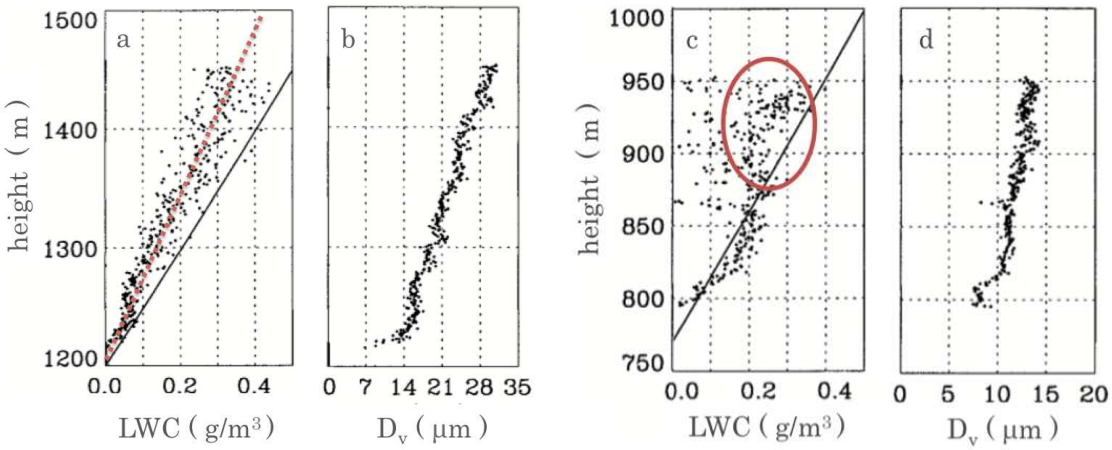

Figure 2.2: Observed profiles of $LWC(z)$ and $r_e(z)$ for two sets of observations (a,b) and (c,d). Solid lines in the LWC profiles indicate the theoretical adiabatic profile. The droplet profiles here are reported in terms of droplet volume diameter (D_v) rather than effective radius. Dashed lines are guides for the eye for features addressed in the text. (adapted from *Brenguier et al.* [2000])

turbulent mixing processes. For example, the entrainment of dry air into the moist cloudy air at cloud edges leads to evaporation of cloud droplets. The resultant effect of this mixing-evaporation process on the cloud microphysics is thought to depend on two timescales: the mixing timescale, and a reaction time-scale for the droplets to equilibrate with a new slightly drier environment [*Baker and Latham*, 1979]. Under inhomogeneous mixing conditions, mixing occurs rapidly and droplets of all sizes are evaporated indiscriminately, effectively reducing CDNC. Whereas under homogeneous mixing conditions mixing occurs slowly and the droplets have time to adjust to their environment, leaving CDNC unchanged but introducing a change in the droplet distribution due to the size dependence of the evaporation/condensation efficiency. Which of these mixing regimes dominates the entrainment of dry air at MBL cloud tops has continued to be an area of active scientific research and debate for over fifty years [*Latham and Reed*, 1977; *Baker and Latham*, 1979; *Gerber et al.*,

2005, 2013; *Beals et al.*, 2015]. More recent studies have suggested that in reality these two limiting cases are much more extreme than realistic cloud behavior which appears to fall somewhere between them. The effect of turbulent mixing on droplet microphysics is further complicated by indications that turbulence can also act to cluster cloud droplets, enhancing collisional-coalescence and broadening the droplet size distributions [*Shaw*, 2003].

The exceptions to adiabatic cloud vertical profile discussed here will be further explored in chapter 3 as we examine how cloud vertical profile assumptions impact passive LWP retrievals.

2.2.1.1 Cloud Vertical Weighting

As mentioned in the previous section, it is difficult for passive satellite remote sensing to identify cloud properties in very specific layers or volumes of a cloud. As a consequence, absorbing spectral bands have limited penetration depth into the cloud and as a result retrievals like the bispectral r_e can be weighted toward the microphysics prevalent in the upper part of the cloud [*Platnick*, 2000]. Therefore, an important step toward understanding the retrieval results is to understand the vertical weighting involved in the r_e retrieval. If the spectral band is very strongly absorbing then it possible to approximate the cloud reflectance in this wavelength as being dominated by single scattering (because multiple scattering is inhibited by absorption). As such, an analytical vertical weighting function ($W(\tau)$) can be approximated by a two-way transmittance (2WT) function as follows [*Platnick*,

2000; *Alexandrov et al.*, 2012a]:

$$u(\tau) = e^{-\tau\left(\frac{1}{\mu_0}+\frac{1}{\mu}\right)}, \tag{2.43}$$

$$W(\tau) \equiv \frac{1}{C}\frac{\mathrm{d}u}{\mathrm{d}\tau}, \tag{2.44}$$

$$\int_{Z_{\mathrm{base}}}^{Z_{\mathrm{top}}} W(\tau)\ \mathrm{d}\tau = 1\,. \tag{2.45}$$

where μ_0 and μ are the cosines of the solar and viewing zenith angles, respectively. The form of $u(\tau)$ corresponds to the attenuation of two-way transmittance and leads to the definition of the vertical weighting function $W(\tau)$. This vertical weighting function provides a useful tool for interpreting r_e retrievals and comparing them to the microphysical properties of the scene. In *Platnick* [2000], $W(\tau)$ is used to estimate r_e retrieval, $r_e(\mathrm{2WT})$, from the vertical profile of $r_e(\tau)$,

$$r_{e,\mathrm{W}} = \int_0^{\tau_{\mathrm{tot}}} r_e(\tau)W(\tau)\mathrm{d}\tau\,. \tag{2.46}$$

However, a different approach to vertical weighting is adopted in this study. As described by *Alexandrov et al.* [2012a], the vertical weighting function $W(\tau)$ is first used to derive an effective size distribution, $N_{\mathrm{2WT}}(r)$, which is an optically weighted superposition of the droplet size distributions throughout the cloud column,

$$N_{\mathrm{2WT}}(r) = \int_0^{\tau_{\mathrm{tot}}} N(r,\tau)W(\tau)\mathrm{d}\tau\,. \tag{2.47}$$

The effective size distribution $N_{2\mathrm{WT}}(r)$ is then used to produce a vertically weighted r_e,

$$r_e(2\mathrm{WT}) = \frac{\int_0^\infty r^3 N_{2\mathrm{WT}}(r)\mathrm{d}r}{\int_0^\infty r^3 N_{2\mathrm{WT}}(r)\mathrm{d}r}. \tag{2.48}$$

The advantage of first defining a vertically weighted droplet size distribution is that it makes no assumptions about the shape of the droplet size distribution. In contrast, the other vertical weighted droplet size, $r_{e,2\mathrm{WT}}$) implicitly assumes that all of the variability in the vertical profile of droplet size distribution properties is attributable to r_e.

2.2.2 Inhomogeneity of Cloud Horizontal Properties

One of the most striking features of MBL clouds is that they have highly variable, and yet often self-similar, horizontal structures ranging from the mesoscale ($\approx 100\,\mathrm{km}$) down well below the sub-pixel scale of most satellite imaging sensors ($< 100\,\mathrm{m}$) [*Davis and Marshak*, 2010]. This large-scale self-similarity is characteristic of fractal cloud structure and poses many challenges for satellite cloud remote sensing. In addition to the physical aspects of horizontal structure there are also practical aspects, like satellite resolution, which become convoluted and produce complicated cloud retrieval biases.

Most cloud retrieval algorithms are forced to assume that clouds are horizontally homogeneous and infinitely plane-parallel below pixel resolution. In reality

however, pixel level reflectances are the result of scattering from the unresolved sub-pixel cloud properties. Broken cloud cover or clouds with inhomogeneous properties at the sub-pixel level can lead to the so-called plane-parallel homogeneous (PPH) bias. This effect is discussed at length in chapter 4 because it has strong effects on bispectral retrievals.

Light scattered from horizontally inhomogeneous clouds is susceptible to 3-D radiative effects, which can strongly impact cloud retrievals [*Várnai and Marshak*, 2001; *Zhang et al.*, 2012]. One method for quantifying the horizontal inhomogeneity of clouds is the sub-pixel inhomogeneity index, H_σ. To quantify the sub-pixel variability, remote sensing instruments sometimes produce measurements both at their principal retrieval resolution (ΔX) but also at a sub-pixel scale ($\Delta X/N$). For example, an instrument with a 1 km principle resolution (such as MODIS) and 250 km sub-pixel resolution this degree of sub-pixel inhomogeneity can be defined as in Equation 2.49 [*Liang et al.*, 2009]. It is evident from this definition that the interpretation of horizontal cloud inhomogeneity is directly tied to the principle footprint resolution of an instrument,

$$H_\sigma = \frac{\text{std}\left[R_i(0.865\,\text{m})\right]}{\text{mean}\left[R_i(0.865\,\text{m})\right]}\,, \tag{2.49}$$

where std [...] and mean [...] indicate the standard deviation and mean of the measured reflectances for the sub-pixels within the larger pixel footprint. When $H_\sigma > 0.4$ the underlying cloud can be considered inhomogeneous and $H_\sigma < 0.4$ is said to be more homogeneous.

Cloud horizontal structure is richly varied, in fact it is not uncommon for MBL clouds to self-organize into large scale cellular patterns as seen in Figure 2.3(top right) [*Agee et al.*, 1973; *Wood and Hartmann*, 2006]. This mesoscale cellular convection (MCC) is observed in both open and closed cellular forms. Open cells are characterized by dry subsiding air at the center of the cell creating cloud free regions with updrafts at the boundaries producing narrow clouds surrounding the cell. In contrast, the closed cellular form is characterized by updrafts at the center of the cell forming broad regions of thick stratiform cloud and the surrounding subsiding air thins the cloud near the cell edge. Transitions from closed to open cellular cloud fields are known to be triggered by precipitation which rapidly forms large pockets of open cells (POCs)[*Wang and Feingold*, 2009; *Feingold et al.*, 2010; *Koren and Feingold*, 2013]. Whether the cloud field has open or closed cellular structure plays an important role in determining both the radiative impact and the retrieval sensitivity to horizontal structure effects. It has been posited that the microphysics in open and closed cells could be different due to their relationship with the precipitation processes [*Wang and Feingold*, 2009]. This poses an interesting and difficult remote sensing problem, as cloud retrievals in the open cellular regions will suffer from sub-pixel inhomogeneity and 3-D effect biases.

2.3 Passive Cloud Remote Sensing Techniques

All of the cloud remote sensing techniques used throughout this study rely on libraries of cloud microphysical, optical, and radiative properties to one degree

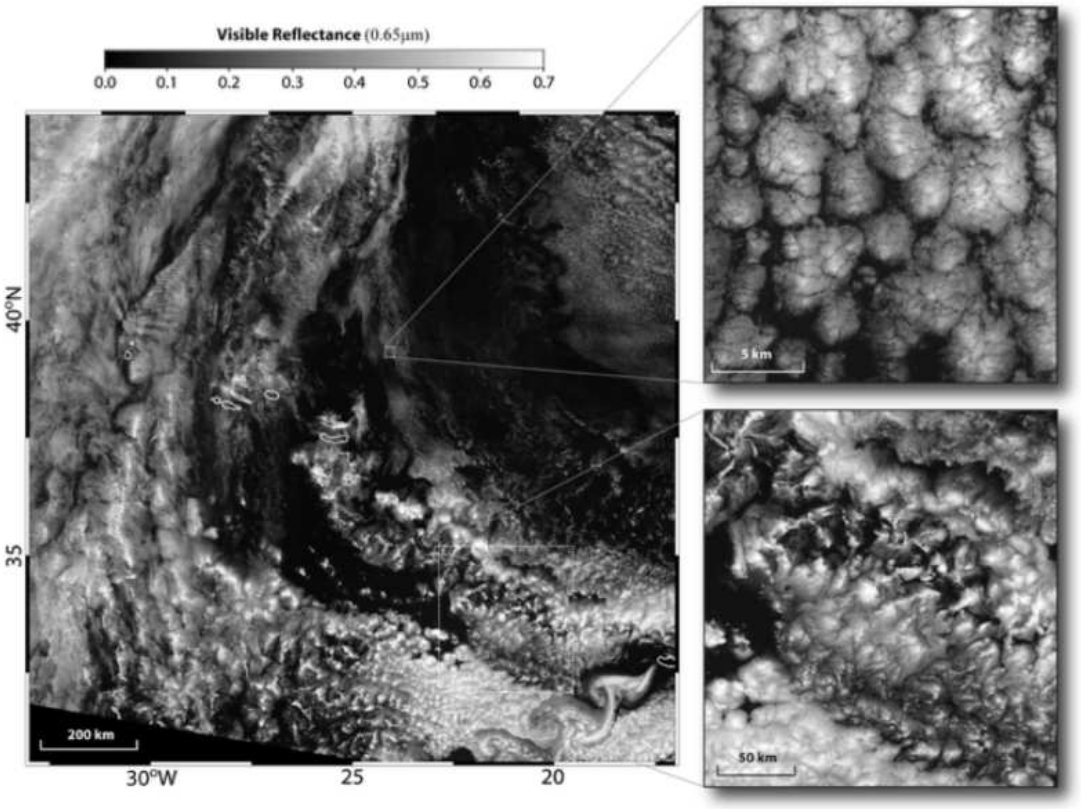

Figure 2.3: Satellite imagery demonstrating the tremendous wealth of spatial scales of MBL clouds on the mesoscale. The main panel is a 250 m resolution visible reflectance image ($\lambda = 0.65\,\mu$m) taken on April 7th 2001 at 12:35 UTC using the Moderate Resolution Imaging Spectroradiometer (MODIS) over the northeast Atlantic Ocean. The inset to the upper right shows a higher resolution (15 m) visible image ($\lambda = 0.8m$) taken at approximately the same time using the Advanced Spaceborne Thermal Emission and Reflection Radiometer (ASTER). The inset to the lower right shows detail from the main image. (Figure and caption adapted from *Wood* [2012].)

or another. The cloud optical property libraries used throughout these studies are based on single scattering Mie calculations of monodisperse droplet optical properties that are averaged with respect to size according to the gamma DSD. In addition, these single scattering optical properties are averaged with respect to wavelength over an instrument spectral response function (based on MODIS bands) and solar source functions (blackbody). The single scattering bulk cloud optical properties are subsequently used to run radiative transfer calculations for the so-called bispectral reflectance look-up-table (LUT). This LUT is made up of pre-calculated reflectances of plane-parallel and homogeneous (PPH) clouds over a high-resolution grid of combinations of τ_{tot}, r_e, and v_e. Here, τ_{tot} is defined in terms of the DSD.

2.3.1 The Bispectral Method

Many satellite-based techniques have been developed to retrieve cloud DSD properties from regional to global scales. These techniques typically infer DSD properties based on an assumed size distribution shape, characterized by an effective radius (r_e), and an effective variance (v_e). One such retrieval method is called the bispectral total reflectance technique, hereafter referred to as the bispectral technique, simultaneously retrieves cloud optical thickness (τ_{tot}) and r_e from a pair of cloud reflectances, one in the visible to near infrared (VNIR) and the other in the shortwave infrared (SWIR) spectral range [*Nakajima and King*, 1990]. This retrieval technique has been implemented for numerous satellite and airborne instruments, such as the Moderate Resolution Imaging Spectro-radiometer (MODIS, [King et al.,

2003; Platnick et al., 2003; 2016]), the Spinning Enhanced Visible and Infrared Imager (SEVIRI, [Roebeling et al., 2006]), and the National Polar-orbiting Partnership Visible Infrared Imaging Radiometer Suite (NPP VIIRS, [Rosenfeld et al., 2014]).

The bi-spectral method retrieves τ_{tot} and r_e simultaneously from a pair of cloud reflectances observed in VNIR and SWIR bands, respectively. The VNIR band, dominated by multiple scattering, provides sensitivity to τ_{tot}; the selected SWIR band, where liquid water droplets are moderately absorptive, provides sensitivity to r_e. This method is usually implemented using a LUT like the one shown in Figure 2.4(a), which has a fixed v_e. Cloud reflectance in the VNIR band (centered around 0.865 μm) increases with τ_{tot} (gray) for a fixed r_e, while the reflectance in the SWIR band (centered around 3.75 μm) decreases with r_e (colored) when τ_{tot} is fixed. The retrieved properties are obtained by performing a two-dimensional inverse interpolation between observed reflectance and the τ_{tot} and r_e grid. A notable characteristic of the bispectral LUT is that when the optical thickness is low ($\tau_{\text{tot}} < 3$), the isolines of the LUT are more densely packed and less orthogonal, which results in reduced sensitivity and increased retrieval uncertainty [*Werner et al.*, 2013]. The bispectral technique, while sensitive to r_e, is not particularly sensitive to v_e, so typically an a priori guess is required (e.g., $v_e = 0.1$ in the operational MODIS retrieval). While different combinations of VNIR and SWIR bands are used to perform the bispectral retrieval, in this study we focus on VNIR reflectances centered on 0.865 μm and SWIR reflectances centered on both 2.13 and 3.75 μm. There are consequences for the r_e retrieval depending on the particular SWIR band selected. For example, a strongly absorbing band limits penetration into the cloud and as a

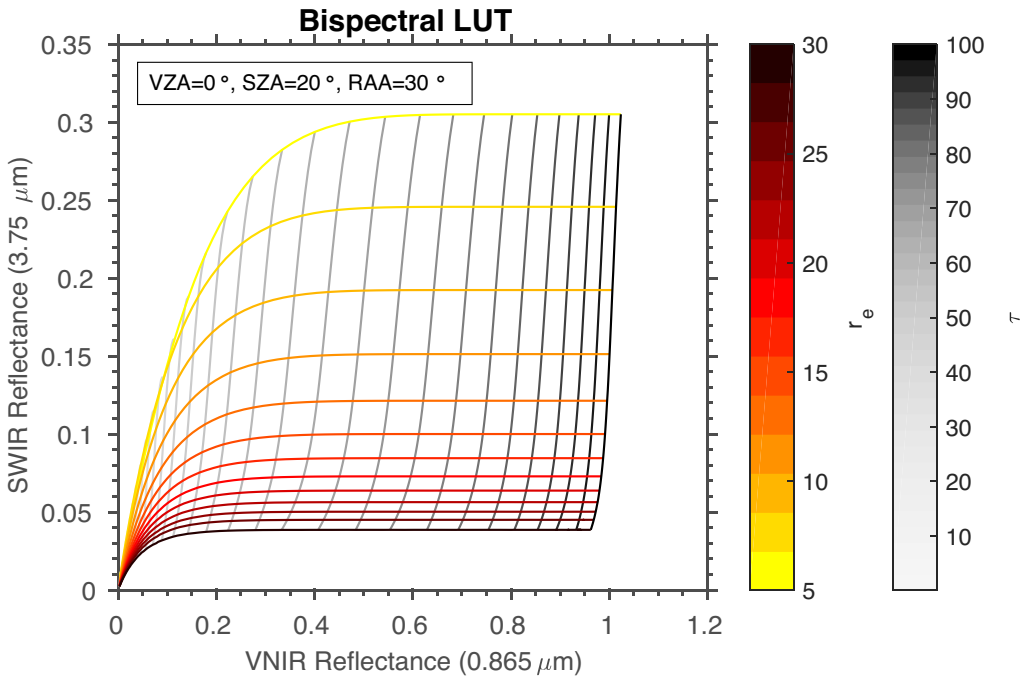

Figure 2.4: Demonstrations of the microphysical sensitivity of the bispectral and the polarimetric techniques. Panel (a) features the bispectral LUT exhibiting sensitivity to r_e (colored iso-lines), due to absorption in the SWIR reflectance. The VNIR reflectances provide sensitivity to τ_{tot} (gray iso-lines).

result the retrieved r_e is vertically weighted toward the microphysics prevalent in the uppermost part of the cloud [*Platnick*, 2000].

2.3.2 The Polarimetric Technique

A second, vastly different, retrieval technique is the multi-angular polarimetric reflectance technique, hereafter referred to as the polarimetric technique. This retrieval requires multi-angular observations of the polarized reflectance in the cloud-bow scattering region. In addition to r_e, the polarimetric technique can also retrieve v_e [*Bréon and Goloub*, 1998]. Global retrievals using the polarimetric technique were first demonstrated by the Polarization and Directionality of Earth Reflectance (POLDER, [*Deschamps et al.*, 1994]) instruments operating from 1996 to 2013 on three different satellite platforms. The Aerosol Polarimetry Sensor (APS, [*Mishchenko et al.*, 2007]) would have been the first space-borne multi-angular polarimeter from U.S. to provide global aerosol and cloud property retrievals. Unfortunately, it was lost as a result of the satellite launch failure in 2011, which suddenly interrupted development of polarimetric-based remote sensing in the U.S. Recognizing the great potential of polarimetric techniques for aerosol and cloud remote sensing, NASA has invested heavily in recent years on the development of airborne polarimeters, such as the Research Scanning Polarimeter (RSP, [*Cairns et al.*, 2003]), the Airborne Multi-angle Spectro-Polarimetric Imager (AirMSPI, [*Diner et al.*, 2013]) and the Airborne Hyper-Angular Rainbow Polarimeter (Air-HARP, [*Martins et al.*, 2017]). Moreover, several space-borne missions are in development, such as the

Multi-Angle Imager for Aerosols (MAIA, [*Liu and Diner*, 2017]), HARP, the Plankton, Aerosols, Cloud, ocean Ecosystem mission (PACE) and the Multi-viewing, Multi-channel, Multi-polarization imaging mission (3MI, [*Marbach et al.*, 2013]). Each of these missions will have a multi-angular polarimeter on-board. In the foreseeable future, we may expect to have operational global retrievals of cloud droplet size distributions from both bispectral and polarimetric methods.

For the polarimetric technique, the source of sensitivity to cloud microphysical properties stems from the angular pattern of the linearly polarized reflectance. Polarized reflectances are dominated by single scattering because multiple scattering induces depolarization. As a result, the single scattering polarized phase functions ($-P_{12}$) shown in Figure 2.5 are good approximations to the observed angular pattern of polarized cloud reflectances [*Bréon and Goloub*, 1998]. These phase functions demonstrate the sensitivity of the polarimetric retrieval to both r_e and v_e. As r_e increases in Figure 2.5(b) the supernumerary bow peaks (around a scattering angle of 142°) become narrower and shift toward smaller scattering angles. In contrast, as v_e increases in Figure 2.5(c) the supernumerary bow peaks erode in magnitude, eventually smoothing out for broad DSDs ($v_e > 0.15$). A consequence of this erosion of the supernumerary peaks is that the polarimetric retrieval has less sensitivity to both r_e and v_e for very broad DSDs. The polarimetric retrieval does not significantly rely on multispectral information, although observations in several bands may help provide stronger observational constraints due to the shift in the supernumerary bows with changing wavelength, as shown in Figure 2.5(a). The dominance of the single scattering contributions to the polarized reflectance leads to cloud re-

trievals that represent microphysical properties within the top $\sim$ 3 optical depths in the cloud. The polarimetric retrieval is often based on a parametric curve fitting retrieval algorithm like the one presented in [*Alexandrov et al.*, 2012a]. However, there are also other retrieval approaches, including the Rainbow Fourier Transform technique of *Alexandrov et al.* [2012b], which can retrieve multi-modal DSDs.) The parametric technique relies on a library of $-P_{12}$ curves with varying r_e and v_e that are parametrically scaled and adjusted to fit the observed reflectance via a nonlinear least squares optimization procedure. This process yields the phase function that best matches the angular pattern of the observation, thus determining the r_e(pol) and v_e(pol) retrieval. The polarimetric method described above does not result in a retrieval of τ_{tot}, however, it can still be obtained by implementing a simplified variant of the bispectral τ_{tot} retrieval. With simultaneous measurements of the total reflectance in a VNIR band and the r_e(pol) retrieval, a VNIR-only LUT curve can be used to perform a 1-D interpolation of the corresponding bispectral LUT curve for $R_{VNIR}(r_e(\text{pol}), \tau_{\text{tot}})$.

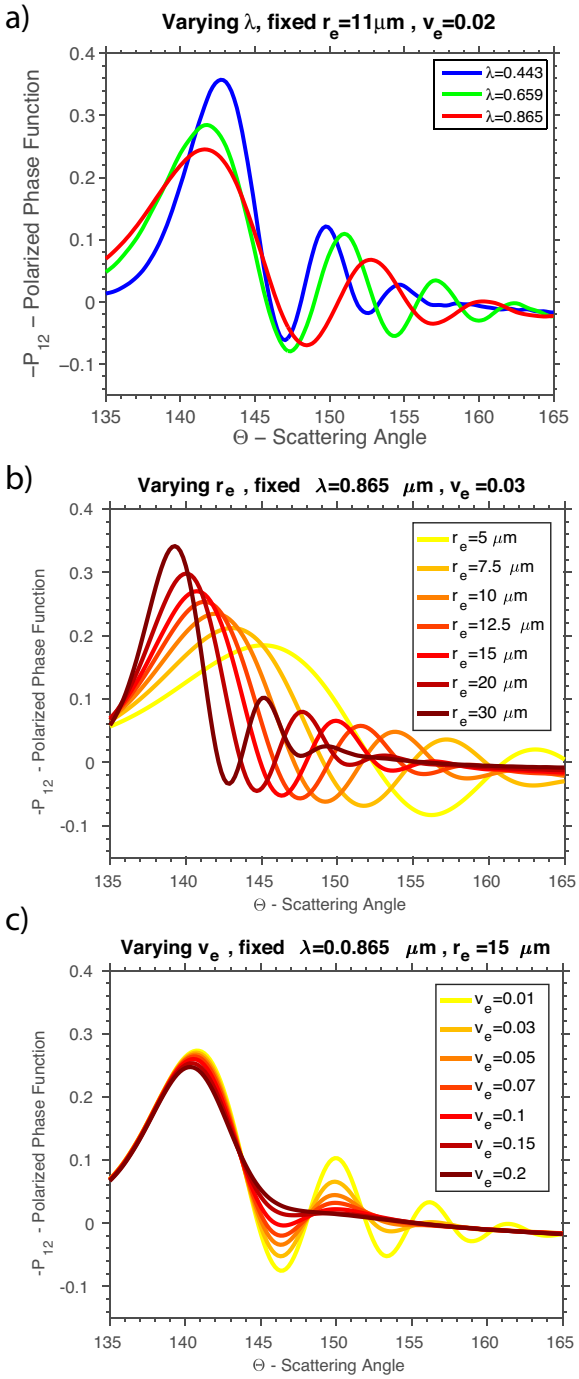

Figure 2.5: The spectral variability of the polarized reflectances is shown in panel (a). Demonstrations of the microphysical sensitivity of the polarimetric technique are shown in panels (b) and (c) demonstrate the sensitivity of polarimetric technique to r_e and v_e respectively. The supernumerary bow peaks of the polarized phase function ($-P_{12}$) shift and become narrower with increasing droplet size (r_e), whereas the peaks erode in magnitude for broadened droplet size distributions (v_e).

2.4 The Satellite Remote Sensing Simulator

2.4.1 The DHARMA LES Model

The remote sensing retrieval simulator implemented in this study is built around a cloud resolving LES model (DHARMA) with bin microphysics [*Ackerman et al.*, 2004; *Zhang et al.*, 2012; *Miller et al.*, 2016]. The LES provides freely evolving 3-D cloud microphysical properties, which are used as reference when comparing to numerically simulated retrievals. The DHARMA LES adopts 25 size bins to represent droplet size distributions [*Ackerman et al.*, 1995]. Unlike a parameterized cloud microphysics scheme, this method makes no assumptions about the shape or number of modes of the droplet size distribution. A bin scheme uses basic physical relationships to describe droplet activation, condensation, collision-coalescence, and sedimentation. Conveniently, the bin scheme also allows us to discriminate drizzle drops from cloud droplets by using a bin size cutoff of $\approx 30\,\mu m$. Distinguishing these two populations of droplets allows us to examine the impact of the larger drops on remote sensing retrievals. The optical properties of each size bin are computed by bulk averaging Mie scattering properties over a highly resolved constant sub-bin droplet size distribution, as described in section 2.1.2. It should be noted that the background aerosols that serve as cloud condensation nuclei in the model are not included in the radiative transfer scene.

2.4.2 LES Cloud Scenes

Three LES cases are the focus of these studies. The first (referred to as ATEX clean hereafter) and second (ATEX polluted) cases are based on an idealized case study from the Atlantic Trade Wind Experiment (ATEX), with different aerosol loadings [Stevens et al., 2001]. The ATEX cases are representative of a trade wind cumulus regime in which scattered cumuli rise into a thin, broken stratocumulus layer. The third case (referred to as DYCOMS-II hereafter), originally presented in Stevens et al. (2005), is an idealized setup based on clouds observed during the second research flight (RF02) of the Second Dynamics and Chemistry of Marine Stratocumulus project (DYCOMS-II) [Stevens et al., 2010]. This case is representative of nocturnal marine stratocumulus under a dry inversion. The specific details of the LES scene properties change from study to study, and these will be discussed in greater detail in chapter 3, chapter 4, and chapter 5.

2.4.3 Radiative Transfer Calculations

Radiative transfer calculations in the this remote sensing simulator are performed by a variety of radiative transer models, each selected to address the specific cloud remote sensing questions of each study. In the cloud LWP and vertical inhomogeneity studies in chapter 3, we make use of the discrete ordinates radiative transfer (DISORT) model [*Stamnes et al.*, 1988], producing 1-D total radiances at the horizontal resolution of the LES grid. The high-resolution 1-D retrievals allow for the isolation of the vertical profile effects from other known retrieval biases

that exist due to inhomogeneous horizontal structure, and 3-D radiative effects. In the study comparing bispectral and polarimetric cloud retrievals in chapter 4 we make use of vector radiative transfer models that result in both the total and polarized reflectances. The vector radiative transfer calculations are performed using a polarized doubling-adding technique (PDA) to produce 1-D total and polarized reflectances at the horizontal resolution of the LES grid [*De Haan et al.*, 1987]. A demonstration of an "imager-mode" of the satellite simulator reflectances is shown in Figure 2.6. Total and polarized reflectances (panel a and b respectively) for a cloudy DYCOMS-II LES scene, where the viewing angle changes horizontally across the scene (as shown in panel c). The viewing angle range is chosen such that the primary and supernumerary cloudbows are visible in the polarized reflectances, while the primary bow is slightly visible in the total reflectance but it doesn't have significant spectral variability. Panel (d) displays the column mean of the LES polarized reflectances, and shows clear signals in the primary and supernumerary bow features for different wavelengths.

The sole consideration of 1-D retrievals avoids 3-D radiative effects and focuses this study on retrieval technique differences rather than on radiative processes. In contrast, the study in chapter 5 focuses on differences between 3-D radiative effects in total and polarized reflectances and their consequences for cloud remote sensing. To that end, the simulation of cloud reflectances in both 1-D (independent pixel) and 3-D scenes will be obtained using the recently developed polarized Monte Carlo radiative transfer algorithm MSCART (Multiple-Scaling-based Cloudy Atmospheric Radiative Transfer)[*Wang et al.*, 2017].

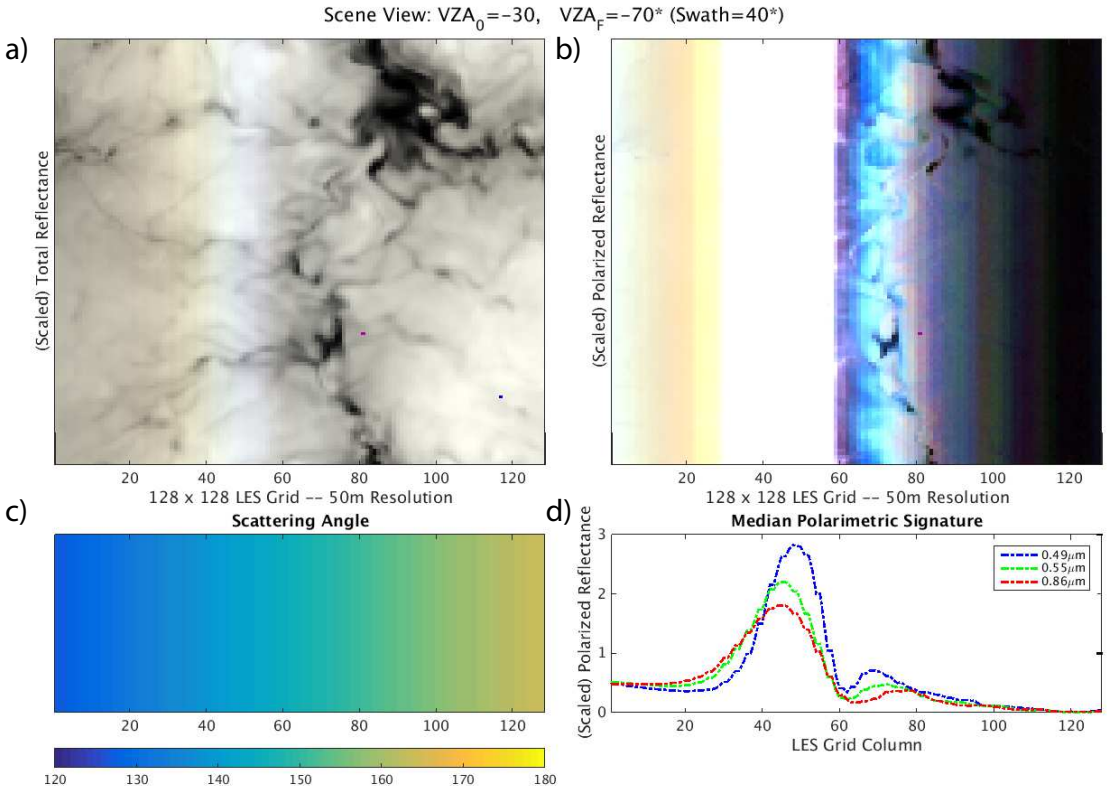

Figure 2.6: Demonstration of the "imager-mode" cloud reflectances from the LES-satellite simulator used in this study. Total and polarized reflectances are shown in panel (a) and (b) respectively. The viewing angle varies horizontally through the simulated scene as shown in panel (c). Median vertical slices demonstrate the angular variability and spectral variability of the polarized cloud reflectances panel (d).

Chapter 3: The impact of cloud vertical profile on passive cloud retrievals of LWP

Passive optical retrievals of cloud liquid water path (LWP), like those implemented for Moderate Resolution Imaging Spectroradiometer (MODIS), rely on cloud vertical profile assumptions to relate τ_{tot} and r_e retrievals to LWP. These techniques typically assume that shallow clouds are vertically homogeneous; however, an adiabatic cloud model is plausibly more realistic for shallow marine boundary layer cloud regimes. In this study a satellite retrieval simulator is used to perform MODIS-like satellite retrievals, which in turn are compared directly to the large-eddy simulation (LES) output. This satellite simulator creates a framework for rigorous quantification of the impact that vertical profile features have on LWP retrievals, and it accomplishes this while also avoiding sources of bias present in previous observational studies. The cloud vertical profiles from the LES are often more complex than either of the two standard assumptions, and the favored assumption was found to be sensitive to cloud regime (cumuliform/stratiform). Confirming previous studies, drizzle and cloud top entrainment of dry air are identified as physical features that bias LWP retrievals away from adiabatic and toward homogeneous assumptions. The mean bias induced by drizzle-influenced profiles was shown to be

on the order of 5–10 $\mathrm{g/m^2}$. In contrast, the influence of cloud top entrainment was found to be smaller by about a factor of 2. A theoretical framework is developed to explain variability in LWP retrievals by introducing modifications to the adiabatic r_e profile. In addition to analyzing bispectral retrievals, we also compare results with the vertical profile sensitivity of passive polarimetric retrieval techniques.

3.1 Overview

Cloud liquid water path (LWP) is a key parameter in many cloud physical processes (e.g., condensation, evaporation, and precipitation) and largely determines cloud shortwave radiative forcing. Many techniques have been developed to retrieve cloud LWP from satellite observations. In this study, we focus on the so-called bispectral solar reflectance method (hereafter bispectral method) of *Nakajima and King* [1990]. This method employs a pair of cloud reflection observations, one in the visible and near-infrared (VNIR), and the other in the shortwave-infrared (SWIR) spectral region. These two bands are used to simultaneously retrieve cloud optical thickness (τ_{tot}) and cloud droplet effective radius (r_e). Cloud LWP can be computed from the retrieved τ_{tot} and r_e by using the relationship,

$$\mathrm{LWP} = C\rho_l r_e \tau_{\mathrm{tot}} \,, \tag{3.1}$$

where ρ_l is the bulk density of liquid water and C is a coefficient that can be derived from the assumed vertical cloud profile (see subsection 2.2.1 for more discussion). Several widely used satellite cloud property products are based on the bispectral

method. Most notably, this includes the operational cloud products from the Moderate Resolution Imaging Spectroradiometer (MODIS) [*King et al.*, 2003; *Platnick et al.*, 2003], the Spinning Enhanced Visible and Infrared Imager (SEVIRI) [*Roebeling et al.*, 2006], and National Polar-orbiting Partnership Visible Infrared Imaging Radiometer Suite (NPP VIIRS) [*Rosenfeld et al.*, 2014]. The cloud products derived from these instruments include LWP retrievals used in numerous studies, for example, to evaluate spatial variability of MBL cloud LWP [*Wood and Hartmann*, 2006], to study the warm rain process in MBL clouds [*Kubar and Hartmann*, 2009; *Suzuki et al.*, 2011], to evaluate cloud LWP simulation in climate models [*Jiang et al.*, 2012], and to assess the impact of aerosols on MBL clouds [*Costantino and Breon*, 2013b].

The wide use of the bispectral method makes it important to understand its inherent limitations and potential sources of retrieval uncertainty. Among others, the influence of cloud vertical profile on the bispectral retrieval of LWP has received significant and increasing attention in recent years [*Wood and Hartmann*, 2006; *Bennartz*, 2007; *Seethala and Horváth*, 2010; *Lebsock and Su*, 2014]. In operational bispectral retrieval algorithms, clouds are commonly assumed to be vertically homogeneous (i.e., $r_e(\tau)$ is constant) which implies that the constant $C = 2/3$ in Equation 3.1, and thus,

$$\mathrm{LWP_h} = \frac{2}{3}\rho_l r_e \tau_{\mathrm{tot}} \,. \tag{3.2}$$

Here the subscript h denotes LWP retrievals based on the homogeneous vertical profile assumption. It is well established, however, that MBL clouds may develop

inhomogeneous vertical profiles as a result of a variety of physical processes. For example, in situ measurements commonly resemble an adiabatic profile associated with droplet condensational growth in nonprecipitating MBL clouds. Adiabatic profiles exhibit cloud water content (LWC) that increases linearly with height from cloud base, because cloud droplet number concentration (CDNC) is constant and all droplet activation occurs at the cloud base [*Nicholls and Leighton*, 1986; *Miles et al.*, 2000; *Brenguier et al.*, 2003]. observations of MBL clouds typically differ slightly from the theoretical adiabatic profile, with a reduced vertical gradient of LWC compared to theory. Profiles exhibiting this reduced gradient are referred to as sub-adiabatic. On the basis of these observations, a number of recent studies have argued that an adiabatic or sub-adiabatic profile is a better assumption for LWP retrievals. These studies have also suggested that assuming clouds to be vertically homogeneous could lead to an overestimation of the LWP of MBL clouds [*Wood and Hartmann*, 2006; *Seethala and Horváth*, 2010]. For both adiabatic and sub-adiabatic vertical profiles $C = 5/9$ in Equation 3.1 leading to the expression:

$$\mathrm{LWP}_{\mathrm{ad}} = \frac{5}{9}\rho_l r_e^{\mathrm{top}} \tau_{\mathrm{tot}} \,, \tag{3.3}$$

where r_e^{top} specifically denotes the droplet size at cloud top and the subscript ad denotes the assumption of adiabatic or subadiabatic vertical profile. In an operational retrieval sense, where the same droplet size retrieval may be used for both $\mathrm{LWP}_{\mathrm{h}}$ and $\mathrm{LWP}_{\mathrm{ad}}$ assumptions, the difference between equations Equation 3.2 and Equation 3.3 is purely in terms of the value of the constant C. Given that both

adiabatic and subadiabatic behavior result in the same LWP relationship, we will simply refer to this as the adiabatic LWP relationship.

Although the adiabatic profile is more appealing and has been increasingly favored over the homogeneous profile in recent studies, only a few have systematically compared and evaluated LWP retrievals based on the two assumptions. For example, *Seethala and Horváth* [2010] compared the two sets of MODIS LWP retrievals (LWP_h and LWP_{ad}) with collocated LWP retrievals from the Advanced Microwave Scanning Radiometer for EOS (AMSR-E). One advantage of the AMSR-E retrieval is that it is less sensitive to cloud vertical profile because the information content for the retrieval comes from transmitted surface microwave emission. Interestingly, they found that assuming adiabatic vertical profile in MODIS LWP retrievals does not always lead to a better agreement with AMSR-E results (see their Figure 6). Over the subtropical coastal stratocumulus regions (e.g., SE Atlantic and Pacific), the results are as expected: the LWP_h overestimates AMSR-E retrievals and the retrieval assuming adiabatic profile, LWP_{ad}, leads to better agreement between the two instruments. However, over tropical and subtropical shallow cumulus regions, the adiabatic assumption increases the difference between the two methods. The LWP_h retrievals from MODIS over these regions are already smaller than AMSR-E results, and assuming an adiabatic profile, LWP_{ad}, makes the underestimation bias even worse. The authors listed a number of potential issues in both MODIS and AMSR-E retrieval techniques that may cause such a bias. However, one possible physical explanation they noted was that entrainment of dry air at cloud top can reduce r_e and thereby induce an underestimated LWP. This occurs because MODIS r_e

retrievals are particularly sensitive to cloud top properties. In a more recent study, *Lebsock and Su* [2014] carried out a comprehensive intercomparison between MODIS (based on adiabatic $\mathrm{LWP_{ad}}$), AMSR-E, and CloudSat LWP retrievals over global oceans. Similar to *Seethala and Horváth* [2010], they also found that MODIS $\mathrm{LWP_{ad}}$ retrievals are in better agreement with the other two data sets over subtropical stratocumulus regions than over tropical and subtropical cumulus cloud regions. Taking advantage of the sensitivity of the CloudSat radar to precipitation in MBL clouds, they found that over the subtropical cumulus cloud regions rainwater accounts for a substantial portion of LWP (see their Figure 14). They hypothesized that the LWP retrieval differences between MODIS and AMSR-E over these regions may be partly caused by differences in the sensitivity of MODIS and AMSR-E algorithms to precipitation. In addition to remote sensing studies, MODIS LWP retrievals have also been rigorously compared to *in situ* observations in field campaigns specifically examining MBL clouds (stratocumulus) [*Noble and Hudson*, 2015]. This study indicated several potential sources of bias for r_e and τ_{tot} that propagate into LWP retrievals. Comparing the homogeneous and adiabatic retrieval assumptions to the *in situ* observations led to mean LWP retrieval biases of 37% and 14%, respectively. For one of the *in situ* data sets studied the MODIS retrieval of τ_{tot} did not appear to be the source of LWP bias, while r_e retrievals were found to be high biased despite being well correlated with *in situ* measurements. One of the conclusions of *Noble and Hudson* [2015] was that MODIS captured the variability of r_e while still being systematically biased due to cloud inhomogeneity, cloud top retrieval sensitivity, or temporal discrepancies between in situ cloud penetration and satellite overpass.

These recent studies have shed light on important limitations and uncertainties associated with bispectral LWP retrievals in comparison with other remote sensing techniques. Beyond cloud vertical profile, however, the bispectral method is sensitive to other sources of retrieval bias. Notable examples include inhomogeneous cloud horizontal structure and retrieval resolution [*Oreopoulos and Davies*, 1998; *Zhang et al.*, 2012], as well as 3-D radiative transfer effects [*Várnai and Davies*, 1999; *Várnai and Marshak*, 2001; *Marshak et al.*, 2006]. These sensitivities are often entangled such that it is problematic to completely separate them in observational studies like those previously mentioned. Moreover, the physical mechanisms underlying the influence of cloud vertical profile on the bispectral LWP retrieval remain largely unexplored in the observational studies.

This study approaches the problem from a different perspective; rather than use remote sensing data, synthetic retrievals are generated from large-eddy simulations (LESs) of cloud scenes. Synthetic retrievals are obtained by modeling the radiative transfer of a scene and performing bispectral retrievals using the resulting reflectances. As discussed in detail in subsection 2.4.1, an advantage of using synthetic retrievals is that uncertainty sources in the retrieval are known and can be controlled, permitting a more focused and in-depth study. The overall objective is to improve understanding of how cloud vertical profile affects bispectral LWP retrievals. More specifically, we hope to shed light on three questions. First, which cloud vertical profile assumption, homogeneous ($\mathrm{LWP_h}$), or adiabatic ($\mathrm{LWP_{ad}}$), leads to bispectral LWP retrievals that agree better with the ground truth from our LES cases? Second, how does cloud vertical profile vary with MBL cloud types (e.g.,

stratocumulus versus cumulus) and what are the consequences of selecting a particular cloud vertical profile assumption for bispectral retrievals? Third, how do cloud top entrainment and the presence of drizzle in MBL clouds influence bispectral retrievals? We address these questions not only using numerical simulations but also by developing a theoretical and analytical framework that can explain the bispectral LWP retrievals for a given true cloud vertical profile from the LES cloud model.

3.2 Results and Analysis

3.2.1 LWP Retrievals

With two vertical profile assumptions for LWP retrieval it is natural to ask the question: does the homogeneous $\mathrm{LWP_h} = 2/3\rho_l r_e \tau_{\mathrm{tot}}$ or adiabatic $\mathrm{LWP_{ad}} = 5/9\rho_l r_e^{\mathrm{top}} \tau_{\mathrm{tot}}$ relationship compare more closely with the LES ground truth? In an attempt to address this question, Figure 3.1 provides gray scale images showing $\mathrm{LWP_{LES}}$ for the three LES cases. The biases of $\mathrm{LWP_h}$ and $\mathrm{LWP_{ad}}$ relative to $\mathrm{LWP_{LES}}$ are then used to identify which retrieval is favored. The favored retrieval assumption is simply the one with a smaller absolute bias. The red contour lines in Figure 3.1 surround retrieval pixels that favor adiabatic vertical profile assumptions, while the blue contour lines surround retrieval pixels that favor homogeneous profile assumptions. For this comparison, both of the retrievals make use of the MODIS-like bispectral $r_e(3.7\,\mu\mathrm{m})$ and τ_{tot} retrievals. To address LES columns that do not overwhelmingly favor either retrieval, a third population is defined, and these columns lie in the space between the red and blue contour lines. This population is

defined by the following tolerance condition on the ratio of the two biases,

$$0.75 \leq \frac{|LWP_{\mathrm{h}} - LWP_{\mathrm{LES}}|}{|LWP_{\mathrm{ad}} - LWP_{\mathrm{LES}}|} \leq 1.25\,. \tag{3.4}$$

The lower and upper ends of the inequality correspond to cases that favor homogeneous and adiabatic assumptions, respectively. It is intriguing to observe that none of the three cases support a single retrieval assumption but rather indicate that $\mathrm{LWP_{ad}}$ works better for some columns, while $\mathrm{LWP_h}$ works better for others. As summarized in the first column of Table 3.1, the $\mathrm{LWP_{ad}}$ retrieval works better for about 70% of the cloudy LES columns in the DYCOMS-II case, 22% in the ATEX clean case, and 70% in the ATEX polluted case. The most appropriate retrieval assumption appears to depend on cloud regime.

It is important to note that in this study, we focus on the r_e retrieval based on the 3.75 μm SWIR band for a few reasons. First, it is a common SWIR band found on board most passive polar-orbiting and geostationary instruments, such as advanced very high resolution radiometer, MODIS, VIIRS, and SEVIRI. Recent studies also indicate that the 3.75 μm band is less sensitive to 3-D radiative transfer effects than other SWIR bands, such as 2.13 and 1.65 μm [*Zhang and Platnick*, 2011; *Zhang et al.*, 2012; *Cho et al.*, 2015].

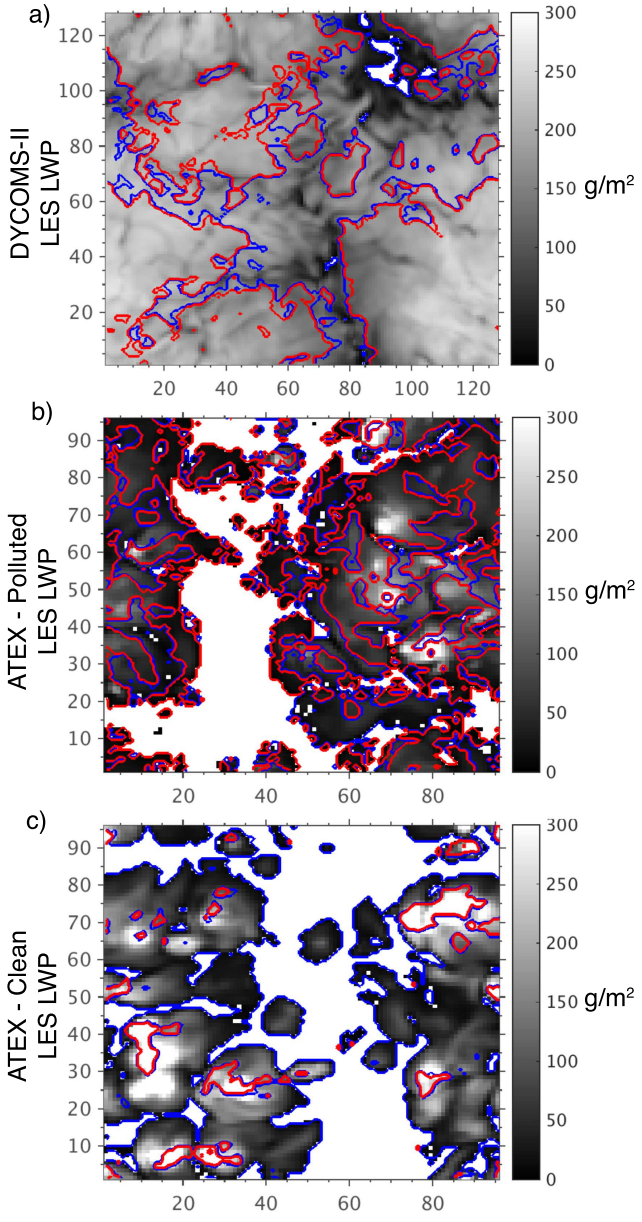

Figure 3.1: These figures depict the VNIR-SWIR retrieval of cloud LWP with adiabatic assumptions as in Equation 3.3 and using the $r_e(3.7\,\mu m)$ retrieval to represent the cloud top droplet size for several LES cases. The red and blue contours outline regions where the adiabatic (red) or constant (blue) vertical profile assumptions more accurately predicted the LES LWP.

	Steps of Procedure					
	1. Original Scene		2. Remove Drizzle		3. Remove Drizzle & Trans. Zone	
Profile Assumption	5/9	2/3	5/9	2/3	5/9	2/3
DYCOMS-II	70.7%	19.1%	91.5%	4.0%	96.3%	1.5%
ATEX Clean	21.7%	73.2%	41.5%	49.8%	54.2%	37.3%
ATEX Polluted	69.8%	19.3%	69.8%	19.63%	84.4%	3.6%

Table 3.1: Percentage of columns that favor adiabatic, homogeneous, or neither LWP retrieval assumption. The rows separate different LES cases and the columns distinguish removal of features. The statistics are aggregated over all scenes for each LES case.

3.2.2 LWP Retrieval Bias Budget

Biases in the bispectral LWP retrieval can result from a number of sources. The retrieval is sensitive to biases resulting from the a priori vertical profile assumption as well as the biases in the τ_{tot} and r_e retrievals that LWP is calculated from. To identify the importance of the bias resulting from cloud vertical profile assumptions, we consider the total bias budget of the LWP retrieval. Treating each of the biases as a deviation away from the actual LES properties leads to the following bias budget,

$$\begin{aligned} LWP_{\text{ret}} &= LWP_{LES} + \Delta LWP \\ &= (C_{\text{LES}} + \Delta C)\,\rho_l\,(r_{e,\text{LES}} + \Delta r_e+)\,(\tau_{\text{LES}} + \Delta\tau)\ , \end{aligned} \tag{3.5}$$

from which the first-order terms can be extracted:

$$\Delta LWP_C \approx (C_{\text{ret}} - C_{\text{LES}})\,\rho_l r_{e,\text{LES}} \tau_{\text{LES}}\,, \tag{3.6}$$

$$\Delta LWP_{r_e} \approx C_{\text{LES}}\rho_l\,(r_{e,\text{ret}} - r_{e,\text{LES}})\,\tau_{\text{LES}}\,, \tag{3.7}$$

$$\Delta LWP_{\tau} \approx C_{\text{LES}}\rho_l r_{e,\text{LES}}\,(\tau_{\text{ret}} - \tau_{\text{LES}})\,, \tag{3.8}$$

where the subscript "ret" denotes retrieved properties and the subscript LES denotes properties taken from the LES scene itself. These biases are reported in units of g/m^2 and are referred to here as the vertical profile assumption bias ΔLWP_C, the r_e retrieval bias ΔLWP_{r_e}, and the τ_{tot} retrieval bias (ΔLWP_{τ}). Although not shown here, higher-order cross terms obtained by fully factoring Equation 3.5 account for a very small portion of the overall LWP retrieval bias, so we neglect them throughout. The value of τ_{LES} can be obtained from LES microphysics in a straightforward manner, while the definition of $r_{e,\text{LES}}$ and C_{LES} require further introduction. The definition of $r_{e,\text{LES}}$ is tied to the definition of cloud top, which we define operationally for each LES column with respect to the cloud maximum LWC located near the optical cloud top (defined as the first cloudy layer with $\tau > 10^{-3}$):

$$r_{e,\text{LES}} \equiv r_e^* = r_e\,(z\,(\max\,[\text{LWC}]))\,. \tag{3.9}$$

Where $r_{e,\text{LES}}$ is recast as r_e^* to recognize that its value depends on the definition of cloud top. The definition of cloud top will be further discussed in the proceeding section. The definition of C_{LES} depends on the coupled relationship between other

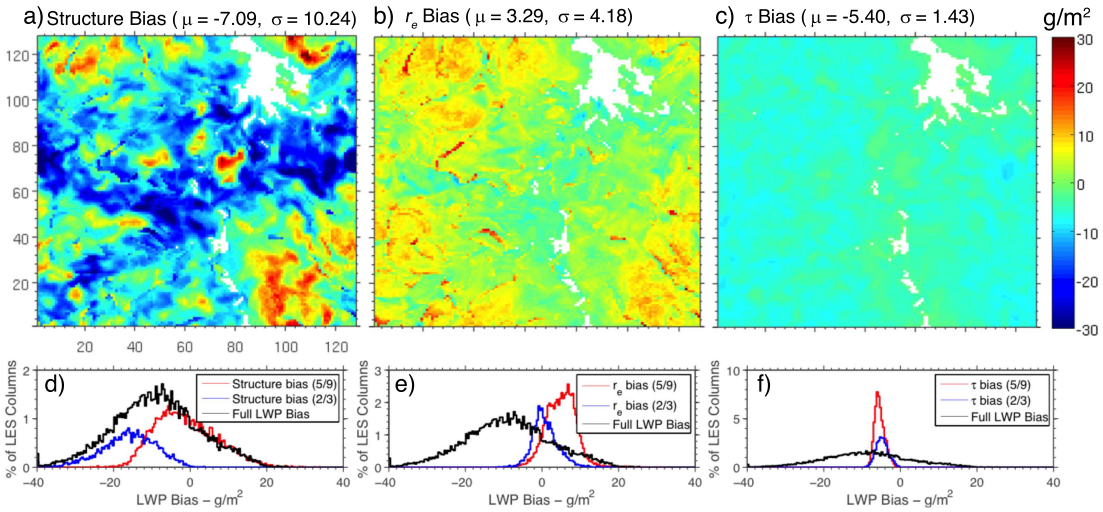

Figure 3.2: The LWP bias budget for a DYCOMS-II scene is broken into the profile bias (a, d), the r_e bias (b, e), and the τ_{tot} bias (c, f). Panels a-c depict the spatial distributions of these biases, while panels d-f depict their corresponding histograms. The mean and standard deviation (μ and σ) of each of the biases in this scene are stated in units of g/m^2. Together these results demonstrate that the profile assumption bias dominates the LWP bias budget (see text).

LES properties outlined in Equation 3.1,

$$C_{\text{LES}} = \frac{\text{LWP}_{\text{LES}}}{r_{e,\text{LES}}\tau_{\text{LES}}}. \tag{3.10}$$

The bias budget presented here allows for the evaluation of the relative importance of each of the primary biases. Analysis of both the spatial distribution and histograms of these primary bias terms yields interesting insight. The spatial distributions of each of the terms in the bias budget for the DYCOMS-II LWP_{ad} retrieval ($C_{\text{ret}} \equiv 5/9$) are shown in Figure 3.2(a-c). These results reveal that the profile assumption bias and the r_e retrieval bias are non-uniformly distributed, in contrast with the more uniformly distributed τ_{tot} retrieval bias. Moreover, the profile assumption bias and the r_e retrieval bias appear to be spatially correlated with the

contours defining the retrieval-favoring populations in Figure 3.1(a). Histograms of these biases, seen in Figure 3.2(d-f), reveal that the magnitude of the vertical profile assumption bias is also highly varied, with some of the population biased high and some low. In contrast, the distributions of the r_e and τ_{tot} retrieval biases are substantially narrower and on average smaller than the vertical profile bias. Motivated by this case, the focus of the remainder of this study will be on the impact of cloud vertical profile assumptions and the physical causes of r_e retrieval bias. While only shown for one scene from one LES case, the vertical profile and r_e retrieval biases were each consistently the greatest contributors to the bias budget across all scenes and cases. The τ_{tot} bias is less deserving of further scrutiny because it cannot account for either the spatial variability or much of the magnitude of the full LWP bias.

3.2.3 Vertical Profiles of LES properties

To further understand the impact of cloud vertical profiles on LWP retrievals, the profiles of several cloud properties were discriminated into two retrieval populations (i.e., LWP_{h} favored versus LWP_{ad} favored). The median vertical profiles for the DYCOMS-II case in Figure 3.3(a,b) demonstrate that both LWP_{h}-favored (blue) and LWP_{ad}-favored (red) columns have similar vertical profiles in terms of CDNC and LWC. The profile of CDNC remains relatively constant within the cloud, with the LWP_{h}-favored columns having on average a smaller CDNC than those LWP_{ad}-favored columns. The LWC profiles for both populations show a characteristic linear

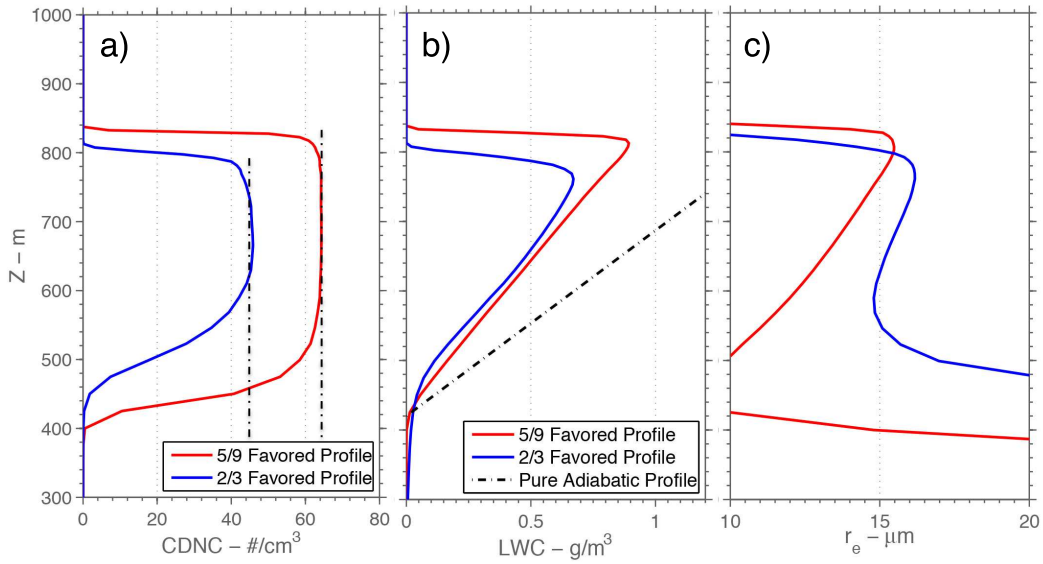

Figure 3.3: Median vertical profiles of (a) CDNC, (b) LWC, and (c) r_e for the DYCOMS-II scene from Figure 3.1(a) when divided into two LWP retrieval bias populations. The blue lines correspond to columns favoring the homogeneous vertical assumption ($C = 2/3$), and similarly the red lines correspond to the adiabatic vertical assumption ($C = 5/9$). The dash-dotted lines in panels (a) and (b) depict the constant CDNC assumption and the adiabatic LWC profile, respectively.

increase with height associated with the sub-adiabatic assumption. However, the most distinguishing feature of the two populations appears to be the vertical profile of r_e. Clearly, the LWP_{ad}-favored columns have simpler vertical profiles within the cloud layer, with r_e monotonically increasing from cloud base upward, unlike the LWP_{h}-favored columns, which have a more complex vertical profile of r_e. Below cloud base r_e is seen to increase rapidly downward for both populations. This signature is indicative of the predominant impact that growth from collisional-coalescence and vertical size sorting can have on the r_e profile at those levels.

Shifting from a physical profile perspective to an optical profile perspective, Figure 3.4 depicts the vertical profile of LWC and r_e as a function of cloud optical depth. Given that scattering exponentially attenuates reflected light as a function

of τ, it is appropriate to plot optical profiles logarithmically with respect to τ. What is evident from these optical profiles is that there is a region above cloud top (defined by the maximum LWC and indicated by the horizontal dashed line) where r_e is modestly reduced from its value at cloud top r_e^*. In this region LWC also transitions from its maximum at cloud top to its cloud-free value of zero as dry air from above cloud top becomes entrained and mixed with the upper region of the cloud. This reduction in LWC is indicative of inhomogeneous mixing or, more simply, dilution, in which mixing resolved by the model is faster than evaporation [*Baker and Latham*, 1979]. However, the modest reduction of r_e in this region also serves as an indicator that some evaporation is also occurring. Hereafter, we shall refer to this region as the cloud top transition zone. The peak LWC is used to define the base of the transition zone, which then extends upwards toward the optical cloud top ($\tau = 10^{-3}$). These artificial boundaries are intended to delimit the region influenced by cloud top entrainment. While the transition zone appears shallow in terms of physical thickness (Figure 3.3), the optical profile (Figure 3.4) reveals that the transition zone has a typical optical depth of 12. This is important because, as mentioned in subsubsection 2.2.1.1, strongly absorbing bands lead to retrievals exponentially weighted toward the uppermost region of the cloud. It follows that a transition zone of this thickness could impact the retrieved droplet size, and thus, it can indirectly influence LWP retrievals. However, the behavior of the transition zone does not appear to significantly differentiate the two retrieval-favoring populations. Looking toward the cloud base in Figure 3.4(b), it is clear that the two populations differ significantly. As Figure 3.4(c) reveals, this difference is absent after removing

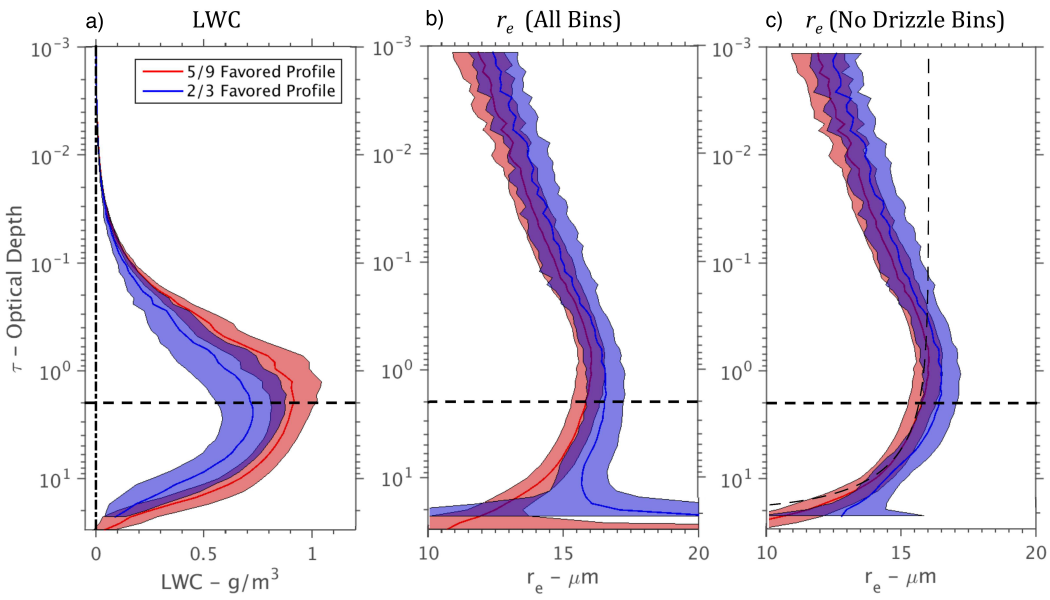

Figure 3.4: Optically binned profiles of (a) LWC, (b) r_e with drizzle bins included, and (c) r_e without contribution of drizzle bins from the DYCOMS-II case. The optical depths refer to the 3.75 μm band. As discussed in the text, drizzle is defined as drops larger than 30 μm. The lines denote median profiles of the columns that favor $\mathrm{LWP_{ad}}$ (red) and $\mathrm{LWP_h}$ assumptions (blue), while the enveloping contours around the curves denote the interquartile range (IQR) envelope centered about the median. In panel (b) the large IQR of the last two bins of the 2/3 favored profile fall well outside of the plotting range with values IQR = [16, 30.7] μm.

drizzle. In fact, the removal of drizzle leaves both profiles resembling one another, in addition to matching well with the form of the theoretical adiabatic profile (the black dash-dotted curve in Figure 3.4(c).

3.2.4 Impact of Drizzle and the Cloud Top Transition Zone

As discussed above, the cloud vertical profiles observed in these LES cases differ from adiabatic profiles mainly due the presence of drizzle and a cloud top transition zone. The impacts of these features on the LWP retrievals are explained using the hypothetical profiles of r_e shown in Figure 3.5. To make the explanation easier, we first define two reference effective radii, $r_e(5/9)$ and $r_e(2/3)$, by rearranging

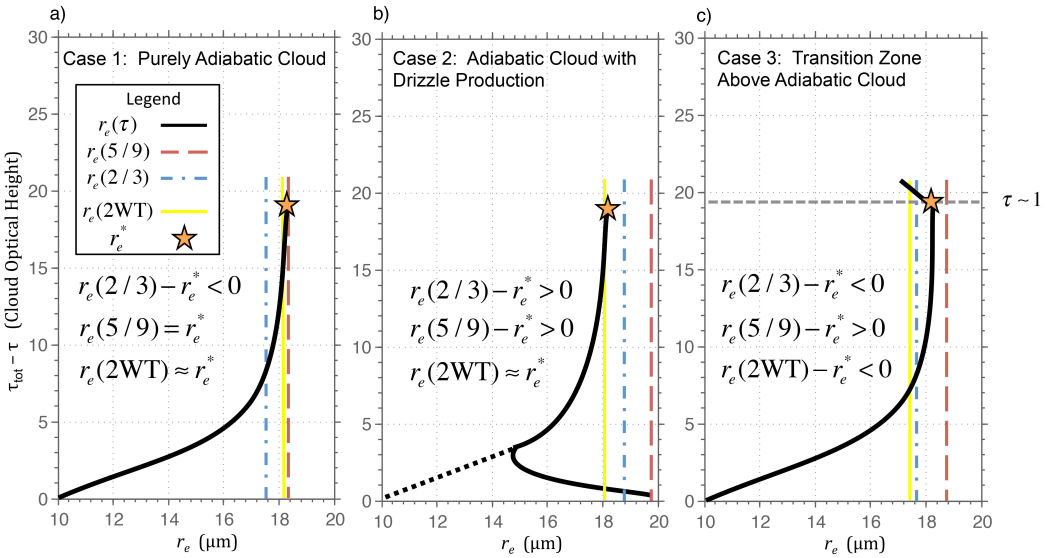

Figure 3.5: Several common cloud vertical profile cases in the LES. These optical profiles are defined in terms of cloud optical height to maintain consistency between the characteristic equation describing an adiabatic vertical profile. The vertical blue and red dash-dotted lines represent the value of the vertical profile assumption-required droplet sizes $r_e(2/3)$ and $r_e(5/9)$ respectively. The yellow line represents the value of the optical retrieval $r_e(2\text{WT})$ and the gray dashed line in panel (c) represents the location of the base of the transition zone. The yellow star represents both the location and value of the cloud top droplet size r_e^*.

Equation 3.1 and substituting the appropriate constant as well as the LWP and τ_{tot} from the LES:

$$r_e(5/9) = \frac{9}{5}\frac{\text{LWP}_{\text{LES}}}{\rho_l \tau_{\text{tot,LES}}}, \tag{3.11}$$

$$r_e(2/3) = \frac{3}{2}\frac{\text{LWP}_{\text{LES}}}{\rho_l \tau_{\text{tot,LES}}}. \tag{3.12}$$

These are the droplet sizes that are required to complete the assumed relationship between LWP, r_e, and τ_{tot} for either of the vertical profile assumptions. These droplet sizes serve as litmus tests: If the in situ cloud top droplet effective radius, r_e^*, better matches with $r_e(5/9)$ than with $r_e(2/3)$, then the LES column favors LWP_{ad} vertical profile assumptions and where closer to $r_e(2/3)$ it favors LWP_{h} vertical

assumptions. The ideal adiabatic profile in Figure 3.5(a) demonstrates that r_e^* and $r_e(5/9)$ would perfectly match when the actual profile is adiabatic. This stands in contrast with $r_e(2/3)$, which is smaller because the $\mathrm{LWP_h}$ profile assumption overestimates the actual LWP. In addition to the vertical profile assumed in the LWP calculation, there is also the impact of vertical weighting on the underlying droplet size retrieval. For the adiabatic profile in Figure 3.5(a), $r_e(2\mathrm{WT})$ matches r_e^* very well, indicating that the vertically weighted droplet size would provide a reasonable estimate of the cloud top droplet size for such a cloud. The comparisons of $r_e(5/9)$ and $r_e(2\mathrm{WT})$ to r_e^* indicate, as expected, that the adiabatic retrieval provides an accurate representation of $\mathrm{LWP_{LES}}$ for an adiabatic cloud. A second hypothetical case seen in Figure 3.5(b) adds complexity by including drizzle near cloud base to mimic the cloud profiles from the LES as seen in Figure 3.3 and Figure 3.4. In this case the retrieval proxy $r_e(2\mathrm{WT})$ is still a good match to cloud top r_e^* because the SWIR band reflectance saturates near cloud top and is largely insensitive to the presence of drizzle lower in the cloud. However, as demonstrated in the schematic, the presence of drizzle can cause both $r_e(5/9)$ and $r_e(2/3)$ to be larger than r_e^* in proportion to the amount of LWP in the drizzle mode. This bias reflects the increase in the ratio of $\mathrm{LWP_{LES}}$ to $\tau_{\mathrm{tot,LES}}$ in Equation 3.11 and Equation 3.12. This shift in the ratio occurs because $\mathrm{LWP_{LES}}$ is sensitive to the increase in the $r_e(\tau)$ profile lower in the cloud, as indicated in the integral in Equation 2.34. It follows that a high bias of $r_e(2/3)$ indicates that, compared to $\mathrm{LWP_{LES}}$, the $\mathrm{LWP_h}$ retrieval would be biased low and the $\mathrm{LWP_a}$d lower yet. With that in mind, a positive $r_e(2/3) - r_e^*$ bias can serve as an indicator of the influence of drizzle on

vertical profile. A third hypothetical case, shown in Figure 3.5(c), addresses the impact of the cloud top transition zone. In this zone, r_e decreases modestly with height (increases with optical depth for $\tau < 2$) from the value at cloud top, r_e^* . The optical thickness of this transition zone is large enough to influence the vertically weighted retrieval, $r_e(2\text{WT})$, which would be low biased relative to r_e^* . A low bias in the cloud top r_e retrieval would subsequently lead to a low bias in both LWP calculations. In contrast, to the extent that the transition zone is optically thin, $r_e(2\text{WT})$ would serve as an accurate description of the cloud top droplet size.

Considering the impacts of the cloud top transition zone and drizzle we now ask, what happens to LWP retrieval biases when these two features are removed from an LES cloud scene? If it were correct to treat these features as the primary drivers of non-adiabatic cloud profiles, then we would expect adiabatic retrieval assumptions to better match the actual LWP upon the removal of these features. To organize these comparisons, we introduce two r_e biases: (1) a profile bias, which compares the vertical profile retrieval assumptions with LES profiles, and (2) a retrieval bias, which compares the vertically weighted 2WT retrieval proxy to LES profiles:

$$r_e \text{ profile bias} \equiv r_e(5/9) - r_e^*, \tag{3.13}$$

$$r_e \text{ retrieval bias} \equiv r_e(2\text{WT}) - r_e^*. \tag{3.14}$$

These two biases are used to identify features of the schematics in Figure 3.5 and allow for the intercomparison of retrieval uncertainty associated with droplet size retrievals (retrieval bias) and profile assumptions in LWP retrievals (profile bias).

This method is convenient because it decouples sensitivity to drizzle and the transition zone. The profile bias is primarily sensitive to the presence of drizzle because of its influence on $r_e(5/9)$ due to the changing vertical profile of $r_e(\tau)$ Figure 3.5(b), whereas the retrieval bias is primarily sensitive to the impact of the transition zone at the cloud top because of the vertically weighted droplet size retrieval Figure 3.5(c). Each bias is compared relative to the droplet size at the peak LWC, r_e^* , as a point of reference.

With the retrieval and profile biases as diagnostics we can now examine what happens to the quality of LWP retrievals as these two features are removed from an LES scene. The removal of drizzle involves simply removing droplets in size bins larger than the 30 μm cutoff from all LES quantities and subsequent retrievals, while the transition zone removal is accomplished by excluding this region at the top of the cloud from the LES LWP and optical thickness as well as the r_e(2WT) retrieval proxy. This removal experiment is performed sequentially, with drizzle removed first, followed by the transition zone. It should be noted that the order of the sequence was determined to be unimportant because the biases from drizzle and the transition zone are sufficiently decoupled. As depicted in Figure 3.6, the joint analysis of the profile and retrieval biases demonstrates how sequential removal of drizzle and the transition zone influence LWP retrievals. For example, the impact of drizzle can be understood by looking at the points around upper horizontal dashed line, which denotes the location of zero bias for $r_e(2/3) - r_e^*$ on the $r_e(5/9) - r_e^*$ axis. As mentioned previously, drizzle can induce a positive bias in $r_e(2/3)$ and an even greater bias in $r_e(5/9)$ (refer to Figure 3.5(b)). Removal of drizzle removes

nearly all occurrences of positive $r_e(2/3) - r_e^*$, as evidenced by the change in bias between the scatter plots in Figure 3.6(a) and (b). In the final removal step, after the transition zone is removed in Figure 3.6(c), there is a drastic improvement in the retrieval bias resulting in almost no dispersion and only a slight negative bias. The removal of drizzle and entrainment zone features causes the DYCOMS-II case to go from nearly a $50 - 50$ split regarding favored vertical profile assumption to more than 95% in favor of the adiabatic vertical profile assumption. The fraction of the DYCOMS-II columns favoring adiabatic, homogeneous, or neither retrieval assumption is shown in the first row of Table 3.1 for each of the removal experiment steps. It is worth noting that the remaining columns that favor homogeneous vertical assumptions appear to be located near cloud holes where entrainment of dry air can occur through the side of the cloud. It thus appears plausible that the transition zone at horizontal cloud boundaries can contribute to LWP retrieval bias as well.

As already mentioned, previous studies have indicated that bispectral LWP retrieval bias is dependent on cloud regime. Thus far, we have highlighted a single LES case (DYCOMS-II) and snapshot, but an examination of the other LES cases offers the opportunity to study how another MBL cloud regime is influenced by vertical profile assumptions. A comprehensive view of the model cases and time slices requires a statistical approach. The mean bias for a case represents the systematic bias from vertical profile and retrieval assumptions, and the standard deviation of the bias is associated with the variability within the LES. The results, provided in Table 3.3, further demonstrate that the relative importance of drizzle and the transition zone are associated with cloud regime. These results are also informed

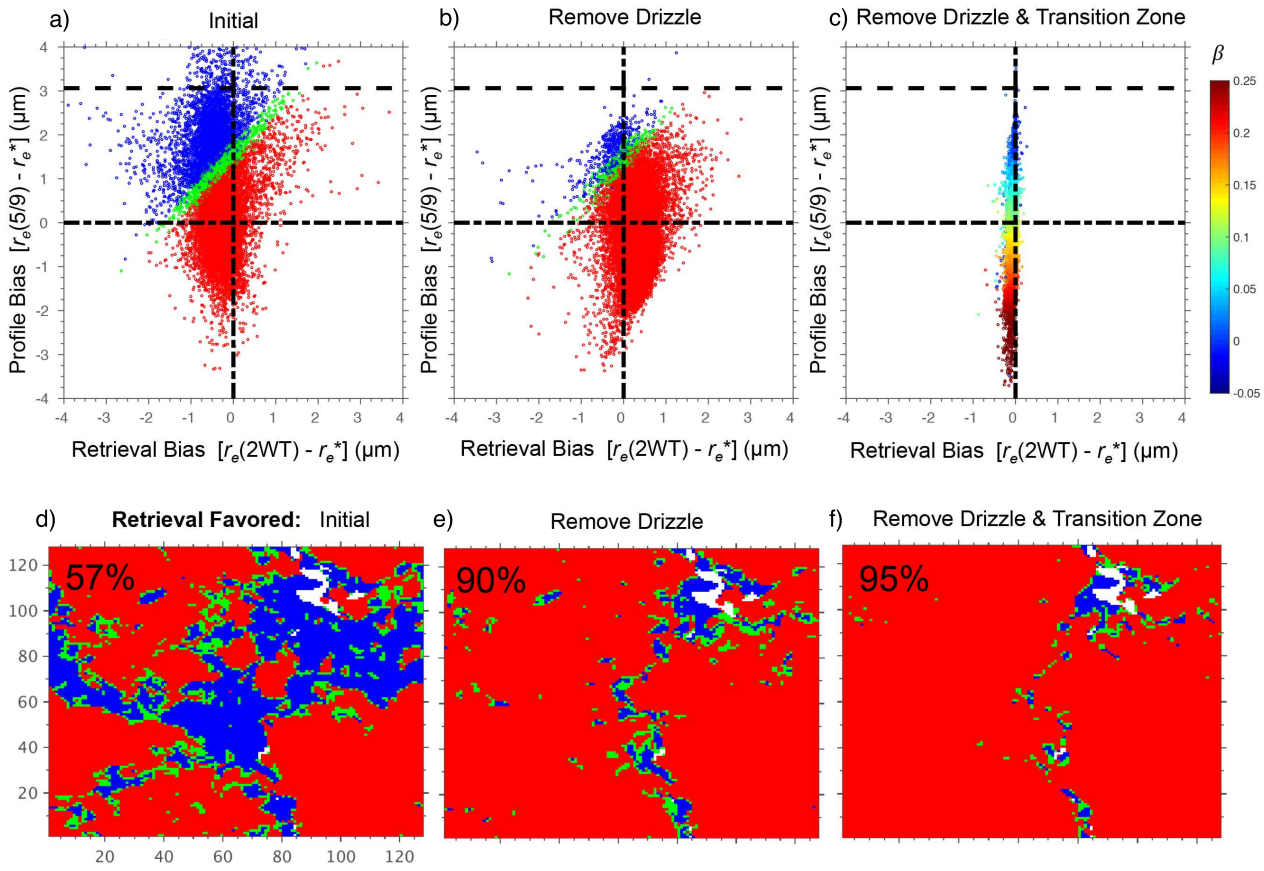

Figure 3.6: The sequential removal analysis for the DYCOMS-II LES scene introduced in Figure 3.1(a) The impact of the removal of drizzle and then transition zone on the profile and retrieval biases. The dash-dotted lines in (a)(c) denote neutral bias, whereas the horizontal dashed line denotes the value of $r_e(5/9)$ profile bias that corresponds to neutral $r_e(2/3)$ profile bias. The color of the points in panel (a) and (b) are associated with the retrieval quality maps in panel (d) and (e), where red denotes LWP retrievals favoring $\mathrm{LWP_{ad}}$, blue with $\mathrm{LWP_h}$, and green with neither. Note that the retrieval quality map in panel (d) corresponds to the contours in Figure 3.1(a). The inset percentages indicate the share of pixels that favor $\mathrm{LWP_{ad}}$. The color of points in panel (c) depict the droplet optical growth exponent, β (see text), after (f) drizzle and the transition zone features have been omitted.

by the cloud fraction and LWP information in Table 3.2. For the DYCOMS-II case, the overall reduction of mean and standard deviation of biases indicates that the removal of both features leads toward increasing agreement with adiabatic retrieval assumptions. The statistical results from the ATEX cases do not exhibit the same behavior. As we saw before, the ATEX clean case strongly favors homogeneous retrievals at the outset. The contribution of drizzle to LWP in this case is appreciable (see Table 3.2), and as a consequence, the removal of drizzle leads to a reduced mean and standard deviation of profile biases. The ATEX clean case does not converge toward adiabatic assumptions by the final removal step and the remaining regions that do not favor adiabatic assumptions are narrow, lie in the vicinity of cloud edge, and surround thick convective cores that favor adiabatic assumptions (not shown). As mentioned previously, horizontal cloud boundaries near cloud holes are potentially influenced by entrainment horizontally as well as from cloud top. The low cloud fraction in this case (see Table 3.2) increases the prevalence of horizontal cloud boundaries making it difficult to distinguish the influence of entrainment and drizzle in these regions. For the ATEX clean case homogeneous assumptions yield less bias than the adiabatic assumptions when drizzle is prominent. However, in the ATEX polluted case, which lacks drizzle (see Table 3.2), the retrievals are little affected by omitting it. The retrieval assumption favored by the ATEX polluted case is not driven by a systematic (mean) bias, as was the case for the DYCOMS-II and ATEX clean cases. Instead, the rather large variability (standard deviations) in both biases leads to instances where either of the LWP retrieval assumptions satisfy portions of the population. Upon removal of the entrainment features the ATEX polluted case

LES Case	Cloud Fraction	Median LWP (g/m^2)	%LWP (Drizzle)
DYCOMS-II	99.4%	163.6	4.0%
ATEX clean	34.8%	71.5	13.0%
ATEX polluted	40.2%	35.6	$< 0.1\%$

Table 3.2: Aggregated statistics for each of the LES cases including: cloud fraction, median LWP , and percent of LWP associated with drizzle. All properties are listed for the initial state of each LES scene before the removal experiment.

clearly favors adiabatic retrievals, as indicated in Table 3.1. However, as with the ATEX clean case, the majority of columns that do not favor adiabatic retrievals are again found near horizontal cloud boundaries (not shown). To summarize some of the foregoing discussion, major distinctions between the ATEX clean and polluted cases can be drawn. The first is that while drizzle plays a dominant role in the clean case, it is negligible in the polluted case. The second is that the polluted case has significantly fewer columns associated with cloud horizontal boundaries and favors adiabatic retrievals more on the whole after removal of entrainment features. The varied difference in these findings across just these three cases demonstrates that bispectral LWP retrieval biases depend on cloud regime as well as the presence of drizzle. Furthermore, the differences highlight the fact that there is no single vertical profile assumption suitable for all of these cloud regimes.

The evaluation of retrieval and profile bias statistics in terms of r_e is useful for identifying and comparing the physical causes of LWP retrieval bias, but it does not directly relate these biases to the magnitude of the associated LWP bias. To address

	r_e Bias Statistics (μm)					
	Profile Bias $[r_e(5/9) - r_e^*]$			Retrieval Bias $[r_e(2\text{WT}) - r_e^*]$		
LES case	Original Scene	Removal of Drizzle	Removal of Drizzle & Transition Zone	Original Scene	Removal of Drizzle	Removal of Drizzle & Transition Zone
DYCOMS-II	$\mu = 0.55$ ($\sigma = 1.03$)	$\mu = -0.0704$ ($\sigma = 0.840$)	$\mu = -0.254$ ($\sigma = 0.832$)	$\mu = -0.217$ ($\sigma = 0.401$)	$\mu = -0.232$ ($\sigma = 0.409$)	$\mu = -0.0696$ ($\sigma = 0.0597$)
ATEX Clean	$\mu = 2.84$ ($\sigma = 2.51$)	$\mu = 1.38$ ($\sigma = 1.37$)	$\mu = 1.30$ ($\sigma = 1.65$)	$\mu = 0.393$ ($\sigma = 1.96$)	$\mu = -0.324$ ($\sigma = 1.21$)	$\mu = -0.016$ ($\sigma = 0.311$)
ATEX Polluted	$\mu = 0.122$ ($\sigma = 0.586$)	$\mu = 0.124$ ($\sigma = 0.585$)	$\mu = 0.084$ ($\sigma = 0.610$)	$\mu = -0.107$ ($\sigma = 0.681$)	$\mu = -0.108$ ($\sigma = 0.681$)	$\mu = -0.0066$ ($\sigma = 0.0752$)

Table 3.3: Aggregate statistics for the profile and retrieval bias of r_e. Rows are as in Table 3.1, while columns are broken into sections for profile and retrieval biases, which are then broken down into subsections by removal step. The mean and standard deviation are indicated by μ and σ

this, we also define LWP profile and retrieval biases, which couples r_e variability and τ_{tot} variability. The LWP profile and retrieval biases are defined as follows:

$$\text{LWP profile bias} \equiv \frac{5}{9}\rho_l r_e^* \tau_{\text{LES}} - \text{LWP}_{\text{LES}}, \tag{3.15}$$

$$\text{LWP retrieval bias} \equiv \frac{5}{9}\rho_l r_e(2\text{WT})\tau_{\text{LES}} - \text{LWP}_{\text{LES}}. \tag{3.16}$$

The LWP profile and retrieval biases, shown in Table 3.4, help to put the previous analysis in the context of retrieval outcomes and furthers our arguments about the impact of profile on cloud retrievals. In the presence of drizzle, the LWP profile bias is negative, while the presence of an optically thick transition zone can cause the LWP retrieval bias to be negative as a secondary effect of low-biasing cloud top droplet size retrievals (refer to $r_e(2\text{WT})$ in Figure 3.5(c). Removal of both of these features leads to LWP_{ad} retrievals that are biased low relative to actual LWP. Mean LWP biases are seen in Table 3.4 to range from values as large as $10\,\text{g/m}^2$before the features are removed, to values on the order of $1\,\text{g/m}^2$ after removal. Thus, adiabatic

	LWP Bias Statistics (g/m^2)					
	Profile Bias [LWP(5/9) − LWP$_{\mathrm{LES}}$]			Retrieval Bias [LWP(2WT) − LWP$_{\mathrm{LES}}$]		
LES case	Original Scene	Removal of Drizzle	Removal of Drizzle & Transition Zone	Original Scene	Removal of Drizzle	Removal of Drizzle & Transition Zone
DYCOMS-II	$\mu = -5.79$ ($\sigma = 8.81$)	$\mu = 2.89$ ($\sigma = 7.70$)	$\mu = 4.41$ ($\sigma = 7.31$)	$\mu = -2.64$ ($\sigma = 3.61$)	$\mu = -2.76$ ($\sigma = 3.64$)	$\mu = -0.990$ ($\sigma = 0.575$)
ATEX Clean	$\mu = -9.92$ ($\sigma = 12.4$)	$\mu = -0.834$ ($\sigma = 7.88$)	$\mu = 1.95$ ($\sigma = 8.09$)	$\mu = -3.37$ ($\sigma = 9.15$)	$\mu = -5.76$ ($\sigma = 11.8$)	$\mu = -2.70$ ($\sigma = 3.83$)
ATEX Polluted	$\mu = -0.63$ ($\sigma = 4.29$)	$\mu = 0.368$ ($\sigma = 4.71$)	$\mu = 0.878$ ($\sigma = 4.71$)	$\mu = -1.33$ ($\sigma = 7.23$)	$\mu = -1.33$ ($\sigma = 7.40$)	$\mu = -0.0156$ ($\sigma = 0.0712$)

Table 3.4: As in Table 3.3 but for LWP.

assumptions in cloud retrievals can lead to LWP biases on the order of 10-20% in the presence of drizzle and the cloud top transition zone. As with the r_e biases, the mean LWP profile and retrieval biases show improvement as well as a reduction in their standard deviation as the features are removed. The remaining variability in these biases and their dependence on cloud regime are likely attributable to unaccounted behavior in the passive LWP retrieval technique, i.e., the assumption that the droplet number concentration is constant throughout the cloud, which we consider next.

3.2.5 Vertical Profile Variability

Beyond the impact of drizzle on the re profile bias the large variability remaining after removal of drizzle and entrainment features remains unexplained. For the adiabatic retrieval, this variability suggests that there are additional aspects of the simulated clouds that are inconsistent with adiabatic assumptions. In an attempt to explain this variability, we return to the adiabatic profile described in Equation 2.41

and note that the profile of $r_e(\tau)$ can be expressed as a simple power law relationship

$$r_e(\tau) = \alpha \left(\frac{\tau_{\text{tot}} - \tau}{\tau_{\text{tot}}} \right)^{\beta} \tag{3.17}$$

Hereafter, we refer to the exponent, β, as the "droplet optical growth exponent," or sometimes "growth exponent" for the sake of brevity. For an adiabatic profile the value of the droplet optical growth exponent is $\beta_{\text{ad}} = 1/5 = 0.2$. Taking the logarithm of both sides of Equation 3.17, solving for β, and taking a derivative yields an expression with fewer unknown constants:

$$\beta = \frac{\text{dlog}\,(r_e)}{\text{dlog}\,(\tau_{\text{tot}} - \tau)}. \tag{3.18}$$

If β was constant throughout the cloudy column, then Equation 3.18 results in the droplet growth exponent in Equation 3.19, which now describes β in terms of $r_e(\tau)$, the total optical thickness and the cloud top droplet size.

$$\beta = \frac{\log\,(r_e^*) - \log\,(r_e)}{\log\,(\tau_{\text{tot}}) - \log\,(\tau_{\text{tot}} - \tau)} = \frac{\log\,(r_e^*/r_e)}{\log\,(\tau_{\text{tot}} - \tau)}. \tag{3.19}$$

A recasting of Equation 3.17 avoids the constant α,

$$r_e(\tau) = r_e^* \left(\frac{\tau_{\text{tot}} - \tau}{\tau_{\text{tot}}} \right)^{\beta}. \tag{3.20}$$

This is the same form as Equation 2.41, and as we did before with the adiabatic case in Equation 2.42, the integral form of the LWP equation in Equation 2.34 can

be used to derive a more general LWP expression that includes our definition of the droplet growth exponent,

$$\begin{aligned} \mathrm{LWP} &= \frac{2}{3}\rho_l \int_0^{\tau_{\mathrm{tot}}} r_e(\tau)\,\mathrm{d}\tau\,, \\ &= \frac{2}{3}\rho_l \frac{1}{\beta+1} r_e^* \left(\frac{1}{\tau_{\mathrm{tot}}}\right)^{\beta} (\tau_{\mathrm{tot}})^{\beta+1}\,, \\ &= \frac{2}{3}\rho_l \frac{1}{\beta+1} r_e^* \tau_{\mathrm{tot}}\,. \end{aligned} \tag{3.21}$$

In practice, we can calculate the value of β discretely between each layer of the LES, as expressed in Equation 3.22, in which β depends on the LES vertical grid index i,

$$\beta_i = \frac{\log(r_{e,i}) - \log(r_{e,i+1})}{\log(\tau_{\mathrm{tot}} - \tau_i) - \log(\tau_{\mathrm{tot}} - \tau_{i+1})}\,. \tag{3.22}$$

We then compute a vertically weighted average of β with the weighted sum of each layer by its contribution to the optical thickness,

$$\beta = \frac{\sum_{i=1}^{N-1} \beta_i \Delta\tau_{i,i+1}}{\tau_{tot}}\,. \tag{3.23}$$

It is clear from Equation 3.21 that values of $\beta = 0$ and $\beta = 1/5 = 0.2$ lead to the respective definitions of LWP for homogeneous and adiabatic vertical profiles that were introduced in Equation 3.2 and Equation 3.3. As was evident from Figure 3.6(c) the value of β associated with zero adiabatic profile bias is somewhat smaller ($\beta \approx 0.13$) than the expected adiabatic value, ($\beta_{\mathrm{ad}} \equiv 0.2$). Perhaps the most striking feature in Figure 3.6(c) is the broad variability in the droplet optical

growth exponent. We speculate that this variability in growth exponent can be associated with the sensitivity to other implicit assumptions in Equation 2.41. Evidently, many of the DYCOMS-II LES profiles have been modified by diabatic processes (i.e., precipitation and radiative heating) leading to violation of two implicit assumptions of the adiabatic model. First, the cloud droplet number concentration is not consistently vertically uniform. Second, the dispersion of the cloud droplet size distribution is also not vertically uniform. To address this, it is important to introduce the complete expression for the adiabatic profile of r_e,

$$r_{e,ad}(\tau) = \left[\frac{5}{3}\frac{1}{Q_e}\left(\frac{4}{3}\pi\rho_l\frac{1}{f\,\Gamma_{\mathrm{LWC}}}\right)\frac{1}{(kN)^2}\frac{\tau_{\mathrm{tot}}-\tau}{\tau_{\mathrm{tot}}}\right]^{1/5}. \tag{3.24}$$

The adiabatic $r_e(\tau)$ relationship presented here is a result of the relationship between adiabatic LWC(z), $r_e(z)$, and $\tau(z)$ profiles that has been described throughout the literature numerously [*Pontikis and Hicks*, 1993; *Pontikis*, 1996; *Szczodrak et al.*, 2001]. A detailed derivation of this relationship can be found appendix A of *Boers et al.* [2006]. Additional constants are introduced in the adiabatic $r_e(\tau)$ profile, like the degree of adiabaticity and adiabatic LWC lapse rate (f and Γ_{LWC}, respectively); a measure of the droplet size distribution dispersion (k) [*Brenguier et al.*, 2011]; and the CDNC (N). As mentioned previously, the adiabatic vertical profile assumption hinges on two implicit assumptions: the effective CDNC ($N_e = kN$) is constant and the droplet size retrieval used is similar to the cloud top droplet size, r_e^*. The observed variability in the values of the droplet optical growth parameter, β, can be attributed to the breakdown of these assumptions. If we assume that both $N(\tau)$

and $k(\tau)$ can also be treated as power law relations, we get the following profiles:

$$N(\tau) \equiv N_0 \left(\frac{\tau_{\text{tot}} - \tau}{\tau_{\text{tot}}} \right)^{\eta}, \tag{3.25}$$

$$k(\tau) \equiv \left(\frac{r_v(\tau)}{r_e(\tau)} \right)^3 = k_0 \left(\frac{\tau_{\text{tot}} - \tau}{\tau_{\text{tot}}} \right)^{\kappa}, \tag{3.26}$$

where the new exponents η and κ can be determined in the same manner as was outlined for β. Referring back to the adiabatic vertical profile in Equation 2.41 and Equation 3.24, we can reform Equation 3.17 to account for the profiles of $N(\tau)$ and $k(\tau)$,

$$\begin{aligned} r_e(\tau) &= \frac{\alpha}{[k(\tau) N(\tau)]^{2\beta}} \left(\frac{\tau_{\text{tot}} - \tau}{\tau_{\text{tot}}} \right)^{\beta}, \\ &= \frac{\alpha}{[k_0 N_0]^{2\beta}} \left(\frac{\tau_{\text{tot}} - \tau}{\tau_{\text{tot}}} \right)^{\beta}. \end{aligned} \tag{3.27}$$

It should be noted that Equation 3.27 becomes equivalent to Equation 2.41 if η and κ are each zero, which of course leads to both k and N being vertically homogeneous (i.e., constant). Nonzero η and κ can lead to a new definition for a reduced effective droplet growth exponent:

$$r_e(\tau) = \alpha' \left(\frac{\tau_{\text{tot}} - \tau}{\tau_{\text{tot}}} \right)^{\beta'}, \tag{3.28}$$

$$\beta' = \beta \left[1 - 2(\eta + \kappa) \right]. \tag{3.29}$$

Hereafter, we will refer to the value of β measured from the LES profile as β' in recognition that it represents a modified adiabatic profile. As previously noted,

the DYCOMS-II case displayed a reduced droplet growth exponent of $\beta' \approx 0.13$ associated with the minimum adiabatic profile bias in Figure 3.6(c). This clearly contradicts the theoretical adiabatic value of $\beta_{\text{ad}} = 1/5 = 0.2$. If we consider the median LES values of the two other exponents, $\eta = 0.039$ and $\kappa = 0.048$, respectively, and an initial droplet growth exponent of $\beta = 0.2$ then Equation 3.29 results in a modified growth exponent of $\beta' = 0.165$. This result, while offering an explanation for the low bias in β values for adiabatic assumptions, still does not explain the source of the broad variability the droplet optical growth rate in Figure 3.6(c). To that end, joint histograms of β' in Figure 3.7 with respect to both η and κ reveal that β' is sensitive to the observed values of η and κ. The relationship between of η and β' in Figure 3.7(a) indicates that much of the broad variability in β' can be traced back to the broadly distributed values of η observed in the LES. While Figure 3.7(b) reveals that much of the reduction in the mean value of β' comes from the strong linear dependence of β' on κ.

3.3 Discussion

Throughout this study several key assumptions are made in order to study the influence of cloud vertical profile on retrievals of cloud LWP: The removal of droplets larger than 30 μm is representative of a cloud without drizzle. The vertically weighted r_e(2WT) is an appropriate proxy for the r_e(3.7 μm) bispectral retrieval. The transition zone appropriately represents the region of the cloud impacted by local entrainment.

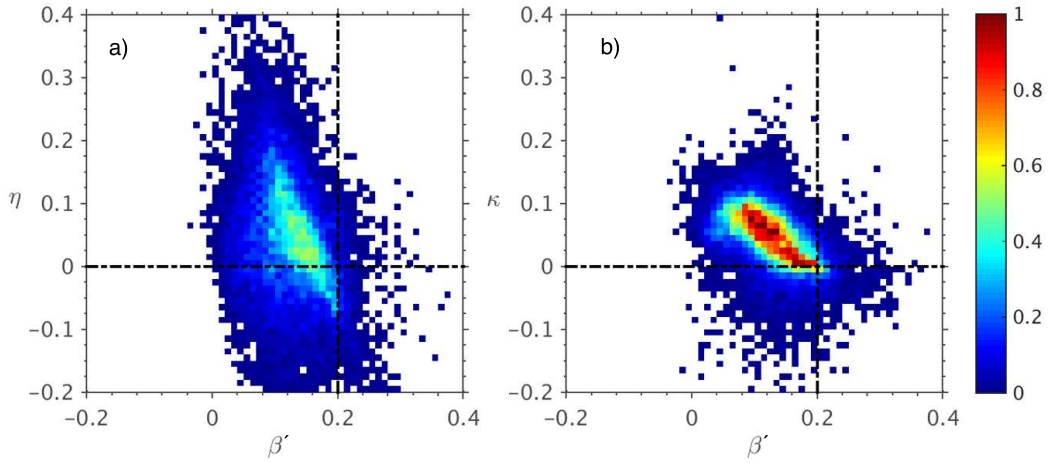

Figure 3.7: Joint histograms of the droplet growth exponent β' and both of the exponents η and κ introduced in Equation 3.25 and Equation 3.26, respectively. All quantities are from the LES profiles. The histogram is binned in 0.01 intervals and the color scale is stated in percent. The median values of both η and κ are 0.039 and 0.048 respectively. The dash-dotted lines denote the adiabatic assumptions for each of these exponents.

The validity of the drizzle assumption was tested directly by turning off collisional-coalescence processes during a DYCOMS-II LES run. The resulting microphysical snapshots revealed that the suppression of droplet growth into drizzle led to a profile bias that was only slightly more reduced than it was by removing drizzle bins. Thus, it is likely that the impact of drizzle on cloud vertical profile assumptions is slightly greater (on the order of a few $\mathrm{g/m^2}$) than predicted in this study. The assumption regarding vertical weighting of the 3.7 μm SWIR band can be tested by explicitly using $r_e(3.7\,\mu\mathrm{m})$ in the definition of the retrieval bias in Equation 3.14 rather than $r_e(\mathrm{2WT})$. The bias scatterplots in Figure 3.8 correspond to this new definition for the retrieval bias. In contrast to the $r_e(\mathrm{2WT})$ retrieval bias, Figure 3.8(a) reveals that, on average, $r_e(3.7\,\mu\mathrm{m})$ has a slight positive bias. A comparison of Figure 3.6(c) and Figure 3.8(c) also reveals that removal of transition zone features does not dramatically reduce the retrieval bias of $r_e(3.7\,\mu m)$. While it may appear that $r_e(\mathrm{2WT})$

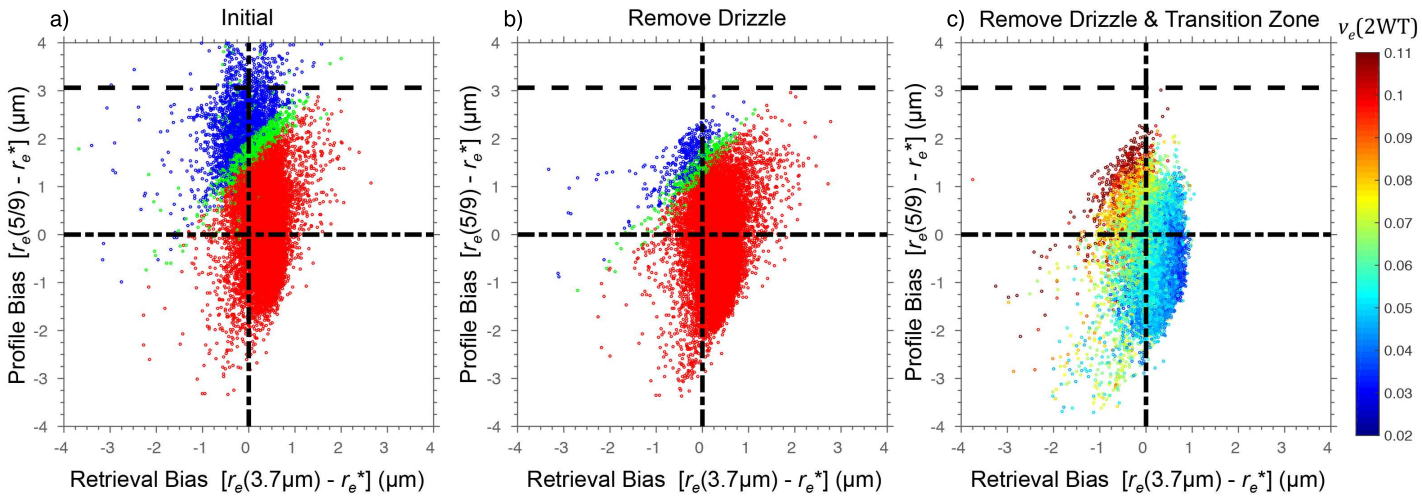

Figure 3.8: Just as in Figure 3.6, these profile and retrieval bias scatter plots depict the sequential removal experiment of the DYCOMS-II case snapshot. The difference between the two figures is that the x-axis depicts the bias of bispectral retrieval $r_e(3.7\,\mu m)$ rather than the vertically weighted r_e(2WT). Panels (a) and (b) the color of the points is as in Figure 3.6; and in panel (c) the color of the points corresponds to the vertically weighted retrieval, v_e(2WT). Refer to Figure 3.6 for the description of lines and coloration.

and $r_e(3.7\,\mu m)$ are not perfect analogues, it is important to note the correlation of the $r_e(3.7\,\mu m)$ retrieval bias with the value of v_e(2WT) in Figure 3.8(c). This implies that distinguishing the impact of the bispectral v_e assumption from the accuracy of the vertical weighting assumptions could be problematic. The impact of the bispectral v_e assumption will be discussed further on in this section with regard to polarimetric retrievals of r_e and v_e.

The removal of the transition zone is assumed to isolate the core of the cloud from the region that could be influenced by cloud top entrainment. While a rigorous definition of this region requires characterization of both the dynamics and microphysics, it is outside the scope of this retrieval study to identify the dynamical causes of the transition zone. We have instead inferred the presence of this feature from the microphysical properties in the LES snapshots because of the clearly

altered microphysics of this region. Resolving the transition zone in this manner can be complicated by the coarseness of the vertical resolution of the LES. This is especially true for the resolution of the ATEX cases where situations can occur such that the optical cloud top and transition zone base cannot be distinguished from one another. Thus, for the ATEX cases, the impact of the removal of the transition zone on the retrieval bias can only serve as a low estimate.

While this work has primarily focused on bispectral LWP retrievals, the core concept behind this passive retrieval technique is likely to be extended to future spaceborne polarimetric instruments. The work of *Alexandrov et al.* [2012a] as well as our own polarimetric simulator studies in (refer to chapter 4) has demonstrated that vertically weighted retrieval proxies, [r_e(2WT), v_e(2WT)], compare well with polarimetric retrievals, [r_e(pol), v_e(pol)] Figure 3.9 and Figure 3.10. The spatial distributions of all of the r_e microphysical retrieval techniques are shown in Figure 3.10(a-c). The similarities between r_e(2WT) and r_e(pol) imply that polarimetric retrievals may exhibit a similar sensitivity to the removal of the transition zone. It follows that a cursory understanding of the impact of cloud vertical profile on polarimetric and spectral retrievals can be obtained from this study. For example, the comparison between the retrieval biases in Figure 3.6(c) and Figure 3.8(c) may also imply that the standard deviation of the retrieval bias for r_e(pol) would be much less than for $r_e(3.7\,\mu m)$. This difference in the accuracy of the retrieval bias occurs in part because r_e(2WT) and r_e(pol) make no explicit assumption about the value of v_e. As the scatterplot in Figure 3.8(c) revealed, v_e(2WT) is correlated with the value of the $r_e(3.7\,\mu m)$ retrieval bias, and this correlation is also demonstrated

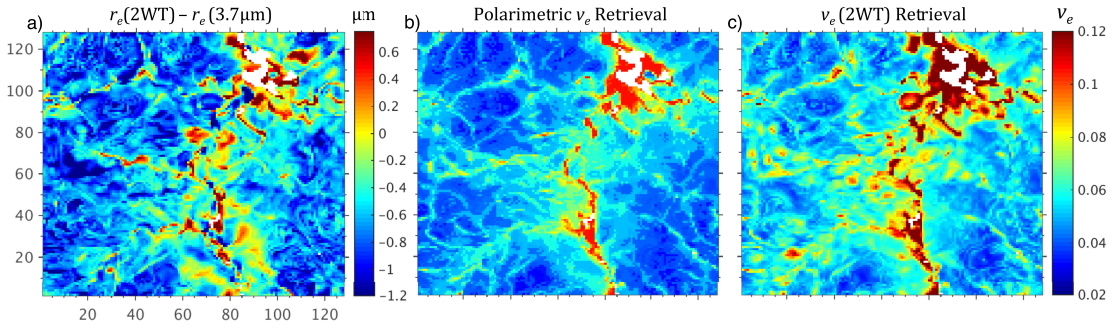

Figure 3.9: Droplet microphysical retrieval scenes from the DYCOMS-II case. (a) The bias between the 2WT and bispectral r_e retrievals; retrieval of v_e via the (b) polarimetric method and (c) vertically weighted retrieval proxy are shown. The lack of sensitivity for the polarimetric v_e retrieval above values of 0.11 is not physical but instead due to retrieval algorithm limitations.

spatially in the comparison of Figure 3.9(a,c). This systematic broadening of the bias indicates that the bispectral assumption of $v_e = 0.1$ results in a lack of sensitivity to the removal of the transition zone. In contrast, the r_e(2WT) bias (and r_e(pol)) clearly improves after removing the transition zone. Thus, polarimetric retrievals of LWP may have to take into consideration the impact that the cloud top transition zone might have on retrieval quality. Further study on the sensitivity of polarimetric retrievals to the cloud top transition may be necessary for future polarimetric campaigns like those of NASAs upcoming Pre-Aerosol Clouds and ocean Ecosystem (PACE) mission and ESAs Multiviewing Multichannel Multipolarization (3MI) mission. It should be noted that for MODIS cloud products the bias due to the v_e assumption does not substantially impact the r_e retrieval compared to other sources of bias (i.e., cloud inhomogeneity or 3-D effects). In the MODIS Collection 6 cloud products, the uncertainty associated with the v_e assumption is included in the determination of the retrieval uncertainty data products.

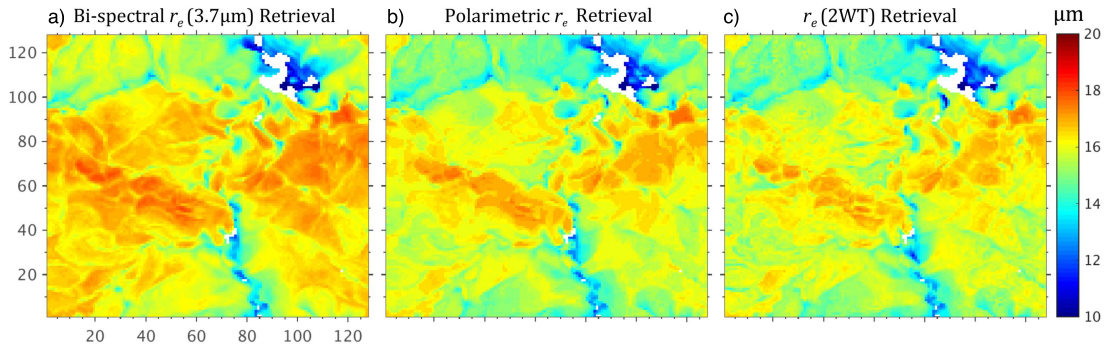

Figure 3.10: Droplet effective radius retrievals from the DYCOMS-II case for a variety of retrieval techniques. The retrievals displayed have been obtained using the (a) bispectral method, (b) the polarimetric method, and (c) the vertically weighted retrieval proxy.

3.4 Conclusions

The LES cloud retrieval simulator used in this study has allowed us to probe the impact of cloud vertical structure on passive LWP retrievals for marine boundary layer clouds in two regimes: trade wind cumulus and subtropical stratocumulus. With regard to the three questions that motivated this study we have found the following:

1. The vertical profile assumption (homogeneous or adiabatic) most appropriate for LWP retrieval depends on cloud regime (cumuliform or stratiform).

2. The vertical profiles of the LES cloud cases were quite varied, with some dominated by strong drizzle production and others by the microphysical impact of entrainment. Each of these features was found to bias LWP retrievals low, leading to a more favorable retrieval for homogeneous vertical profile assumptions.

3. The theoretical framework developed here defines LWP in terms of an arbitrary droplet vertical profile. This framework was used to demonstrate that the large variability in the bias of LWP retrievals was associated with varying vertical profiles of CDNC and droplet size distribution dispersion (both of which are assumed to be constant in the standard adiabatic profile).

A primary objective of this study was to identify the cloud vertical profile assumption most appropriate for LWP retrievals; however, we have found that simply asking which retrieval assumptions perform better is not a particularly fruitful approach to these issues. In fact, there is likely no such thing as an ideal retrieval assumption that suits all cloud regimes. With that in mind, the impact of the *a priori* cloud vertical profile assumption should not be neglected when attempting passive LWP retrievals. Future work needs to address a method of identifying appropriate *a priori* vertical profile assumptions by constraining them relative to other measurable or retrievable cloud properties.

The focus on high-resolution retrievals based on 1-D radiative transfer leaves questions for future studies. While these model choices were invoked to focus on biases associated with cloud vertical profile assumptions, it does limit the scope of this study. Future work will need to also identify the relative importance cloud vertical profile and cloud horizontal heterogeneity or 3-D radiative effects on retrievals. This study begins the discussion of a broader and more complicated study of the impact of cloud vertical profile on LWP retrievals when including all possible cloud retrieval biases.

The results of this study are not limited to the passive bispectral retrieval of LWP. Regardless of the microphysical retrieval technique, the profile assumption bias has an impact on any passive shortwave retrieval based on the retrieval relationship in Equation 3.1. As we have demonstrated, polarimetric retrievals of droplet microphysics do not avoid this limitation. In fact, polarimetric retrievals exhibit a more acute sensitivity to the cloud top transition zone than bispectral retrievals. This is due, in part, to the influence of the bispectral v_e assumption on the variability of r_e retrievals. The r_e retrieval variability induced by this assumption is of the same magnitude as the impact of the transition zone. Future polarimetric microphysical retrievals, unencumbered by the v_e assumption will likely be sensitive to the cloud top transition zone, and this could in turn influence the future climatic record of LWP measurements.

Chapter 4: Comparisons of bispectral and polarimetric cloud microphysical retrievals using an LES-Satellite retrieval simulator

Many passive remote sensing techniques have been developed to retrieve cloud microphysical properties from satellite-based sensors, with the most common approaches being the bispectral and polarimetric techniques. These two vastly different retrieval techniques have been implemented for a variety of polar-orbiting and geostationary satellite platforms, providing global climatological datasets. Prior instrument comparison studies have shown that there are systematic differences between the droplet size retrieval products (effective radius) of bispectral (e.g. MODIS, Moderate Resolution Imaging Spectroradiometer) and polarimetric (e.g. POLDER, Polarization and Directionality of Earths Reflectances) instruments. However, intercomparisons of airborne bispectral and polarimetric instruments have yielded results that do not appear to be systematically biased relative to one another. Diagnosing this discrepancy is complicated, because it is often difficult for instrument intercomparison studies to isolate differences between retrieval technique sensitivities and specific instrumental differences such as calibration, atmospheric correction, etc. In addition to these technical differences the polarimetric retrieval is also sensitive

to the dispersion of the droplet size distribution (effective variance), which could influence the interpretation of the droplet size retrieval. To avoid these instrument-dependent complications, this study makes use of a cloud remote sensing retrieval simulator. Created by coupling a large eddy simulation (LES) cloud model with radiative transfer models, the simulator serves as a test bed for understanding differences between bispectral and polarimetric retrievals. With the help of this simulator we can not only compare the two techniques to one another (retrieval intercomparison), but also validate retrievals directly against the LES cloud properties. Using the satellite retrieval simulator we are able to verify that at high spatial resolution (50 m) the bispectral and polarimetric retrievals are indeed highly correlated with one another. The small differences at high spatial resolution can be attributed to different sensitivity limitations of the two retrievals. In contrast, a systematic difference between the two retrievals emerges at coarser resolution. This bias largely stems from differences related to sensitivity of the two retrievals to unresolved inhomogeneities in effective variance and optical thickness. The influence of coarse angular resolution is found to increase uncertainty in the polarimetric retrieval, but generally maintains a constant mean value.

4.1 Overview

The bi-spectral and polarimetric remote sensing techniques are the major tools we have to obtain DSD observations on a global scale. Thus it is important to identify and explain the differences between them so we can better understand the

advantages and limitations of each technique. A satellite retrieval intercomparison of POLDER and MODIS r_e retrievals by *Bréon and Doutriaux-Boucher* [2005] represented one of the first attempts to identify and understand the differences between the two techniques. The main finding from this study is that the bispectral-based MODIS retrieval of $r_e(2.13\,\mu\text{m})$ (using the $2.13\,\mu\text{m}$) SWIR band) is persistently larger than the polarimetric-based POLDER retrieval by about $2\,\mu\text{m}$ over ocean, despite a close correlation between the two. A variety of factors, from differences in sensitivity to cloud vertical profile to influence of cloud horizontal inhomogeneity, have been suggested to explain this difference. However, as pointed out by the authors, all these factors might contribute to the difference. It is difficult, if not impossible, to untangle them in observations and determine their relative importance. In addition, POLDER observations in this study were aggregated from the nominal 6 km spatial resolution to a much coarser 150 km resolution to achieve the angular resolution needed to resolve the cloud bow. The vast difference in spatial resolution (i.e., 150 km for POLDER and 1 km for MODIS) makes the interpretation of the $2\,\mu\text{m}$) r_e difference between the two retrievals even more difficult.

A more recent study by *Alexandrov et al.* [2015] is based on observations from the recent sub-orbital Polarimeter Definition Experiment (PODEX) in 2013. In this study, the polarimetric r_e retrievals for marine stratocumulus decks off the California coast from the RSP instrument are compared to collocated bi-spectral retrievals from the Autonomous Modular Sensor (AMS). Interestingly, the two retrievals are found to be in close agreement, with a correlation of 0.928 and negligible sub-micron bias. The differing conclusions of *Alexandrov et al.* [2015] and *Bréon and Doutriaux-*

Boucher [2005] raise many questions, motivating this study.

A great challenge facing these observational studies is the separation of various intertwined factors, which could result in retrieval differences. For example, the polarimetric and bi-spectral methods may have different sensitivity to cloud vertical structure, and at the same time they are also both affected by cloud horizontal inhomogeneity [*Zinner et al.*, 2010; *Zhang et al.*, 2012; *Miller et al.*, 2016; *Zhang et al.*, 2016a]. It is difficult, if not impossible, to separate these two factors based on observations alone. This study approaches the intercomparison of bispectral and polarimetric retrievals from a different perspective; rather than use observational remote sensing data, synthetic retrievals are generated from large-eddy simulations (LES) of clouds. Modeling radiative transfer in an LES scene to obtain total and polarized reflectances opens up the possibility of using the LES to perform synthetic bispectral and polarimetric retrievals. This retrieval simulator framework has proven to be a useful tool in other cloud remote sensing studies [*Zhang et al.*, 2012; *Miller et al.*, 2016; *Zhang et al.*, 2016a]. Using this idealized simulation at high spatial resolution, we can attempt to parse the effects of unresolved sub-pixel inhomogeneity, spatial resolution, and angular sampling/resolution on the inter-comparison of polarimetric and bispectral retrievals. The use of a satellite retrieval simulator opens up two unique opportunities for developing and studying cloud microphysical retrievals: First, it provides the means to compare retrievals directly to LES cloud microphysics and thus test retrieval closure for each of these retrieval techniques. Second, it allows us to perform a retrieval technique intercomparison that is independent of instrument characteristics and other differences that often complicated

previous observational studies. This study focuses on three particular questions:

- How well do the bispectral and polarimetric retrievals perform in terms of retrieval closure (i.e., comparing retrievals to the physical LES properties)?
- How do the bispectral and polarimetric retrieval techniques compare to one another at high spatial resolution?
- How are the bispectral and polarimetric retrieval techniques sensitive to specific observational conditions (i.e., the influence of spatial and angular resolution)?

The rest of the chapter is organized as follows: section 4.2 provides a brief overview of different sensitivities of the bispectral and polarimetric retrievals. section 4.3 describes the LES-based satellite retrieval simulations used in this study; the comparisons between the two techniques based on the LES cases are presented in 4.4; followed by summary and discussion in section 4.5.

4.2 Background

Both bispectral and polarimetric techniques are susceptible to a variety of retrieval uncertainties. The main objective of this study is to understand how the retrieval uncertainties influence each technique and whether they can lead to deviation between the two techniques in terms of retrieval results. In this study, we focus on three major sources of retrieval uncertainty for both techniques:

1) Cloud vertical profile: In the operational retrievals, both bispectral and polari-

metric techniques assume vertically homogenous clouds. However, clouds in reality often have significant variability in vertical profile resulting from microphysical processes (e.g., adiabatic condensation growth of droplet; sedimentation and coalescence). This deviation from the assumed profile gives rise to many questions. For example, how do we interpret the r_e and v_e retrievals based on homogenous cloud assumption? To what extent does cloud vertical profile influence the bispectral and polarimetric techniques? Note that Platnick (2000) developed a method utilizing the so-called vertical weighting function to interpret the r_e retrieval from the bispectral method for clouds with vertically varying r_e profile. Recently, Alexandrov et al., (2015) modified this method slightly and applied it to interpret the r_e and v_e retrievals from the polarimetric technique. In subsection 4.4.1, we will apply the vertical weighting function method to both techniques on the basis of the LES cloud fields, to help us understand if cloud vertical structure could lead to significant differences between the two techniques.

2) Reduced sensitivity: It can be clearly seen from Figure 2.4 that when clouds are optically thin ($\tau_{\text{tot}} < 3$), the LUT for the bispectral retrieval becomes less orthogonal and the isolines of r_e become more condense. This reduction in sensitivity can lead to significant retrieval uncertainties in bispectral techniques for optically thin clouds ($\tau_{\text{tot}} < 3$). Similarly, the sensitivity of polarimetric technique to r_e and v_e is reduced when DSD becomes very broad (i.e., $v_e > 0.15$), in which case the supernumerary bow features are barely distinguishable (Figure 2.5(c)). In subsection 4.4.2, we will investigate the impacts of the reduction of sensitivity on retrieval consistency between the two techniques.

3) Sub-pixel inhomogeneity: The impact of spatial resolution and unresolved sub-pixel cloud inhomogeneity on bispectral retrievals has been well studied [*Zhang and Platnick*, 2011; *Zhang et al.*, 2012, 2016a]. An important conclusion from these studies is that the so-called plane-parallel homogenous bias (PPHB) can cause the bispectral technique to significantly overestimate r_e. In contrast, the sensitivity of the polarimetric retrieval to unresolved sub-pixel inhomogeneity and resolution has not been significantly studied. In subsection 4.4.3, we will compare the impacts of sub-pixel inhomogeneity on bispectral and polarimetric techniques, and investigate whether is can cause deviation between the two techniques.

4) Angular resolution and sampling for polarimetric technique: In addition to spatial resolution, angular resolution and sampling is also important for the polarimetric technique. A coarse angular resolution may not be able to resolve the feature of the supernumerary bows. Similarly, if the scattering angles corresponding to the supernumerary bows are not or only partly sampled, then the polarimetric technique may not have enough information content for retrieval. This issue will be discussed in subsection 4.4.4.

4.3 Model and Methodology

The satellite retrieval simulator implemented in this chapter obtains vector radiative transfer calculations using the polarized doubling-adding technique (PDA) to produce 1-D total and polarized reflectances at the horizontal resolution of the LES grid (described below) [De Haan and Bosma, 1987]. The radiative transfer model-

ing in this work is performed for numerous solar zenith angles (SZA = $[20, 40, 60]^\circ$), viewing zenith angles (VZA = $[70 : +70]^\circ$), and a constant relative azimuthal angle ($\Delta\phi = 30^\circ$). The VZA resolution results in a scattering angle (Θ) resolution on the order of 0.5°. Reflectances in spectral bands (based on MODIS spectral response functions) are centered on 0.865, 2.13, and 3.75 μm wavelengths. Total reflectances in all bands are used to produce bispectral retrievals, whereas polarized reflectances in the 0.865 μmband are used to produce polarimetric retrievals. Subsequently, the bispectral and polarimetric retrieval algorithms are performed on the simulated reflectances to obtain the r_e (and v_e) retrievals. Bispectral and polarimetric retrievals are performed over a sub-set of observation geometries, with bispectral retrievals performed for VZA = $[50, 40, 30, 20, 10, 0, 10]^\circ$ and all SZA. Meanwhile, the polarimetric retrievals are performed for a SZA = 20° and a range of VZA = $[0 : 27]^\circ$ that result in reflectances spanning scattering angles resolving the primary and supernumerary bow features (i.e., $\Theta = [135 : 160]^\circ$). Reflectances are also aggregated from the 50 m native LES resolution up to coarser 100, 200, 400, and 800 m horizontal resolutions to reflect the influence of different remote sensing footprint resolutions. The retrievals performed in this study are also performed at all of the various reflectance resolutions. The bispectral LUT implemented in this study spans microphysical properties $r_e = [2 : 30]\,\mu$m in steps of 0.5 μm and $v_e = [0.01 : 0.11]$ in steps of 0.01. The τ_{tot} retrieval in this study is anchored to the 0.865 μm band optical properties and spans $\tau_{\text{tot}} = [0.1 : 100]$ with 101 logarithmically spaced grid points. Including v_e variability in the bispectral LUT allows for the comparison of standard MODIS-like retrievals (the $v_e = 0.1$ LUT) to retrievals with other v_e assumptions. The bispectral

retrieval is then accomplished by performing a 2-D linear interpolation of the observed reflectances and inverting between the reflectance and retrieval space. For the polarimetric retrieval, the polarimetric phase function library spans $r_e = [2 : 40]\,\mu$m in steps of $0.25\,\mu$m and $v_e = [0.01 : 0.3]$ in steps of 0.01. The polarimetric retrieval implemented in this study is based on the approach of Alexandrov et al. (2012a), fitting the polarized phase functions in their eq. (3) to the modeled polarized reflectances of the LES scene. The optimal parametric fit in the $-P_{12}$ library is arrived at a solution arrived at by using the Levenberg-Marquardt nonlinear least squares algorithm. This optimally fitting phase function corresponds to the resulting $r_e(pol)$ and $v_e(pol)$ retrieval. As previously stated in subsection 2.3.2 the polarimetric retrieval of τ_{tot} is accomplished by using a constrained 1-D version of the bi-spectral LUT.

The LES cloud fields are used not only to drive the radiative transfer simulations, but also to help us interpret and understand the retrieval results. As mentioned in Section 2.2, it is not trivial how to interpret the r_e and v_e retrievals based on the homogeneous cloud assumption, when the cloud has significant vertical structure. To address this issue, for each LES column with detailed vertical profiles of DSD, we derive two reference variables r_e(2WT) and v_e(2WT) from the vertical integration of the DSD profile. The integration is weighted by a two-way transmittance (2WT) function to account for the penetration depth of the single-scattered radiation following the procedure in subsubsection 2.2.1.1. The r_e(2WT) and v_e(2WT) take into account the first-order sensitivity of the retrieval techniques to the vertical profile of clouds. Thus, they are directly comparable to the nu-

merically retrieved r_e and v_e from the simulated reflectance [*Platnick*, 2000; *Zhang et al.*, 2010; *Alexandrov et al.*, 2015; *Miller et al.*, 2016]. We note that the 2WT vertical weighting function provides a reasonable approximation when the signal is contributed mainly by single-scattering (i.e., 3.7 μm or polarimetric reflectances) but becomes less accurate when multiple scattering increases [*Platnick*, 2000]. In addition to r_e(2WT) and v_e(2WT), we also derive $\tau_{\text{tot,LES}}$ for each LES column simply by integrating the extinction coefficient from cloud bottom to cloud top. The r_e(2WT) and v_e(2WT) and $\tau_{\text{tot,LES}}$ are used as references in the closure study in Section 4.1 to understand the differences between the retrievals and the original LES fields. After obtaining the r_e(2WT) and v_e(2WT) and $\tau_{\text{tot,LES}}$ at the 50 m native LES resolution, they are aggregated to 100, 200, 400, and 800 m to help interpret the retrievals at these coarser resolutions. In this study, we simply aggregate r_e(2WT) and v_e(2WT) from the native LES resolution 50 m to obtain the values at desired resolution (e.g., 800 m).

The three LES cases introduced in section 2.4 are the focus of this study. The first (referred to as ATEX clean hereafter) and second (ATEX polluted) cases are based on an idealized case study from the Atlantic Trade Wind Experiment (ATEX), with different aerosol loadings [*Stevens et al.*, 2001]. The ATEX cases are representative of a trade wind cumulus regime in which scattered cumuli rise into a thin, broken stratocumulus layer. The third case (referred to as DYCOMS-II hereafter), originally presented in *Stevens et al.* [2005], is an idealized setup based on clouds observed during the second research flight (RF02) of the Second Dynamics and Chemistry of Marine Stratocumulus project (DYCOMS-II) [*Stevens et al.*, 2003].

This case is representative of nocturnal marine stratocumulus under a dry inversion. The DYCOMS-II case has a domain size of 6.4,x 6.4,x 1.5 km (128,x 128,x 96 grid points), while each of the ATEX simulations have a domain size of 7.2 x 7.2 x 3 km (144 x 144 x 200 grid points). The spatial resolution of these LES cases is fixed at 50 m, while the vertical resolution is defined based on a stretched vertical grid with a minimum spacing of 5 m near the surface and temperature inversion to better resolve small-scale turbulence. Further details of the model setup for the DYCOMS-II case are provided in *Ackerman et al.* [2009]. The ATEX cases are updated model runs with increased spatial resolution that are similar to the cases discussed in *Fridlind and Ackerman* [2011]. For each LES scene a snapshot of cloud microphysical and optical properties is saved every half hour after the first hour of each simulation, resulting in numerous cloud fields. A single time step of each of the cases was selected to be the focus of this retrieval study, each occurring $\approx$ 3 hours into the simulation.

The variability of cloud optical and microphysical properties in each of the LES cases is highlighted in Figure 4.1 and Table 4.1. Spatial inhomogeneity of both optical and microphysical properties of these scenes is evident, with the ATEX polluted and DYCOMS-II cases exhibiting lower spatial inhomogeneity and the ATEX clean case being more broken and inhomogeneous. One method for quantifying the optical inhomogeneity of a cloud scene is to use the sub-pixel inhomogeneity index (Equation 2.49). In addition to optical inhomogeneity, each of the LES scenes also has characteristically different microphysical properties. The average value of r_e(2WT) of each scene varies, in part because of the initial background CCN in

LES case	CCN	CF	$\tau_{\mathrm{tot,LES}}$	r_e(2WT)	v_e(2WT))	H_σ(800 m))
DYCOMS-II	60	0.998	17.95	15.52	0.071	0.13
			(6.22)	(1.00)	(0.11)	(0.10)
ATEX Clean	40	0.941	7.90	16.93	0.16	0.42
			(8.02)	(2.62)	(0.12)	(0.17)
ATEX Polluted	600	0.985	17.48	7.29	0.13	0.24
			(14.71)	(0.91)	(0.068)	(0.13)

Table 4.1: Mean values (μ) and standard deviations (σ, in parenthesis) of various optical ($\tau_{\mathrm{tot,LES}}$ and H_σ) and microphysical properties (r_e(2WT) [μm], and v_e(2WT)) of the LES scenes examined in this study. The cloud fraction (CF) is obtained by using a threshold of $\tau_{\mathrm{tot,LES}} > 0.1$ to define cloudy pixels. Note that the units for cloud condensation nuclei (CCN) [#cm^{-3}]

each particular case but also cloud top height variability. In these LES cases v_e is spatially correlated with τ_{tot} and organized in a cellular structure - regions with larger τ_{tot} tend to have smaller v_e(2WT) and regions with thinner τ_{tot} tend to have large v_e(2WT).

4.4 Results and Analysis

4.4.1 Retrieval Closure

Before comparing the retrieval results from the two techniques, in this section we first carry out a retrieval closure study to assess and understand the differences between the retrieval results and the original LES cloud fields. This is a necessary sanity check that will help us understand the accuracy and uncertainty of our retrieval routines. More importantly, this closure study will help us to interpret the

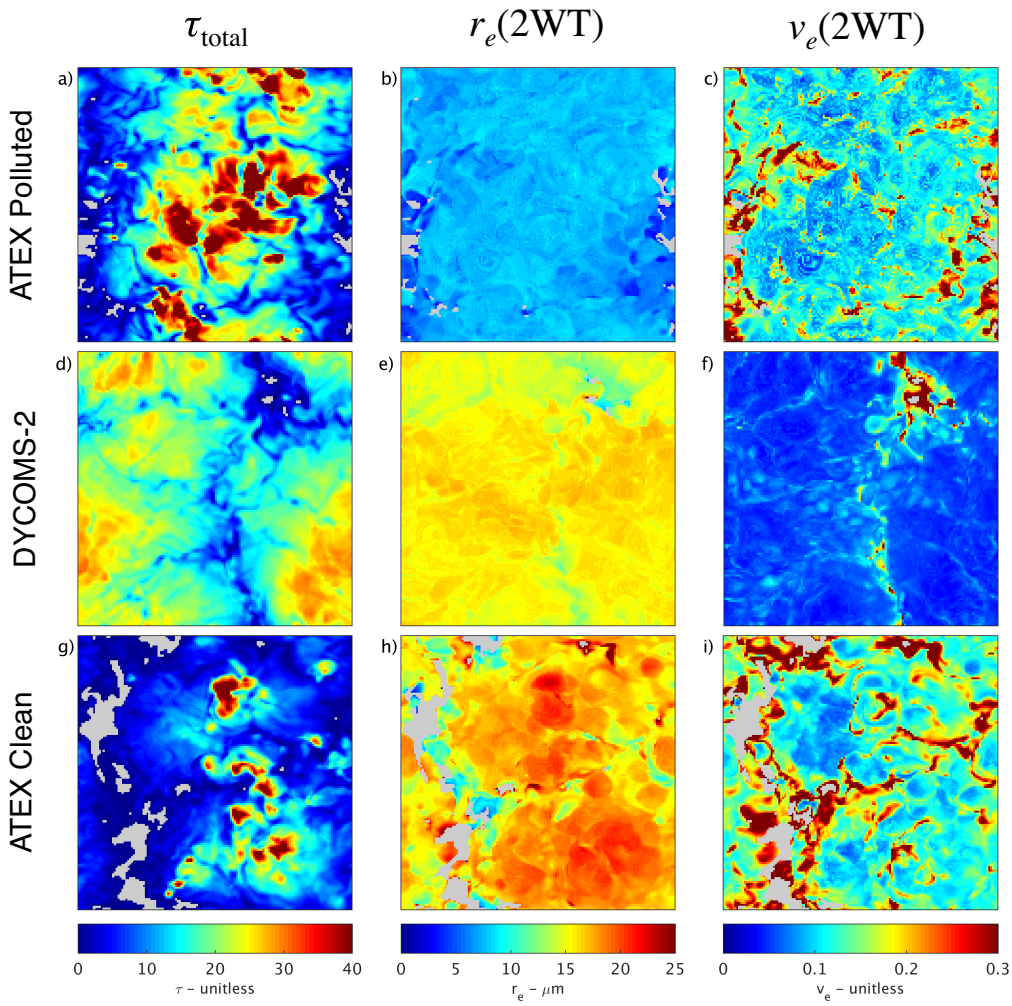

Figure 4.1: The optical and microphysical properties ($\tau_{\text{tot,LES}}$, r_e(2WT), and v_e(2WT)) of the LES cases examined in this study. The panels are arranged such that each LES case appears row-wise and the different properties are appear column-wise. Cloud-free masking in each of the images appears in gray.

retrievals based on homogeneous cloud assumption when the LES cloud fields have significantly inhomogeneous vertical profiles.

The bispectral retrieval closure comparisons in Figure 4.2 depict joint histograms of r_e and τ_{tot} retrievals using both the 2.13 and 3.75 μm SWIR bands against the reference values derived from the LES fields, r_e(2WT), v_e(2WT), and $\tau_{\text{tot,LES}}$. The two bispectral r_e retrievals, $r_e(2.13\,\mu\text{m})$ and $r_e(3.75\,\mu\text{m})$, are in agreement with the LES ground-truth (Figure 4.2(a,b)) with strong correlations exceeding 0.95. The biases between these two retrievals and the LES properties differ slightly. As expected, the different vertical weighting differences discussed in section 4.2, the $r_e(2.13\,\mu\text{m})$ retrieval is typically smaller than the $r_e(3.75\,\mu\text{m})$ retrieval. Both r_e retrievals have relatively small sub-micron mean biases compared to LES. The mean absolute biases in this closure experiment are also less than 1 μm. Note that the mean regression biases reported throughout this study are stated relative to the plotted axes as, $\mu_{\text{bias}} = \langle y - x \rangle$ and $\mu_{|\text{bias}|} = \langle |y - x| \rangle$ (i.e., x and y denote the axes). Additionally, it is important note a sampling limitations of this population, as none of the LES scenes in this study have a mean cloud top r_e near 10 μm. As a consequence, there is an evident lack of sampling in this particular regime. The two bispectral τ_{tot} retrievals, $\tau_{\text{tot}}(2.13\,\mu\text{m})$ and $\tau_{\text{tot}}(3.75\,\mu\text{m})$ in (Figure 4.2(c,d)), are compared here in terms of percent difference. Each of these τ_{tot} retrievals also reveal good correlations ($R > 0.99$), despite a slight high bias on the order of 2-5%. As explained earlier in section 4.2, the bi-spectral method suffer a reduction of sensitivity when clouds are optically thin. By sampling only LES columns that are optically thick ($\tau_{\text{tot}} > 3$) a significant improvement in the regression correlations of

the two r_e retrievals (Figure 4.2(e,f)) is achieved. However, some outlier points still remain. In particular, both $r_e(2.13\,\mu\text{m})$ and $r_e(3.75\,\mu\text{m})$ have some cases where the retrieved values (10-30 μm) are substantially larger than the corresponding r_e(2WT) values (mostly around 5μm)). The cause of these outliers and some other differences between the retrievals and LES fields will be discussed in detail in subsection 4.4.2.

The joint histograms in Figure 4.3 depict comparisons of the polarimetric retrievals, r_e(pol) v_e(pol), and τ_{tot}(pol), against corresponding LES properties. The r_e(pol) retrieval compares very well to r_e(2WT) (Figure 4.3(a)), with a regression correlation exceeding 0.98 and a mean bias of less than 0.1 μm. The quality of this retrieval closure test also supports the definition of r_e(2WT), as the polarimetric retrieval is indeed well represented by the single-scattering 2WT vertical weighting. In contrast, the polarimetric retrieval of v_e(pol) reveals a regression against v_e(2WT) (Figure 4.3(c)) that does not perform quite as well. In this case the regression correlation is much weaker (0.62) with a mean bias of -0.013. While the mean bias is on the order of the v_e LUT grid spacing, it is clear that the regression correlation is poor because of a systematic low bias for $v_e(2\text{WT}) > 0.15$.[1] Comparing only the population with $v_e(2\text{WT}) \leq 0.15$ reveals an improved correlation of 0.86 with negligible mean bias. The final retrieval product, τ_{tot}(pol) (Figure 4.3(e)), indicates that more accurate *a priori* r_e and v_e estimates have little impact on the retrieval of τ_{tot}. As explained earlier in section 4.2, the polarimetric method suffer a reduction of sensitivity when DSD is broad. This explains why limiting the

[1]The increased concentration of v_e(pol) retrievals at $v_e = 0.3$. is a result of the boundaries of the retrieval space, $v_e = [0.01, 0.3]$. This limitation is a consequence of the definition of the gamma distribution in *Hansen and Travis* [1974]; for $v_e = 0.3$ the size distribution becomes monotonic.

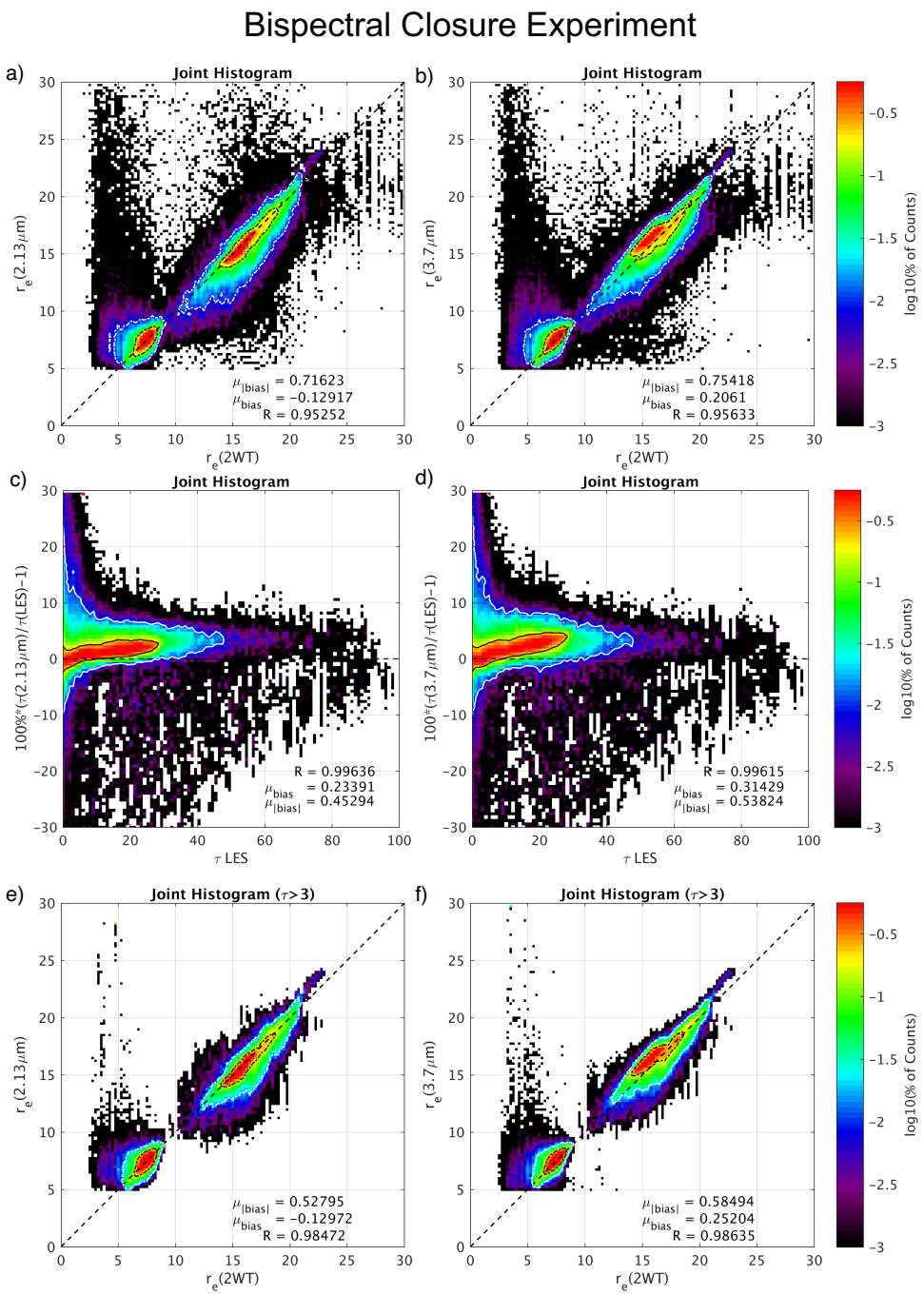

Figure 4.2: Joint histogram regressions or r_e and τ_{tot} in all LES cases comparing the bispectral retrievals to the physical LES properties. Panels (a) and (b) are regressions of the bispectral $r_e(2.13\,\mu\text{m})$ and $r_e(3.75\,\mu\text{m})$ retrievals against the physical analogue $r_e(2\text{WT})$. While panels (c) and (d) are regressions of the bispectral $\tau(2.13\,\mu\text{m})$ and $\tau(3.75\,\mu\text{m})$ retrievals against the physical $\tau_{\text{tot}}(\text{LES})$. While the final pair of panels, (e) and (f), display the regression of the bispectral $\tau_{\text{tot}}(2.13\,\mu\text{m})$ and $\tau_{\text{tot}}(3.75\,\mu\text{m})$ retrievals for only optically thick ($\tau_{\text{tot}} > 3$). Note that in each panel the quality of the correlation is quantified and the black and white population density iso-contours are drawn surrounding 66% and 95% of the data respectively.

regression population only to LES columns with $v_e(\text{2WT}) \leq 0.15$ (Figure 4.3(b)) increases the correlation and decreases the absolute bias. This appears to be an indication of sensitivity to degradation of the supernumerary bow features for large v_e, features that are necessary for reliable $r_e(\text{pol})$ and $v_e(\text{pol})$ retrievals. For $v_e(\text{pol})$ we find that by sampling LES columns that are optically thick ($\tau_{\text{tot}} > 3$), there is moderate improvement in the correlation and reduced biases (Figure 4.3(d). This improvement stems from the correlation between the population of optically thin clouds and high $v_e(\text{2WT})$ (Figure 4.3(f)) that are found near cloud edges in the LES scenes.

4.4.2 Retrieval Comparison at High Spatial Resolution

At the native spatial resolution of the LES (50 m) direct intercomparisons of polarimetric and bispectral retrieval techniques offer the possibility of diagnosing different sources of bias. The joint histograms of r_e retrievals in Figure 4.4 compare the two bispectral retrievals, $r_e(2.13\,\mu\text{m})$ and $r_e(3.75\,\mu\text{m})$, to the polarimetric retrieval, $r_e(\text{pol})$, for all LES cases and observation geometries. The regression for the comparisons of both $r_e(2.13\,\mu\text{m})$ (Figure 4.4(a)) and $r_e(3.75\,\mu\text{m})$ (Figure 4.4(b)) are highly correlated ($R \approx 0.954$) and have relatively small sub-micron mean biases. A couple of notable features are evident in these regressions. (1) The sign of the mean bias appears to be sensitive to the SWIR band selection. (2) There are numerous statistical outliers with small $r_e(\text{pol}) \approx 5-9\,\mu\text{m}$ but broadly distributed $r_e(2.13\,\mu\text{m})$ or $r_e(3.75\,\mu\text{m})$. One way to understand these features is to constrain the data set

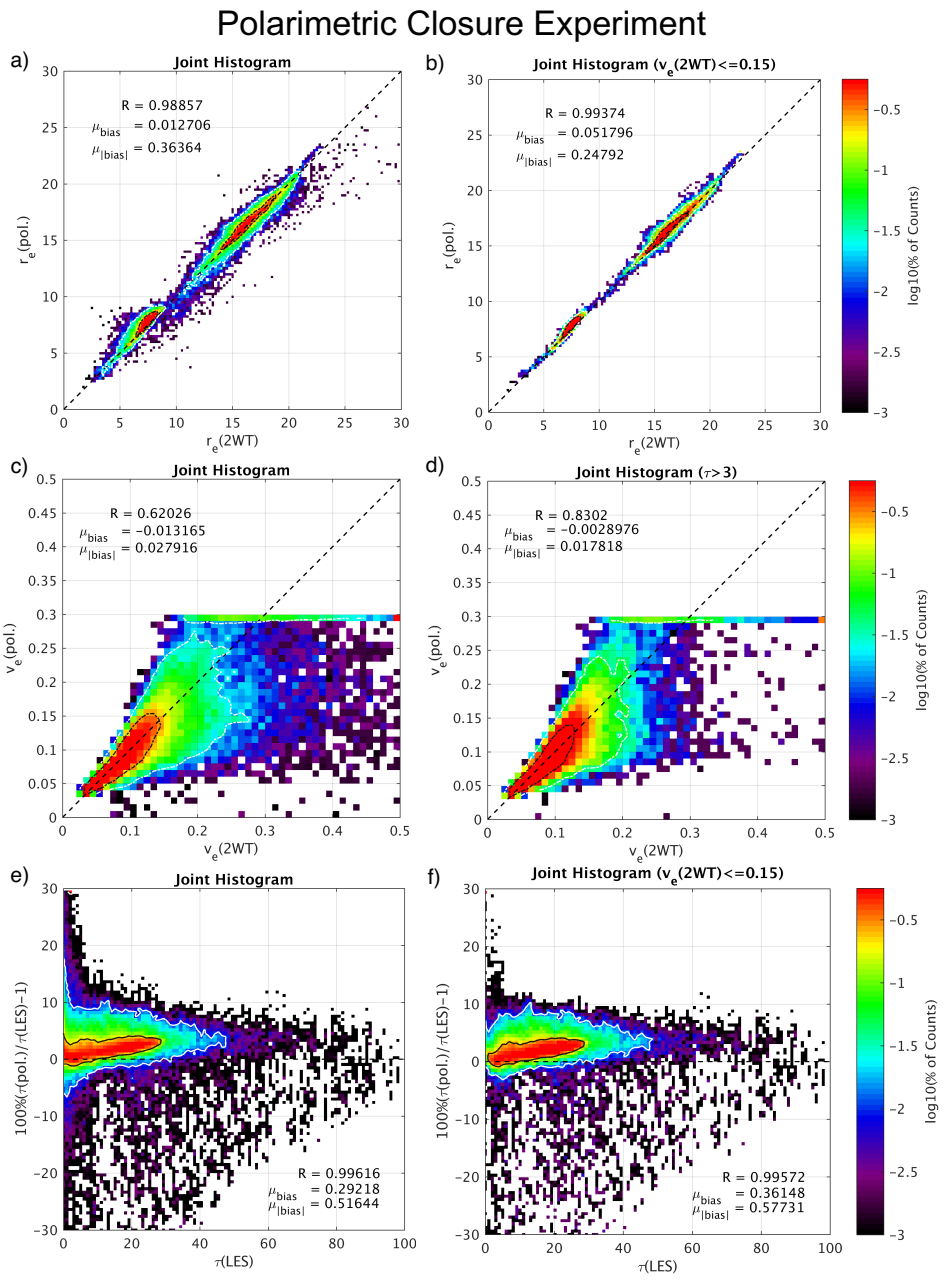

Figure 4.3: Joint histogram regressions of r_e, v_e, and τ_{tot} in all LES cases comparing the polarimetric retrievals to the physical LES properties. Panel (a) depicts the regression of the polarimetric $r_e(\text{pol})$ retrieval against the physical analogue $r_e(\text{2WT})$, while panel (b) is sub-selection of the same regression for low v_e. Panel (c) depicts the regression of the polarimetric $v_e(\text{pol})$ retrieval against the physical analogue $v_e(\text{2WT})$, while panel (c) is a sub-selection of the same regression for thick clouds ($\tau_{\text{tot}} > 3$). Panel (e) depicts the regression of the polarimetric $\tau_{\text{tot}}(\text{pol})$ retrieval against the physical analogue $\tau_{\text{tot}}(\text{LES})$, while panel (f) is sub-selection of the same regression for low v_e. Note that in each panel the quality of the correlation is quantified and the black and white population density iso-contours are drawn surrounding 66% and 95% of the data respectively.

to LES columns where both retrieval techniques yield reliable results. As discussed previously, the bispectral retrieval is sensitive to biases for thin clouds ($\tau_{\text{tot}} < 3$) and the polarimetric retrieval is sensitive to biases for broad droplet size distributions ($v_e > 0.15$). Based on these criteria ($\tau_{\text{tot}} > 3$ and $v_e \leq 0.15$), the constrained joint histograms (Figure 4.4(c) and (d)) feature much tighter regression relationships ($R \approx 0.99$) and reduced mean absolute biases are observed. These filters indicate that the poorly correlated population corresponds to situations in which both retrievals are expected to suffer from significant biases. The retrieval regression can be further improved if the bispectral retrieval is artificially provided with more complete information about the shape of the droplet size distribution. Providing the v_e(pol) retrieval as an a priori assumption for the bispectral LUT can demonstrate the sensitivity of the bispectral r_e retrievals to the $v_e = 0.1$ assumption. To create these new retrieval results we coupled the selection of the bispectral retrieval LUT to the pixel-by-pixel value, thus making sure that the respective LUT had a matching v_e to the v_e(pol) retrieval. The new $r_e(2.13\,\mu\text{m})$ retrievals (Figure 4.4(e)) are largely unchanged from the $v_e = 0.1$ results, although a slight increase in the two biases indicates that $v_e = 0.1$ was both an appropriate and sufficient assumption for the $r_e(2.13\,\mu\text{m})$ retrieval. In contrast, the $r_e(3.75\,\mu\text{m})$ retrieval (Figure 4.4(f)) is shown to benefit from this additional a priori information, improving the correlation and reducing the small systematic low bias ($\approx 0.25\,\mu\text{m}$). The differences between the two SWIR band retrievals can be explained in two ways. Firstly, the vertically weighted DSD of the $2.13\,\mu\text{m}$ SWIR band might result in a broader DSD (i.e., a larger v_e) compared to the $3.75\,\mu\text{m}$ SWIR band, and therefore the results might be closer to

the ones with the $v_e = 0.1$ assumption. Alternatively, the $R(2.13\,\mu\text{m})$ reflectance might simply be less sensitive to the broader DSD shape than the $R(3.75\,\mu\text{m})$ reflectance. Overall, these results demonstrate a feature well known to the remote sensing community; the bispectral retrieval of r_e is not particularly sensitive to v_e [*Nakajima and King*, 1990]. Indeed, when comparing the coupled bispectral retrieval of r_e to the polarimetric retrieval of r_e confirms that the advantage of retrieving v_e only changes the bispectral retrieval of r_e on sub-micron scales (i.e., it is appropriate to neglect this parameter of the DSD for retrieval purposes). The slight improvement demonstrates that when the two retrievals are compared on equal information footing they can be nearly equivalent.

The origin of the broadly distributed high-biased bispectral retrievals in the small droplet size regime ($r_e(pol) \approx 5\,\mu\text{m}$) stems from the ATEX polluted case, where such small droplets make up about 5% of the LES scene.[2] A close examination of this case reveals that there are no bispectral retrievals below $5\,\mu\text{m}$, despite approximately 5% of the cloudy pixels in the scene are characterized by $r_e(2\text{WT}) < 5\,\mu\text{m}$. This feature is a consequence of the bispectral LUT state space[3], which covers a r_e range of 5–30 μm. In contrast, the polarimetric retrieval space covers 1–30 μm. The differences between these two state spaces is not so much a matter of decision-making, but is more reflective of complexities of the bispectral retrieval for small r_e. To demonstrate this point panels (a) and (b) of 4.5 depict the cloud reflectances from the ATEX polluted case (colors) within the respective bispectral LUT. It is obvious

[2] Additionally, $\approx 2.5\%$ of the cloudy pixels in this scene exhibit values below $4\,\mu\text{m}$.

[3] Note that the MODIS LUT extends its range down to $4\,\mu\text{m}$, and in situations with multiple solutions the larger retrieval value is selected.

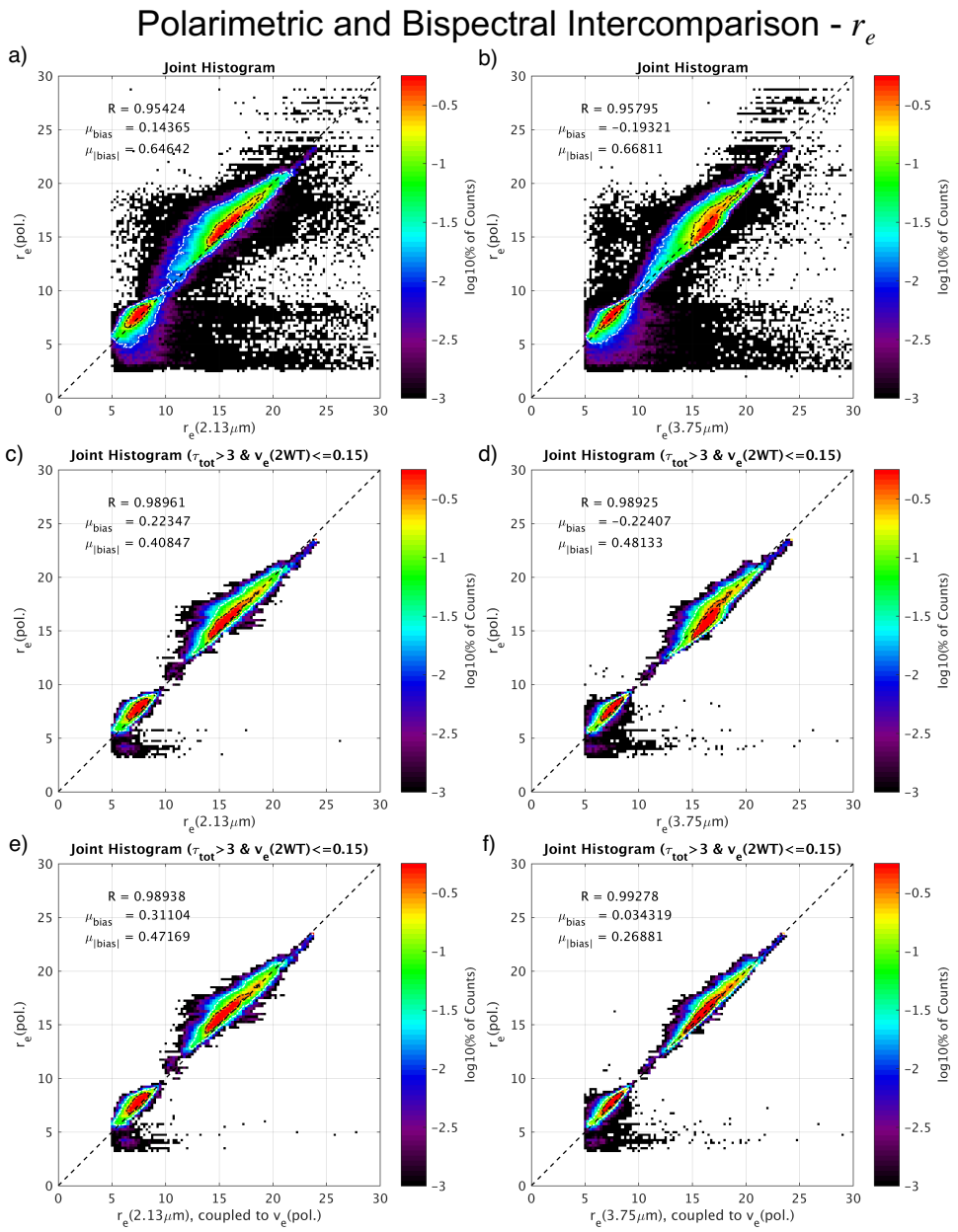

Figure 4.4: Joint histogram regressions of r_e retrievals for all LES cases comparing the bispectral and polarimetric techniques. Panels (a) and (b) display the unfiltered regressions of r_e(pol) against the $r_e(2.13\,\mu\text{m})$ and $r_e(3.75\,\mu\text{m})$ bispectral retrievals. After introducing filters to these regressions to remove thin clouds ($\tau_{\text{tot}} < 3$) and broad droplet size distributions ($v_e > 0.15$) panels (c) and (d) the retrieval intercomparison improves. Panels (e) and (f) each replicate the results from the previous selection criteria but additionally provide bispectral retrieval in this regression with v_e(pol) as an *a priori* for each retrieval. In each panel the quality of the correlation is quantified and the black and white population density iso-contours are drawn surrounding 66% and 95% of the data respectively.

that the black isolines for τ_{tot} and r_e increasingly overlap with the standard LUT space as τ_{tot} decreases. In this region of the state space, there are multiple solutions for a single reflectance pair; one solution is representative of a small r_e ($< 5\,\mu$m, extended LUT), while the other indicates a much larger r_e ($\geq 5\,\mu$m, standard LUT). There is also a modest impact on τ_{tot}, but due to the curvature of the LUT this impact is less severe. The overlapping region between the standard and extended LUT is referred to as the multiple solution space and the amount of LUT overlap is determined by both the observation geometry and the combination of the selected spectral bands. Depending on the optical thickness, the larger r_e retrieval may be significantly larger, because the extended LUT isolines cross numerous larger r_e isolines in the standard LUT. The color of each scattered reflectance in Figure 4.5(a) and (b) correspond with the associated $r_e(\text{SWIR}) - r_e(\text{2WT})$ retrieval bias maps shown in Figure 4.5(c) and (d). This highlights that for optically thick clouds the bispectral r_e retrievals exhibit only moderate retrieval biases on the order of $\pm 1\,\mu$m. However, for very thin clouds (near cloud edge) the retrieval bias can increase significantly. For some of these thinner clouds the retrievals also fall within the multiple solution space, so it is possible to attribute the very large biases to the presence of ambiguous retrieval results. This also provides another explanation for why the removal of optically thin ($\tau_{\text{tot}} < 3$) observations significantly improved the bispectral retrieval comparisons.

In contrast to the intercomparison of r_e retrievals, the τ_{tot} retrieval intercomparison in Figure 4.6 reveals very few differences between the bispectral and polarimetric technique. This is not surprising, because the $\tau_{\text{tot}}(\text{pol})$ retrieval is simply

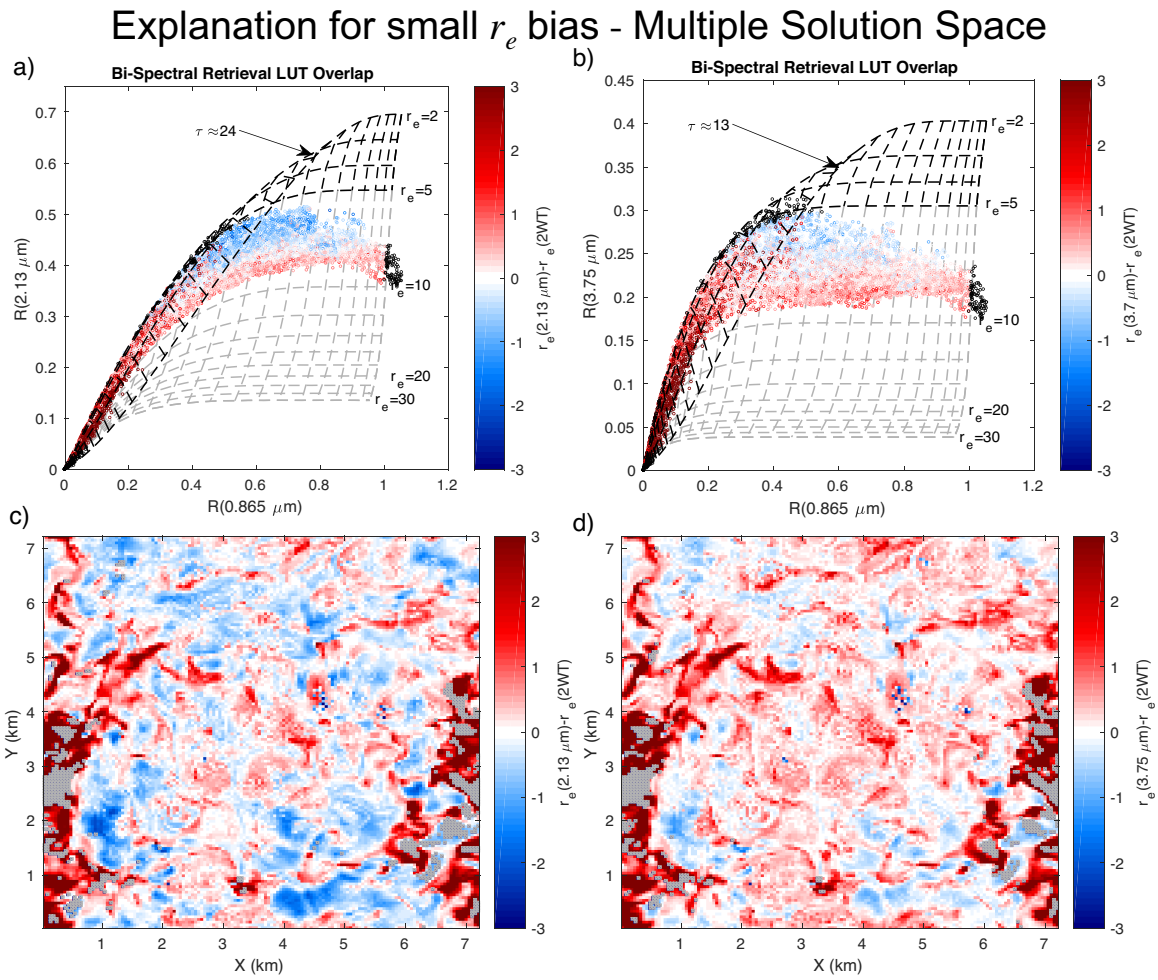

Figure 4.5: Panel (a) and (b) depict the standard bispectral LUT (light gray dashed lines) for both SWIR bands with the scattered reflectance points for the ATEX polluted LES case plotted overtop. The scatterplot is colored by the bias between the bispectral retrieval and the physical reference (r_e(SWIR)r_e(2WT)), which is also shown below as a spatial variability map. Note that some reflectance points are colored in black to indicate retrieval failure due to falling outside the standard LUT space. In addition to the standard LUT, an extended LUT including droplet sizes from 2–4 μm is included (black dashed lines), revealing an overlapping region of the two LUT for smaller τ_{tot} referred to as the multiple solution space.

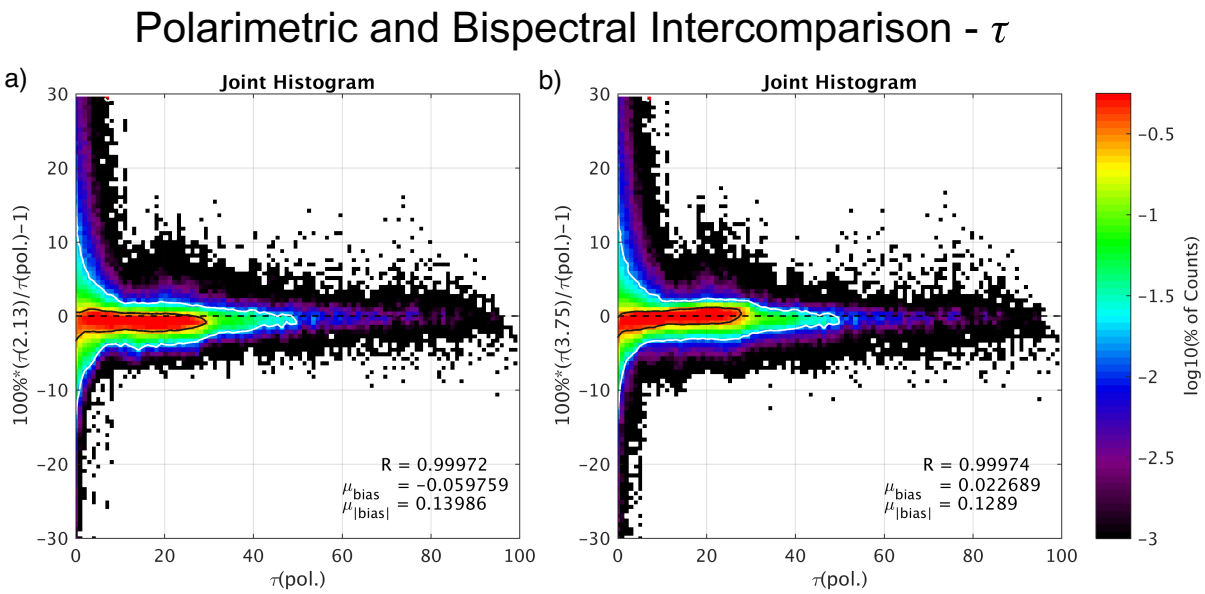

Figure 4.6: Joint histogram regressions of τ_{tot} retrievals for all LES cases comparing the bispectral and polarimetric techniques. Panel (a) and (b) display the $\tau_{\text{tot}}(2.13\,\mu\text{m})$ and $\tau_{\text{tot}}(3.75\,\mu\text{m})$ retrievals respectively. In each panel the quality of the correlation is quantified and the black and white population density iso-contours are drawn surrounding 66% and 95% of the data respectively.

a reimplementation of the bispectral technique with constraints on r_e and v_e (as discussed in section 4.2).

4.4.3 Sensitivity to Unresolved Spatial Inhomogeneity

Unresolved spatial inhomogeneity affects the bispectral and polarimetric cloud retrievals in very different ways. Comparing 100% overcast coarse resolution retrievals to the native resolution (50 m) results demonstrates this difference clearly, as illustrated in the panel (a) and (b) of Figure 4.7. As the retrieval resolution coarsens (larger circles), the sub-pixel inhomogeneity index (H_σ) tends to increase (redder color), and the $r_e(2.13\,\mu\text{m})$ retrieval suffers from an increasingly high bias relative to the polarimetric retrieval. Compared to the $r_e(2.13\,\mu\text{m})$ retrieval the bias

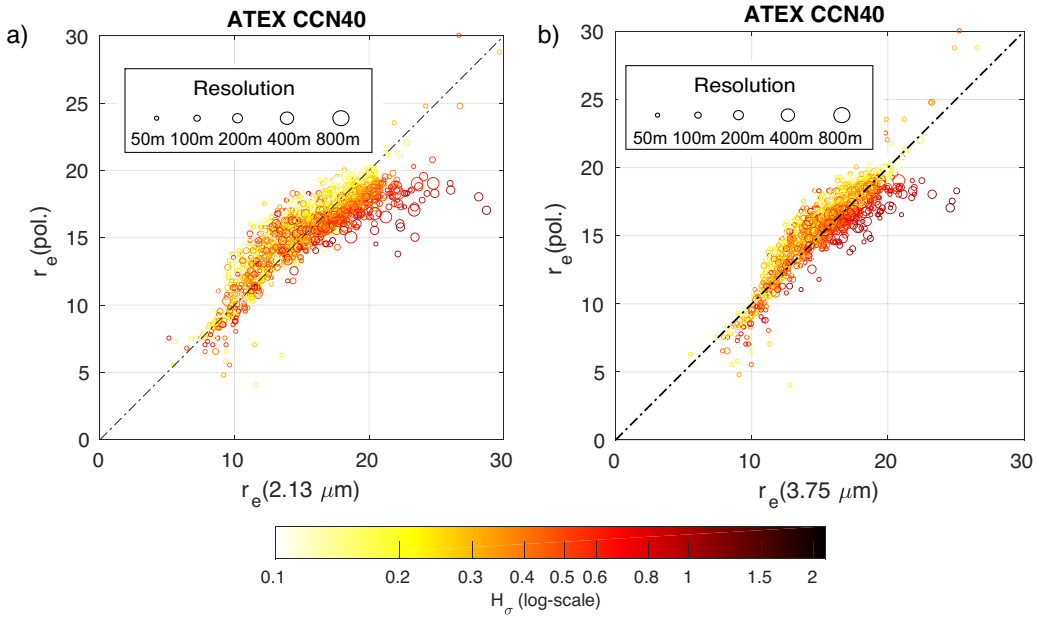

Figure 4.7: Bispectral and polarimetric cloud retrievals exhibit different sensitivities to sub-pixel inhomogeneity even for 100% cloudy pixels. Panel (a) and (b) each respectively demonstrate that the $r_e(2.13\,\mu\text{m})$ and $r_e(3.75\,\mu\text{m})$ retrievals diverge from the polarimetric retrieval at coarse resolutions (size of circle) and with large sub-pixel inhomogeneity, H_σ (color).

in the $r_e(3.75\,\mu\text{m})$ results is lower, although the trend is still clearly present.

To probe how unresolved inhomogeneity influences these two retrieval techniques, we will examine a particularly inhomogeneous pixel from the ATEX clean case at a very coarse resolution ($800\,m$). Focusing first on the bispectral retrieval using the $2.13\,\mu$m SWIR band, the LUT scatterplot in Figure 4.8(a) reveals that there is significant variability in the sub-pixel (i.e., 50 m) VNIR reflectances, indicated by a large value of the sub-pixel inhomogeneity index ($H_\sigma = 0.5637$). In contrast to the variability of VNIR reflectances, the microphysical properties of this $800\,m$ pixel are largely homogeneous, indicated by the narrow distribution of sub-pixel $r_e(\text{2WT})_{50\,\text{m}}$ (color of the points). The sub-pixel mean of $< r_e(\text{2WT}) >_{50\,\text{m}} = 19.23\,\mu$m agrees well with the mean of both sub-pixel retrievals, $< r_e(2.13\,\mu\text{m}) >_{50\,\text{m}} = 18.73\,\mu$m and

$< r_e(\text{pol}) >_{50\,\text{m}} = 18.92\,\mu\text{m}$. This combination of optical inhomogeneity and microphysical homogeneity leads to an average reflectance (indicated by the black star) for the 800 m pixel that falls significantly below the $r_e = 20\,\mu\text{m}$ isoline (i.e., the closest isoline to the mean sub-pixel retrievals). Thus, the coarse resolution 800 m reflectance results in an 800 m bispectral retrieval with $r_e(2.13\,\mu\text{m})_{800\,\text{m}} = 23.62\,\mu\text{m}$, which is biased high by $\approx 4\,\mu\text{m}$. This effect is attributable to the well-documented PPH bias induced by the curvature of the bispectral LUT [*Zhang et al.*, 2016b, 2012, 2016a]. The PPH bias has a stronger influence on the $2.13\,\mu\text{m}$ retrieval compared to the $3.75\,\mu\text{m}$ retrieval (Figure 4.8(c)) because the curvature of the LUT is more pronounced.

The polarimetric retrieval has a fundamentally different relationship to the unresolved sub-pixel inhomogeneity, as shown in the sub-pixel polarized reflectance histogram in Figure 4.8(b). The reflectances in this figure have been binned by scattering angle to demonstrate the 50 m sub-pixel distribution of polarized reflectances within the selected 800 m pixel footprint. Within the plot there are also two curves, shifted in amplitude away from the histogram for clarity, that display the mean 800 m multi-angular polarized reflectance and the corresponding 800 m retrieved polarized phase function. It is evident from this histogram and these curves that the mean angular position of the supernumerary bow does not shift, indicating that there is no significant difference between $r_e(\text{pol})_{800\,\text{m}}$, $\langle r_e(\text{pol})_{50\,\text{m}} \rangle$, and $\langle r_e(\text{2WT})_{50\,\text{m}} \rangle$. In contrast, there is clear variability in the amplitude of sub-pixel polarized reflectances. This variability owes itself to both optical (τ_{tot}), and microphysical inhomogeneity (i.e., $v_e(\text{2WT}) > 0.15$) within the coarse resolution pixel. For thin clouds ($\tau_{\text{tot}} < 3$)

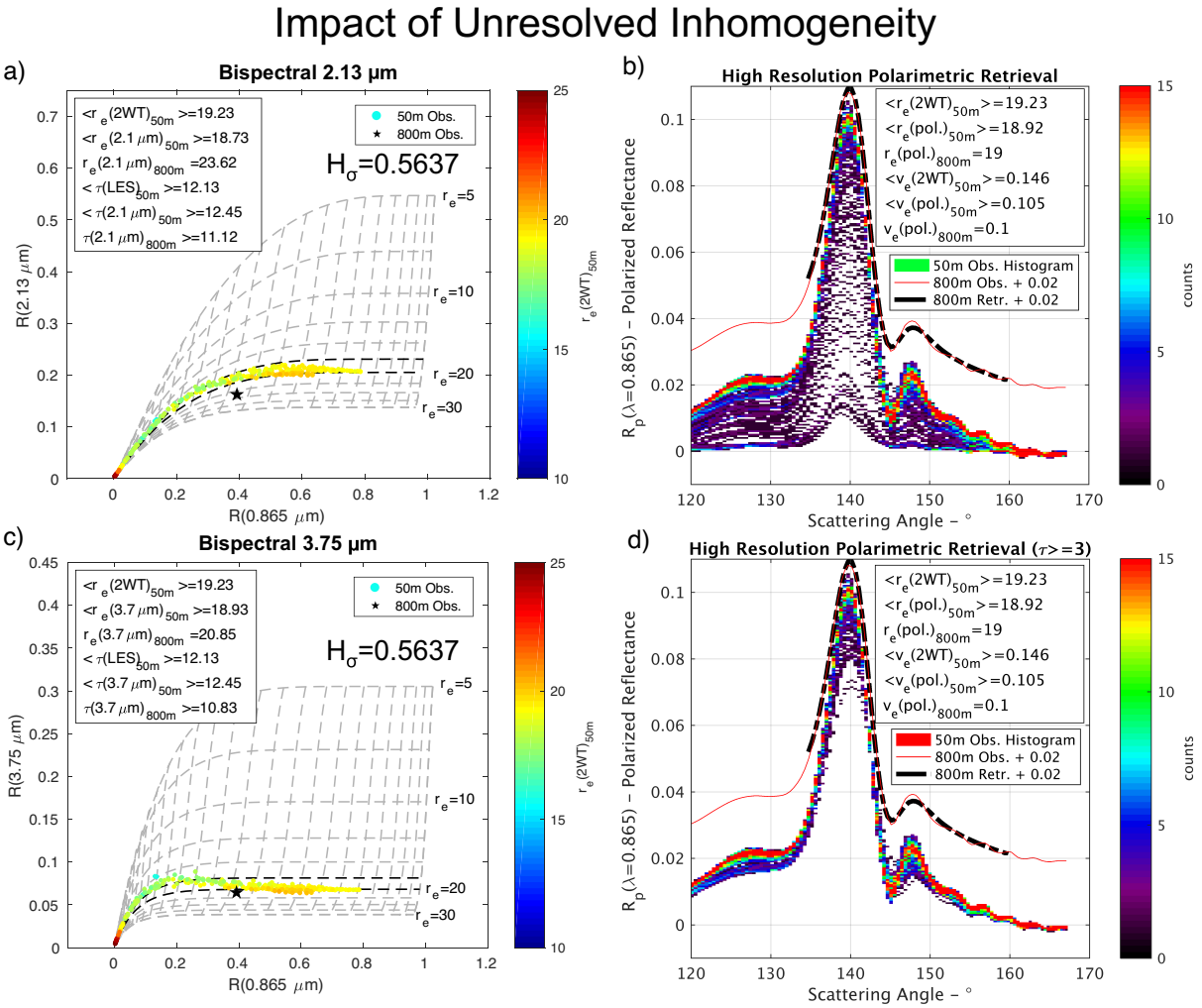

Figure 4.8: Selecting a particularly inhomogeneous 800 m pixel how resolution and inhomogeneity influence the bispectral and polarimetric retrieval in different ways. Panels (a) and (c) depict the bispectral LUTs and 50 m reflectances for the 2.13 and 3.75 μm SWIR retrievals respectively. The scattered points correspond to 50 m reflectances with color corresponding to r_e(2WT), while the black star corresponds to the 800 m reflectance pair (the average of the 50 m data). The polarimetric reflectance distribution histograms in panels (b) and (d) address how the high-resolution (50 m) reflectance distribution influences the polarimetric retrieval at coarse resolution (50 m). The two curves (plotted with a 0.02 reflectance shift for clarity) are the 800 m observed reflectance (black dashed curve) and the 800 m retrieval (red solid curve). All of these figures include statistics on the high-resolution averages of physical properties and retrievals along with their coarse resolution counterparts for comparison.

the supernumerary bow amplitude is dependent on both τ_{tot} and v_e. With a fixed v_e and varying τ_{tot} the polarized reflectance converges towards an asymptotic maximum for optically thick clouds ($\tau_{\text{tot}} \geq 3$), a consequence of increasing depolarization due to multiple scattering. Similarly, for a fixed τ_{tot}, reflectances corresponding to $v_e(\text{2WT}) > 0.15$ also produce decreased polarization in the primary and supernumerary bow features, as discussed in subsection 2.3.2. Despite the fact that both types of inhomogeneity induce an asymmetric polarized reflectance distribution, we find that these features do not systematically bias the $v_e(\text{pol})$ retrieval in this case. In fact, rather surprisingly, we find that the most important bias for the coarse spatial resolution $v_e(\text{pol})$ retrieval is the lack of sensitivity on $v_e(\text{2WT}) > 0.15$, a feature that was also present for the high spatial resolution retrievals. This finding is also supported for polarimetric retrievals performed on sub-populations of the polarized reflectance of this 800 m pixel that removed populations of either the $v_e(\text{2WT}) > 0.15$ or $\tau_{\text{tot}} < 3$ populations, removing either of them had little to no impact on either the coarse resolution $r_e(\text{pol})$ or $v_e(\text{pol})$ retrieval. Possible explanations for this behavior will be discussed in section 4.4.

4.4.4 Sensitivity to Angular Resolution and Sampling

The polarimetric retrieval requires high-resolution multi-angular data to resolve the supernumerary bow features. To test how angular resolution influences polarimetric retrievals we examined coarse spatial resolution $r_e(\text{pol})_{800\,\text{m}}$ retrievals at different angular resolutions. Each angular resolution (i.e., changing angular step

size) was also convoluted with shifting angular sampling (i.e., changing the initial angle). This convolution is necessary in order to account for all possible sets of scattering angle observations associated with each resolution. These coarse resolution retrievals were then compared to the original high angular resolution retrieval. The results of this experiment (including all LES cases), are shown in Figure 4.9(a), reveal that angular resolution does not systematically bias r_e(pol) retrievals, although angular resolutions exceeding 3° do result in a marked increase in retrieval variability (i.e., a constant mean bias, but increased absolute bias). In contrast, Figure 4.9(b) demonstrates that angular resolutions exceeding 3° lead to both high-biased v_e(pol) and increased retrieval variability.

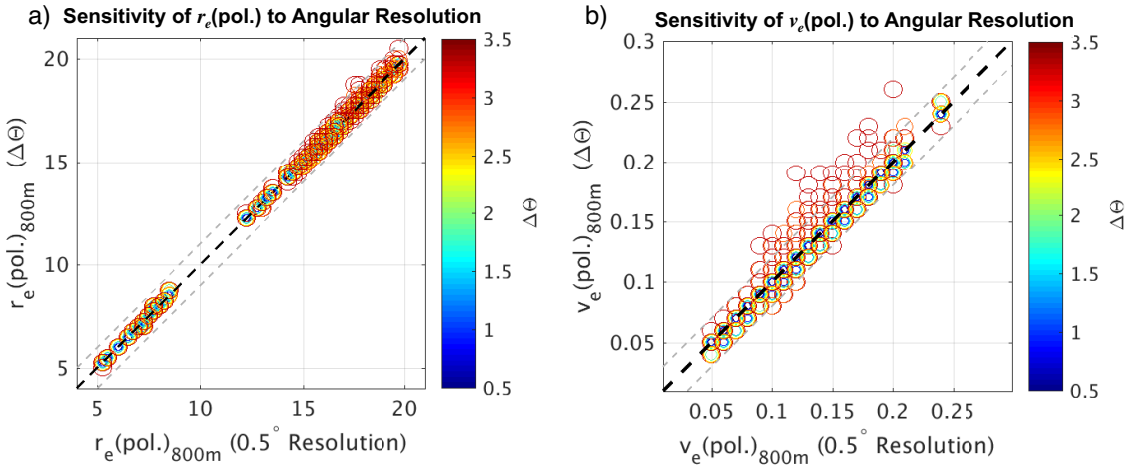

Figure 4.9: Angular resolution sensitivity experiments examining polarimetric retrievals of r_e (panel a) and v_e (panel b) for all LES scenes at the 800 m spatial resolution. The color and size of scattered points denote the angular resolution of each retrieval. The gray dashed lines denote a step in microphysical space of the ±0.5 m and ±0.01 for r_e and v_e respectively.

The origin of the observed degradation in retrieval accuracy above 3° angular resolution is demonstrated in Figure 4.10(a), where two different polarized phase functions with $r_e = 15\,\mu$m and $v_e = [0.03, 0.2]$ (solid and dashed-dotted respec-

tively). are sampled at an angular resolution of 3.5° (indicated by the gray vertical lines). This resolution is coarser than the spacing between the supernumerary bow maxima. As a consequence, this particular angular sampling nearly intersects both of the polarized phase functions at nearly the same locations. This leads to a relatively low cost-function during the best fit optimization in the polarimetric retrieval algorithm. The lack of observed differences between these two curves leads to a lack of v_e information. However, under different angular sampling condition, shifting the initial angle by a few degrees to the right, the supernumerary bow peaks of the low v_e curve would be sampled and the similarity between the observations of these two curves would go away. This highlights an important feature of multi-angular polarimetry, poor angular resolutions can suffer increased biases depending on whether or not important angles are sampled. Generalizing this result requires determining the angular spacing of the supernumerary bow features for other r_e. With decreasing droplet size the supernumerary bow features widen and dilate, making it easier to resolve supernumerary bow features at coarse angular resolution. The peak-to-trough distance of the supernumerary bow oscillations can be used to determine the Nyquist-frequency, or in this case Nyquist resolution. In signal analysis, a sampling resolution finer than the Nyquist frequency is required to appropriately resolve features of an oscillatory signal. The corresponding Nyquist angular resolution, that is required for resolving the supernumerary bow oscillations, changes with both r_e and λ according to the behavior illustrated in Figure 4.10(b). Note that according to this analysis a shorter wavelength would require finer angular resolutions. The Nyquist angular resolution for $= 0.865\,\mu$m and $r_e = 15\,\mu$m is 3°, providing an explanation

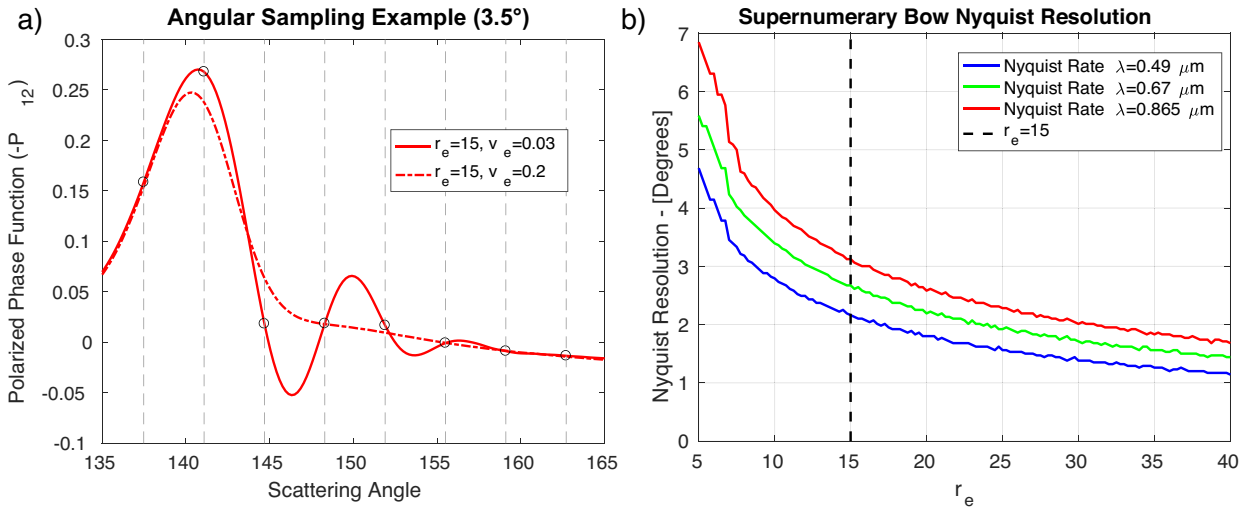

Figure 4.10: Panel (a) features the polarized phase functions $r_e = 15\,\mu$m (red) at $v_e = 0.03$ (solid) and $v_e = 0.2$ (dashed). Gray dashed lines and circles indicate a 3.4° observation sampling of the phase functions. The Nyquist rate is obtained by measuring the peak-to-trough distance of the supernumerary bow oscillations. The Nyquist resolution changes as a function of r_e and λ as shown in panel (b), where the gray vertical line highlights the Nyquist resolutions required for the $r_e = 15\,\mu$m case.

for the increased uncertainty in r_e(pol) and v_e(pol) LES retrievals exceeding this angular resolution.

4.5 Summary and Discussion

The analysis in this study, which features comparisons of vastly different passive cloud property retrieval techniques, is facilitated by comparisons to the LES cloud fields. Perhaps one of the most essential examples of this is the retrieval closure experiment at the native LES resolution (50 m). This experiment reveals promising results for both the bispectral and polarimetric retrievals. For the bispectral retrieval, the closure experiment shows significant biases for retrievals of very thin clouds, as well as only small differences between the vertically weighted cloud properties in each of the two SWIR bands (2.13 and 3.75 μm). Meanwhile, for the

polarimetric retrieval, the closure experiment demonstrates that the r_e(pol) retrieval agrees well with the vertically weighted in situ properties of each LES scene. However, the v_e(pol) retrieval exhibits persistent low biases due to a lack of retrieval sensitivity to very broad droplet size distributions (i.e., $v_e(\text{2WT}) \leq 0.15$). The optical thickness retrievals from both methods are effectively the same, with the caveat that the polarimetric technique performs the r_e(pol) retrieval as an a priori constraint on the τ_{tot} retrieval space. Regarding τ_{tot}, both bispectral and polarimetric retrievals were found to have a small systematic high bias on the order of 2–5%.

The retrieval intercomparison of polarimetric and bispectral retrievals in this study demonstrates that both techniques yield very similar results, especially when the most reliable populations of cloud properties are selected for each method ($\tau_{\text{tot}} > 3$ and v_e centered around 0.1). While the physical principles and measurement requirements are vastly different, both retrieval techniques seem to be able to capture similar information about r_e. These results agree with high-resolution airborne observations obtained during the PODEX and ORACLES field campaigns, where RSP and AMS microphysical retrievals are compared [*Alexandrov et al.*, 2015]. These high spatial resolution field campaign observations indicate that the two retrieval techniques agree well to within the tolerances observed in this study. The bispectral r_e retrievals are found to be moderately sensitive to v_e in the 3.75 μm band, and less so in the less absorptive 2.13 μm band. Coupling the retrieved v_e(pol) to the bispectral $r_e(3.75\,\mu\text{m})$ retrieval led to slight improvements in the r_e(pol) and r_e(2WT) comparison. It should be noted that for MODIS cloud products the bias due to the $v_e = 0.1$ assumption does not substantially impact the r_e retrieval com-

pared to other sources of bias (i.e., cloud inhomogeneity or 3-D radiative effects). In addition, the MODIS Collection 6 cloud product includes uncertainty estimates associated with the v_e assumption. The intercomparison of the bispectral and polarimetric τ_{tot} retrievals indicates that the two produce very similar results. This was to be expected, as the polarimetric technique also uses a bispectral LUT approach to derive τ_{tot}. When the results from the two methods diverge, the observations tend to be related to the thin cloud regimes.

The presence of a multiple solution space in the bispectral LUTs, where small droplet sizes ($r_e < 5\,\mu$m) have the same reflectance as larger droplets, was shown to induce numerous outliers resulting in a significant high bias in the bispectral retrievals for both r_e and (to a lesser extent) τ_{tot}. This multiple solution space likewise impacts the MODIS operational products, since the bispectral LUTs used in the MODIS collection 6 cloud products include theoretical r_e solutions as low as $4\,\mu$m. However, for retrievals with multiple LUT solutions the MODIS product only reports the larger r_e value, leading to a systematic bias if the observed cloud really includes a population of small droplets. As a consequence, for thin clouds with small droplet sizes one can expect the comparison of polarimetric and bispectral retrievals to disagree. This strong high-bias for small r_e retrievals provides a plausible explanation for the large discrepancies observed in the small droplet size regime in the intercomparison of MODIS and POLDER retrievals [*Bréon and Doutriaux-Boucher*, 2005]. Absent a solution to this issue, future intercomparisons or combined climatological datasets should be limited to retrievals of r_e(pol) exceeding 5–7 μm (depending on the respective bispectral LUT multiple solution space properties).

At the coarse spatial resolutions of most satellite instruments, the dominant source of bias between the polarimetric and bispectral r_e retrievals is attributable to the influence of unresolved spatial inhomogeneity. In this study we found that even for 100% cloudy pixels (at a coarse $800\,m$ horizontal resolution) the influence of the PPH bias is significant, with the average r_e bias exceeding $1\,\mu$m in the most inhomogeneous LES scene (ATEX clean). Based on these results we expect that the overall systematic bias observed in the MODIS and POLDER intercomparison of moderate droplet size regimes may be attributable to the influence of this PPH bias [*Bréon and Doutriaux-Boucher*, 2005]. Recently, great effort has been made to account for the influence of the PPH bias on bispectral (MODIS) retrievals. The 2-D Taylor expansion technique implemented by *Zhang et al.* [2016a] offers the possibility of quantifying (and potentially correcting for) the impact of PPH bias on bispectral retrievals. This approach requires high spatial resolution measurements in at least one spectral band to obtain the sub-pixel reflectance variability, which is used to determine corrections for the bias of r_e and τ_{tot}.

Sufficient angular resolution is one of the more important requirements of the polarimetric retrieval technique. We find that resolving the multi-angular polarized reflectance at a resolution coarser than the Nyquist angular resolution results in greater uncertainty (r_e(pol) and v_e(pol)) and biased (v_e(pol)) polarimetric retrievals. The required angular resolution is dependent both on droplet size and wavelength. Future cloud polarimetric instrumentation should consider these angular resolution requirements. While we have not explicitly tested the so-called super-pixel approach implemented for POLDER retrievals, our coarse spatial and

angular resolution studies lead us to anticipate some biases induced by this technique. We would expect such an approach to further bias r_e(pol) retrievals low, due to the lack of sensitivity to unresolved high-v_e populations. In addition, this current study indicates that r_e(pol) retrieval variance might increase, but the mean bias may not increase significantly. However, if the there was significant correlation between the unresolved r_e and v_e populations within the observation footprint, the mean r_e bias would be expected to suffer.

Chapter 5: The impact of 3-D radiative effects on passive cloud remote sensing – Comparisons of total and polarized reflectances and retrievals

Radiative transfer in 3-D inhomogeneous cloud fields has always proved to be a complicated issue for passive cloud remote sensing techniques that are typically restricted to 1-D cloud homogeneity assumptions. While a great amount of study has gone into understanding 3-D radiative effects on total reflectances and on subsequent bispectral retrievals, very few have examined the influence of 3-D radiative effects on polarized reflectances and retrievals. Addressing this lack of understanding, this study aims to contextualize 3-D radiative effects in polarized reflectances by comparing total and polarized reflectances (and retrievals) to one another. Building a foundation for understanding polarimetric 3-D radiative effects we focus on use simple hypothetical models to study the coupled impact that cloud horizontal inhomogeneity and 3-D radiative effects can have on remote sensing. With hypothetical models of clouds we can develop an understanding of 3-D radiative effects in total and polarized cloud retrievals from two perspectives: The first focuses on idealized cloud cases, isolating simplified examples of horizontal radiative flux; while the second examines more realistic inhomogeneous conditions by analyzing 3-D effects

observed in a bounded-cascade fractal cloud model. Comparisons between the 1-D and 3-D reflectances and retrievals are made in order to study horizontal photon transfer and radiative smoothing. The differences between the behavior of polarized and total reflectances are explored in particular, in addition to behavior of subsequent impacts on retrieval biases. The influence of 3-D radiative effects on polarized reflectances is currently an area of significant interest with regard to forthcoming satellite remote sensing technologies.

5.1 Overview

To facilitate passive remote sensing of cloud properties, it is typical to approximate the inhomogeneous 3-D structure of real clouds into a simplified 1-D model such that the radiative transfer process can be efficiently simulated. To that end, clouds are typically considered to be both vertically and horizontally homogeneous within each observation footprint. This assumption is known as the plane-parallel homogeneity (PPH) assumption. In addition, it is assumed that there is no net horizontal photon transport between individual pixels and, as such, each pixel is independent of one another. This is known as the independent pixel assumption (IPA). These assumptions can become problematic when the underlying cloud is particularly inhomogeneous. When real clouds deviate from the simplified plane-parallel IPA model, the cloud radiative properties (i.e., cloud reflectance) expected based on 1-D radiative transfer modeling will be different from the observed cloud radiative properties, which can in turn lead to retrieval artifacts. These deviations

of 1-D radiative transfer models from the real world 3-D cloud fields, and subsequent impacts on retrievals, are known as "3-D radiative effects" [*Davies*, 1978]. The importance of these 3-D radiative effects depend on numerous observation conditions including observation and solar geometry [*Davies*, 1978; *Loeb and Davies*, 1996], cloud inhomogeneity [*Zhang et al.*, 2012; *Marshak et al.*, 2006], and the spatial resolution of observations [*Cahalan et al.*, 1997; *Oreopoulos and Davies*, 1998].

Most previous studies of 3-D radiative effects have focused on cloud optical thickness retrievals [*Marshak et al.*, 1995; *Loeb and Davies*, 1996; *Várnai and Davies*, 1999; *Várnai and Marshak*, 2002a], only few have studied the impacts on cloud microphysics retrievals [*Marshak et al.*, 2006; *Zhang and Platnick*, 2011; *Zhang et al.*, 2012]. Motivated by this, this study primarily focuses on cloud microphysical properties (e.g., effective radius (r_e) and effective variance (v_e) of the droplet size distribution). In addition, we are focused on both the bispectral and polarimetric cloud retrievals. In contrast to the vast amount of work that has gone into understanding 3-D radiative effects observed in total reflectances [*Marshak and Davis*, 2005; *Davis and Marshak*, 2010], there has been very little exploration of 3-D radiative effects in polarized reflectances. The physical processes behind polarized radiative transfer differ in a few significant ways from total reflectance. For example, polarized reflectances are predominately the result of single scattering and only a few orders of multiple-scattering events contribute to the observed polarized reflectance. The work of *Cornet et al.* [2009] demonstrated that this low-scattering order dependence led to 3-D radiative effects in cirrus that exceeded the 1-D reflectances by $\approx 8\%$ over all viewing angles. They also demonstrated for a step cloud case that the lo-

cal influence of 3-D radiative effect near cloud edge can be quite significant, with biases ranging from 25–150% depending on cloud thickness and viewing geometry. The angular dependence of the polarized reflectance is required for the polarimetric r_e(pol) and v_e(pol) retrievals. Therefore the angular dependence of polarized 3-D radiative effects could be of great importance to the accuracy of the polarimetric technique. The polarimetric retrieval sensitivity study of of *Alexandrov et al.* [2012a] found that the r_e(pol) retrieval was not significantly influenced by the 3-D radiative effects. However they also found that the v_e(pol) retrieval high-biased in retrievals based 3-D reflectances. However, the focus of that work was on the quality of retrieval outcomes, not on the influence of 3-D effects, so their work did not focus on the origins and impact of polarimetric 3-D effects much further.

This study explores the impact of 3-D radiative effects on total and polarized reflectances and their subsequent impact on cloud property retrievals. Simulated cloud reflectances in both 1-D (independent pixel) and 3-D scenes will be obtained using the recently developed polarized Monte Carlo radiative transfer algorithm, Multiple-Scaling-based Cloudy Atmospheric Radiative Transfer (MSCART) [*Wang et al.*, 2017]. The hypothetical cloud model clouds studied here will be used to develop the scientific knowledge required to study 3-D radiative effects in observed total and polarized cloud reflectances. Additionally, the comparison of 3-D effects in both bispectral and polarimetric retrievals will help to develop a greater understanding of the differences between observations made by different satellite instruments. This research will study the influence of 3-D radiative effects as follows: 1) hypothetical cloud scenes of increasing complexity will be generated in subsection 5.3.1.

2) The 1-D and 3-D reflectances of the hypothetical cloud models will be used to demonstrate illuminating and shadowing effects, the angular variability of 3-D reflectances, and diagnose radiative smoothing (subsection 5.4.1 and subsection 5.4.3). 3) Finally the 1-D and 3-D reflectances can be used to generate bispectral and polarimetric cloud retrievals that can be compared to one another and understood in context with the 3-D effects diagnosed in the previous step.

5.2 Background

One of the limitations of operational cloud retrieval algorithms is that 3-D radiative transfer effects are simply not accounted for in most algorithms [*Várnai and Davies*, 1999; *Marshak et al.*, 2006]. There are two primary categories of 3-D radiative effects: unresolved and resolved. As mentioned previously, operational retrievals are forced to assume that clouds are horizontally homogeneous below the resolved pixel scale. Below pixel resolution, unresolved cloud features can result in retrievals that suffer from PPH biases as discussed in subsection 4.4.3. On the other hand, the second category consists of horizontal inhomogeneities above detector resolvable scales. In this category pixels in an inhomogeneous cloud field can be influenced by 3-D scattering to/from neighboring pixels, violating the independent pixel approximation (IPA). As a consequence, there is a trade off, high resolutions are susceptible to the IPA biases associated with 3-D radiative effects, whereas low resolution reflectances that do not clearly resolve the cloud scale are susceptible to PPH biases [*Davis et al.*, 1997a]. The focus of this study is on resolved 3-D radiative

effects.

Transmission from or scattering into/out of neighboring pixels can lead to the so called illuminating/shadowing effect [*Marshak et al.*, 2006]. These effects are expressed in terms of the difference between 3-D and 1-D reflectances, where a positive value of $I_{3D} - I_{1D}$ corresponds to illuminating and a negative value with shadowing. Such 3-D radiative effects are not only important for inhomogeneous or broken clouds, but are also particularly relevant at cloud edges and during low solar illumination. Focusing on the bispectral retrieval, *Marshak et al.* [2006] demonstrated that, due to the non-linear relationship between reflectances and optical properties, the illuminating and shadowing effects lead to microphysical retrieval biases. For example, the shadowing effect increases r_e more than the illumination does. In contrast the illumination effect increases $\tau_{\rm tot}$ more than the shadowing effect does. The result is that for domain averages the values of r_e or $\tau_{\rm tot}$ will be biased low/high for illuminated pixels,

$$\Delta r_e^{\rm ill} \quad < \quad \Delta r_e^{\rm shd}\,, \tag{5.1}$$

$$\Delta \tau_{\rm tot}^{\rm ill} \quad > \quad \Delta \tau_{\rm tot}^{\rm shd}\,. \tag{5.2}$$

For high sun, the domain averaged 3-D reflectance is lower than predicted by 1-D RT (due to radiative smoothing) and thus shadowing dominates [*Davis and Marshak*, 2001]; while the opposite is true for low sun conditions [*Várnai and Marshak*, 2001]. It follows that for high sun the shadowing effect dominates, positively biasing bispectral r_e retrievals (on average). In contrast, for low sun, the illumination effect

dominates leading to a positive bias in retrieved optical thickness (on average).

Multiple scattering plays an important role in enhancing 3-D radiative effects, because of this it is important to understand the influence of multiple scattering on polarized reflectances. Typically, polarized reflectances are dominated by single-scattering. This is a result of the orientation of the scattering plane of each multiply-scattered photon becoming uncorrelated with one another, resulting in unpolarized light. However, for photons initially scattered in the near-forward direction the orientation of the scattering plane is largely preserved, and therefore secondary scattering events can continue to contribute to the magnitude of the polarized reflectance. Throughout this work we will refer to this type of scattering as polarimetrically coherent scattering[1]. For example, the primary and supernumerary cloudbows are influenced significantly by multiple scattering, while other scattering angles with lower polarized reflectances, are less sensitive to multiple scattering. This is a consequence of enhanced coherent scattering in directions associated with the primary and supernumerary bows. Forward scattered photons, with a preserved scattering plane and therefore polarization state, are capable of traveling from one pixel to another leading to an enhancement of the polarized reflectance these in these special angles.

[1]Not to be confused with coherent (or elastic) scattering, which preserves the energy and momentum of the scattered photon.

5.3 Models and Methodology

5.3.1 Cloud Models

5.3.1.1 Step Cloud Model

The step cloud case is one of the simplest hypothetical cloud observation scenarios, featuring a homogeneous optically thin-cloud environment ($\tau_{\text{thn}} = 0.1$) surrounding a region with a homogeneous step-wise jump in cloud optical thickness ($\tau_{\text{thk}} = 10$). Given that both the thin and thick regions have the same geometrical thickness, $H = 1\,\text{km}$, the extinction cross sections are $\beta_{\text{thn}} = 0.1\,\text{km}^{-1}$ and $\beta_{\text{thk}} = 10\,\text{km}^{-1}$ respectively. In this model we can meaningfully address the impact of horizontal photon transfer on reflectances and retrievals. Additionally, we use this case to understand the differences between how single-scattering and multiple-scattering influence the observed 3-D radiance field. The simplicity of the step cloud case also offers the opportunity to obtain analytical solutions for the single-scattering 3-D cloud reflectance. Such an analytical model can be quite useful in explaining the 3-D polarized reflectances because they are so strongly dominated by single-scattering. Comparisons of these single scattering approximations to the modeled 3-D and 1-D reflectances will enable a more robust understanding of the horizontal photon transport. For a nadir viewing zenith angle ($\mu \equiv 1$), the theoretical single scattering reflectance, I_{SS} or $-Q_{\text{SS}}$, can be described as a piece-wise function of x, breaking the scene into different sections sensitive to horizontal transport near the locations of the illuminated (x_{ill}), and shadowed cloud edges (x_{shd}),

$$I_{\mathrm{SS}}(x,\mu=1,\mu_0) = A \begin{cases} \left[1-e^{-H\beta_{\mathrm{thn}}\left(\frac{1}{\mu_0}+\frac{1}{\mu}\right)}\right] & 0 < x \le x_{\mathrm{ill}}\,, \\ \left[1-e^{-z'\beta_{\mathrm{thk}}\left(\frac{1}{\mu_0}+\frac{1}{\mu}\right)}\right] + e^{-z'\left(\frac{\beta_{\mathrm{thk}}}{\mu_0}-\frac{\beta_{\mathrm{thn}}}{\mu_0}\right)}\left[e^{-z'\left(\frac{\beta_{\mathrm{thn}}}{\mu_0}+\frac{z'\beta_{\mathrm{thk}}}{\mu}\right)} - e^{-H\left(\frac{\beta_{\mathrm{thn}}}{\mu_0}+\frac{\beta_{\mathrm{thk}}}{\mu}\right)}\right] & x_{\mathrm{ill}} < x \le x_{\mathrm{ill}} + \Delta x_{\mathrm{3D}}\,, \\ \left[1-e^{-H\beta_{\mathrm{thk}}\left(\frac{1}{\mu_0}+\frac{1}{\mu}\right)}\right] & x_{\mathrm{ill}} + \Delta x_{\mathrm{3D}} < x \le x_{\mathrm{shd}}\,, \\ \left[1-e^{-z'\beta_{\mathrm{thn}}\left(\frac{1}{\mu_0}+\frac{1}{\mu}\right)}\right] + e^{-z'\left(\frac{\beta_{\mathrm{thn}}}{\mu_0}+\frac{\beta_{\mathrm{thk}}}{\mu_0}\right)}\left[e^{-z'\left(\frac{\beta_{\mathrm{thk}}}{\mu_0}+\frac{\beta_{\mathrm{thn}}}{\mu}\right)} - e^{-H\left(\frac{\beta_{\mathrm{thk}}}{\mu_0}+\frac{\beta_{\mathrm{thn}}}{\mu}\right)}\right] & x_{\mathrm{shd}} < x \le x_{\mathrm{shd}} + \Delta x_{\mathrm{3D}}\,, \\ \left[1-e^{-H\beta_{\mathrm{thn}}\left(\frac{1}{\mu_0}+\frac{1}{\mu}\right)}\right] & x_{\mathrm{shd}} + \Delta x_{\mathrm{3D}} < x \le 12\,. \end{cases} \tag{5.3}$$

Where the coefficients in this model are defined as:

$$A \equiv \frac{\omega F_0 P_{ij}}{4\pi}\left(\frac{1}{\mu_0}+\frac{1}{\mu}\right)^{-1}, \tag{5.4}$$

$$z'(x, x_{\mathrm{edge}}, \mu_0) \equiv \frac{x - x_{\mathrm{edge}}}{\tan\theta_0}\,, \tag{5.5}$$

$$\Delta x_{\mathrm{3D}} \equiv H\tan\theta_0\,. \tag{5.6}$$

Note that the coefficient A can be modified to calculate I_{SS} or Q_{SS} depending on whether the phase function or polarized phase function is substituted into P_{ij}. The variable z' depends on both x and μ_0, and is used to define the amount of radiation transmitted into or out of the cloud edges located at x_{edge}. Additionally, ΔX_{3D} defines the maximum distance away from the cloud edges that could be influenced by single scattering horizontal transport effects across the cloud step.

5.3.1.2 Fractal Cloud Model

The fractal cloud represents the next incremental step in our study toward modeling a more realistic cloud, mimicking both the LWP distribution and the spatial variability of an MBL cloud field. The spatial variability of clouds and rain is self-similar across vast spatial scales [*Lovejoy*, 1982]. This self-similarity, a property of fractals, allows us to model cloud spatial distributions using multi-fractals. Taking advantage of this, realistic cloud spatial variability can be modeled using the bounded-cascade fractal model described in *Cahalan et al.* [1994]. The fractal model produces a spatial distribution of cloud LWP that is characteristic of marine stratocumulus clouds. The recursive algorithm for generating this one dimensional (horizontal variability) fractal cloud is as follows: Starting with a single uniform cloud slab with fixed geometric thickness and mean LWP. This uniform slab is then divided in half horizontally, with each containing half of the cloud mass. Subsequently a fraction of mass, f_0, is transferred in a random direction (from the left to the right or vice versa) and into one of the new sub-divisions. With these two slabs the process begins again, but this time dividing both of the new slabs in half again. A random fractional mass transfer of, f_1, is then exchanged between the newly created quarters. The schematic diagram of this process from *Davis and Marshak* [2010] is included for the sake of completeness in Figure 5.1(a). This process then continues for many steps, for example, the fractal model in Figure 5.1(b) went through n=10 iterations of this algorithm. The recursive relationship defining the fractional mass transfer is defined in Equation 5.7, where f_0 is a free parameter

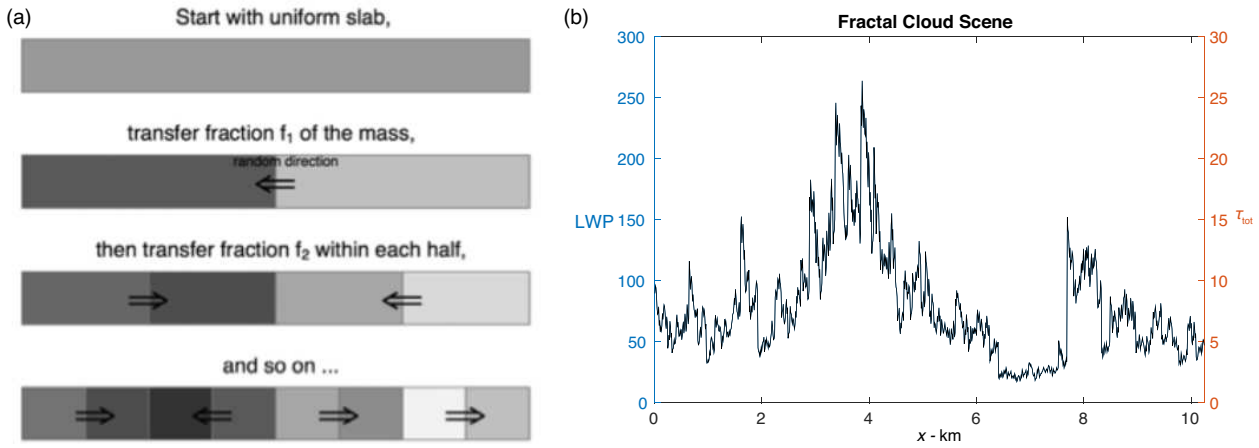

Figure 5.1: The schematic of the recursive algorithm used to generate the fractal cloud model is shown in panel (a). Darker shades of gray indicate higher LWP. Refer to the text for more details. (Schematic adapted from *Davis and Marshak* [2010]). The particular fractal cloud scene used throughout this study is shown in panel (b), with the left y-axis indicating the LWP and right y-axis indicating optical thickness.

that defines the resulting distribution of LWP. If we define $f_0 = 0.5$ then the fractal model reproduces a LWP distribution characteristic of a stratocumulus cloud.

$$f_n = f_0\, 2^{-n/3} \tag{5.7}$$

The fractal cloud LWP can then be used to determine τ_{tot} by assuming a vertical profile of $r_e(z)$ and using the relationship in Equation 3.1. In this study we will assume that the cloud is vertically homogeneous, using the LWP relationship in Equation 3.2. This assumption focuses our efforts on understanding 3-D radiative effects and spatial inhomogeneity. The fractal cloud scene, shown in Figure 5.1, displays LWP and τ_{tot} for a cloud with $r_e = 15\,\mu\text{m}$ and $v_e = 0.02$, a geometrical thickness $H = 1\,\text{km}$ and a spatial resolution of 10 m. Note that in some experiments we will make use of alternate fractal model that has the same LWP and optical

thicknesses but geometric thickness of $H = 500\,\mathrm{m}$ and a spatial resolution of $50\,\mathrm{m}$.

5.3.2 Radiative Transfer and Retrieval

The 1-D (independent pixel) and 3-D cloud radiative transfer simulations in this study are each handled by the same radiative transfer model to avoid discrepancy during intercomparison. To that end, we make use of the Monte Carlo radiative transfer algorithm Multiple-Scaling-based Cloudy Atmospheric Radiative Transfer (MSCART) [*Wang et al.*, 2017]. MSCART is a fast vector 3-D radiative transfer algorithm that yields both total and polarized reflectances for complex cloud structures. Note that the modeled 3-D reflectances used throughout this study have been collocated to the cloud top to correct for the impact of parallax on the 3-D radiation fields. This is an important detail, as an accurate comparison of 1-D and 3-D reflectances requires that both observations originate from the same location of the cloud. The bispectral and polarimetric retrievals are performed in the same manner as discussed previously in subsection 2.3.1 and subsection 2.3.2. Further details on other sources of bias between the bispectral and polarimetric retrievals can be found in chapter 4.

5.3.3 Quantifying Radiative Smoothing

A useful tool for understanding the influence of radiative smoothing is the spatial Fourier transform, F. The spatial Fourier transform can be used to determine the scale-dependent power spectral energy density, E , probing the behavior of

different scale-dependent cloud phenomenon,

$$E(k) = |F(k)|^2 \,, \tag{5.8}$$

where the power spectral density expresses the relative contribution of each spatial scale (k is the spatial wavenumber) to the spatial variability of the scene. In the fractal cloud case it will be useful to study the power spectral density (PSD) of the cloud LWP and reflectances, which often exhibit a power law sensitivity to spatial scale,

$$E(k) \approx k^{-\beta} \,, \tag{5.9}$$

where β is referred to as the spectral slope, defining the steepness of the energy cascade in the PSD. Cloud physical properties have a PSD that follows Kolmogorov's $\beta = 5/3$ law for energy distribution in a turbulent fluid [*Kolmogorov*, 1941]. In the absence of horizontal radiative flux, cloud reflectances also follow a $\beta = 5/3 \approx 1.66$ spectral slope over all scales. For example, the power spectrum of the fractal cloud LWP (in Figure 5.2) used in this study has a value of β that quite close to 5/3. The fractal model reproduces this spectral variability because of the $2^{-n/3}$ dependence in Equation 5.7, other power law dependencies would produce different spectral slopes. The value of β is determined by fitting a linear curve to the log-log plot of $E(k)$. Obtaining a good curve-fit is nontrivial, and requires aggregating some of the high spatial-frequency data to appropriately account for the limited amount

of low spatial frequency data [*Davis et al.*, 1997b]. This is accomplished by first creating octave bin averaged PSD's that are then used to obtain a best fit curve that defines β. The details of this bin-averaging approach are described in section 3 of *Schröder et al.* [2004] as well as appendix A of *Davis et al.* [1996]. With increasing horizontal photon transport, the cloud reflectances at small scales (typically $< 1\,\mathrm{km}$) the PSD will sometimes exhibit a steeper power law relationship with $\beta_s > \beta$ due to the erosion of small scale features caused by radiative smoothing. In constrast, the large scale cloud optical properties continue to follow the $\beta = 5/3$ relationship. The spatial scale where this change in the variability of cloud optical properties occurs is known as the scale break, ξ. The scale break is useful in determining the resolution below which 3-D radiative effects have significant influence over cloud reflectances [*Schutgens and Roebeling*, 2009]. The theoretical work in *Marshak et al.* [1995] led to the determination of a relationship between the transport mean free path ($l_\mathrm{t} = [(1-g)\sigma_\mathrm{ext}]^{-1}$) in fractal clouds and the expected ξ of reflectances from a conservative scattering medium,

$$\langle \xi \rangle \approx \sqrt{\langle l_\mathrm{t} \rangle \langle H \rangle} = \frac{\langle H \rangle}{(1-g)\langle \tau_\mathrm{tot} \rangle}\,. \tag{5.10}$$

For a moderately absorbing medium, this result was studied theoretically in *Marshak et al.* [1999] and numerically in chapter 12.4.2 of *Marshak and Davis* [2005]. These works demonstrated that increasing the absorption decreased the length scale of the scale break, due to the the role that absorption plays in decreasing multiple

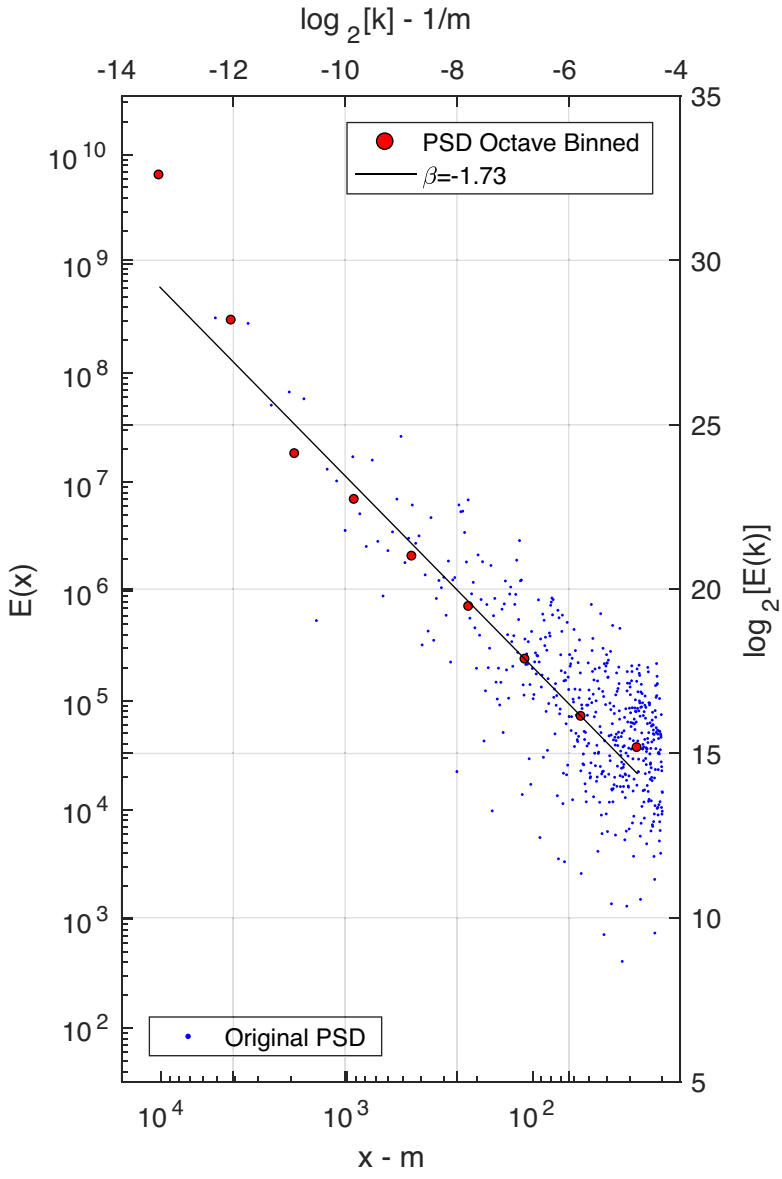

Figure 5.2: Power spectral density of the LWP in the fractal cloud model scene. The scattered blue points correspond to the original PSD. Whereas the red scattered points correspond to the octave-bin averaged PSD that is used to determine the linear best fit. Note that the theoretical spectral slope for MBL clouds and this fractal model is $\beta \approx 5/3$.

scattering (and therefore the transport mean free path).

$$\xi\left(\bar{\omega}\right) > \xi\left(\bar{\omega'}\right) \quad \text{, if } \ \bar{\omega} > \bar{\omega'}\,. \tag{5.11}$$

In addition to radiative smoothing, roughening of the scene properties can occur under certain observation conditions [*Marshak and Davis*, 2005]. For example, when the SZA is very large radiative roughing is observed at intermediate scales near the scale break. Additionally the intensity of radiative roughening is dependent on absorption, with smaller $\bar{\omega}$ corresponding to increased radiative roughening. Radiative roughening is characterized by a small ($\beta < 5/3$) or neutral ($\beta = 0$) the local slope in the PSD near the scale break. The behavior of radiative smoothing and roughening in the polarized and total reflectances will be explored throughout subsubsection 5.4.3.1.

5.4 Results and Analysis

5.4.1 Step Cloud Reflectances

The step cloud model serves as a simple demonstration of 3-D radiative effects related to horizontal photon transport and the violation of the IPA. At a spatial resolution of 10 m, the step cloud case has significant horizontal radiative flux – violating the IPA. Both the 1-D and 3-D reflectances of total and polarized light scattered from the step cloud model are depicted in Figure 5.3. These modeled reflectances are shown for SZA = $-60°$, VZA = $0°$, and RAA = $0°$, relative to the

scene this geometry places the sun to the left of the step. It should be noted that this nadir viewing geometry is convenient because it can be compared to the theoretical I_{SS} in Equation 5.3. One of the clearest features of the step cloud reflectance is the region on the sunward side of the step cloud that has a significantly brighter reflectance in the 3-D model due to illuminating effects. In this case, the light entering the τ_{thn} region ends up being transmitted into the τ_{thk} region, increasing the scattered light from the cloud step. This results in an increased photon flux across the cloud step that can then lead to multiply-scattered enhancements. For example photons that multiply scatter back out of the τ_{thk} region can illuminate the τ_{thn} region. Or multiple scattering can transmit these illuminating photons further into the τ_{thk} region, spatially broadening the peak of the illuminated reflectance. In addition to these illuminating effects, the side of the step cloud opposite the sun has a reduced 3-D reflectance associated with shadowing effects. In this case, the light entering the thick region of the cloud near cloud edge, has some of its photons absorbed or scattered away in the process of transmitting from the τ_{thk} and into the τ_{thn} region. This transmission loss on the shadowed side leads to a significantly reduced reflectance on the sunward cloud side. Both the illuminating and shadowing effects observed in the step cloud are largely a consequence of geometry, depending largely on the cloud geometrical thickness, the solar zenith angle, and the ratio of $\tau_{\mathrm{thn}}/\tau_{\mathrm{thk}}$. The illuminating and shadowing features are present in both total and polarized reflectances as well as all the spectral bands studied here – though the particular features of these effects may differ.

Focusing first on the bispectral total reflectances in Figure 5.3(a–b), the sig-

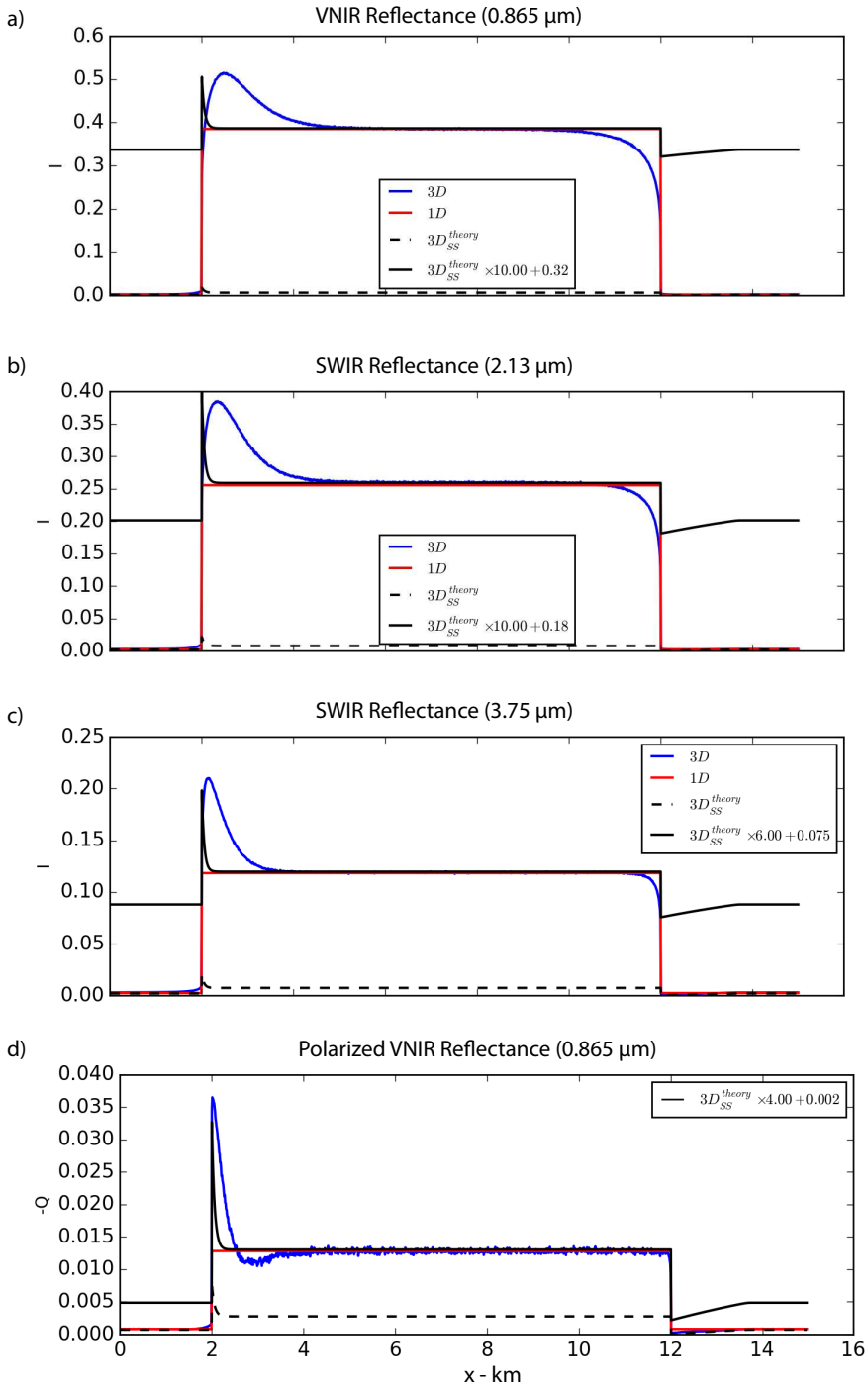

Figure 5.3: Step cloud total reflectances for $\lambda = 0.865$, 2.13, and 3.75 μm in panel (a), (b) and (c) respectively. All reflectances are observed at the following geometry: SZA = 60°, VZA = 0°, and RAA = 0°. In addition to the total reflectances, the polarized reflectance for $\lambda = 0.865\,\mu$m is in panel (d). Each panel includes 1-D (red) and 3-D (blue) reflectances as well as the theoretical I_{SS} (black) in Equation 5.3. Note that the I_{SS} has been adjusted and scaled to match the pattern of the modeled (multiple scattering).

nificant multiple scattering in the VNIR band (0.865 μm, Figure 5.3(a)) leads to a spatially broadened illuminating effect. As discussed previously, multiple-scattering can enhance 3-D radiative effects by increasing horizontal transfer into and out of the cloud step. In contrast, absorption reduces multiple scattering decreasing horizontal transfer. As a result, the absorbing SWIR bands (2.13 μm and 3.75 μm, Figure 5.3(b) and (c) respectively) exhibit illuminating shadowing effects that are sharper, and less spatially broadened. This dependence on the single scattering albedo indicates that strongly absorbing bands, or reflectances dominated by single scattering (i.e., polarized reflectance) will reduce the broadness of illuminating and shadowing effects. However, this does not mean that the influence of 3-D effects in these bands is lessened, because the relative bias between the peak illuminating reflectance and the 1-D reflectance increases with increased absorption. On the shadowed side of the step cloud the influence of absorption is again evident. Approaching the the transition from the thick to thin regions there is a dip in the reflectance – a consequence of horizontal flux due to transmission out of the thick cloud. The magnitude of this transmission effect is a function of absorption, because less light is transmitted in strongly absorbing spectral bands.

Compared to total reflectances, the 0.865 μm polarized reflectance in Figure 5.3(d) exhibits illuminating and shadowing effects that are similar, though sharper in magnitude and less broad in spatial extent. The relative magnitude of this peak is more than double the presumed 1-D polarized reflectance at cloud edge. At first glance, there is a lot of similarity between the polarized reflectance and the overall shape of the total reflectance in the strongly absorbing 3.75 μm band – supporting

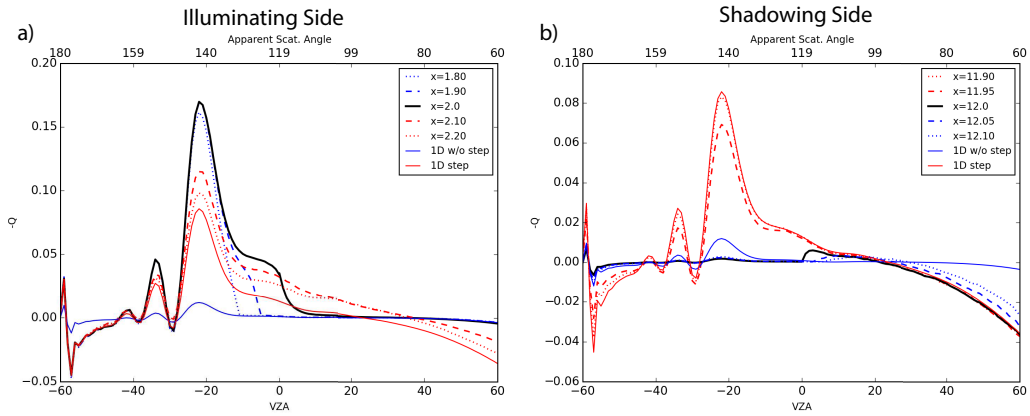

Figure 5.4: The angular features of the polarized reflectance are influenced 3-D effects near the illuminated side (panel (a)) and the shadowed side (panel (b)). Red curves correspond to reflectances within the thick cloud and blue curves correspond to reflectances that are within the thin cloud. The dashed curves are slightly displaced (50–100 m) to either side of the cloud edge (black curve). The solid red and solid blue lines correspond to the 1-D plane parallel reflectances.

the idea that strongly absorbing bands have single-scattering-dominated 3-D effects. Strictly speaking, the comparison between strongly absorbing total reflectance and polarized reflectances could be problematic. For one, coherent polarimetric scattering is unlike absorption, which absorbs photons irrespective of scattering geometry. In contrast, the dependence of the polarimetrically coherent reflectance on scattering angle leads to the multiple scattering sensitivity in polarized reflectances (as discussed in section 5.2). To that end, Figure 5.4 reveals that the influence of 3-D effects (illuminating and shadowing) on polarized reflectances is intrinsically dependent on viewing angle. This figure demonstrates clear enhancements to the polarized reflectance in primary, secondary, and supernumerary bow features on the illuminating side of the cloud. In contrast, the 3-D effects on the shadowed side are less stark and extensive, but there are some impacts within 50 m of cloud edge that influence the back-scattering more than the cloudbow features.

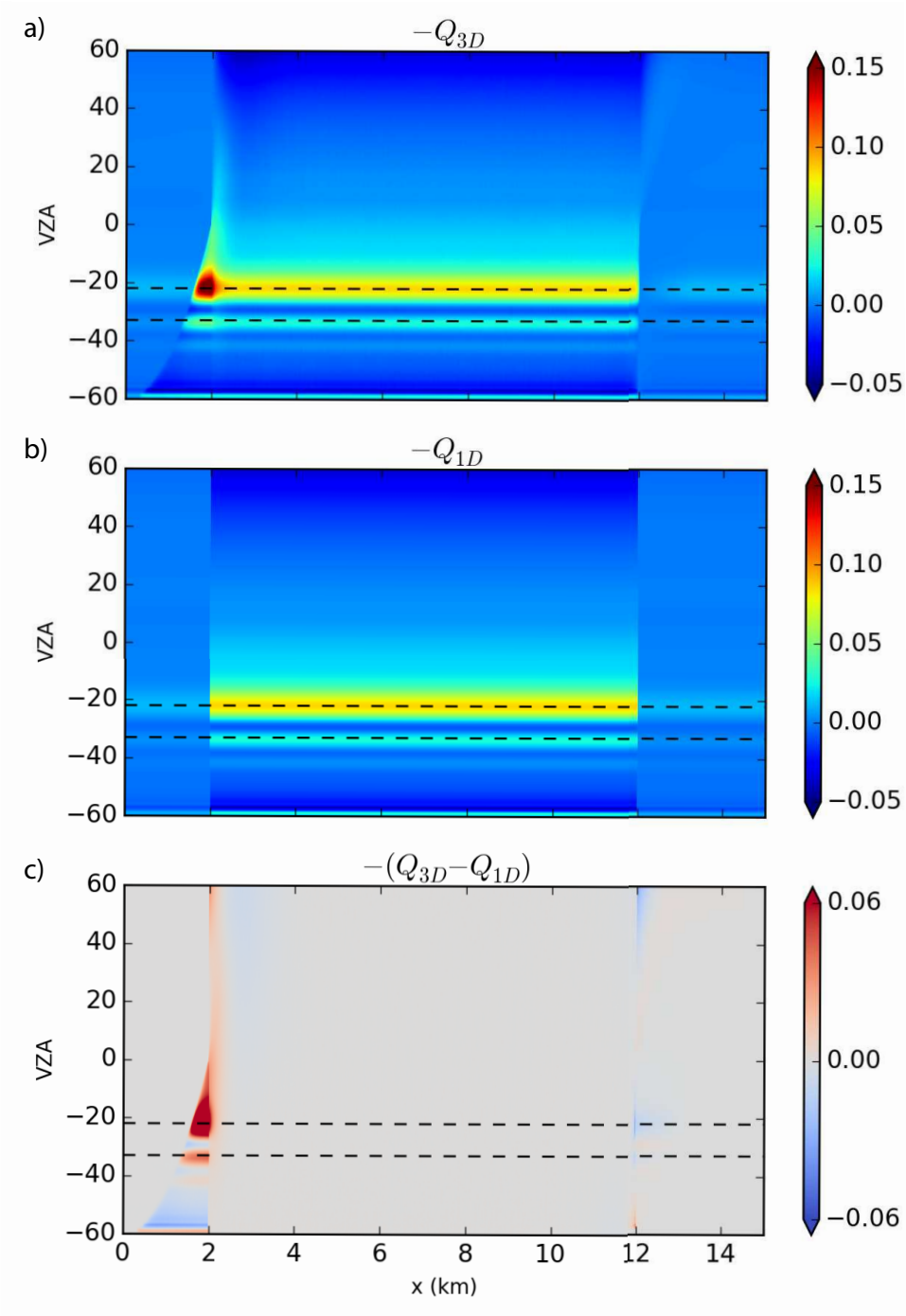

.

Figure 5.5: The spatial and angular dependency of the 1-D and 3-D polarized reflectance of the step cloud scene is shown in panel (a) and (b) respectively. The bias between the two reflectances is introduced in panel (c). Viewing angles that correspond to the scattering geometries of the primary and supernumerary bow are highlighted with dashed black lines.

Taking this analaysis a step further, the angular and spatial dependence of these 3-D effects is fully examined in Figure 5.5. This examination also demonstrates that the primary cloud bow (at VZA $= 0°$) suffers the greatest enhancement due to illumination. Some of the observed VZA dependence stems from the parallax effect. For example, a really oblique viewing angle of VZA $= -60°$ looking at the cloud reflectance at 1 km observe a larger optical optical path because it is viewing through the thin cloud region and into the thick cloud region. For a polarized reflectance this parallax effect can be important if the thin cloud region observed has $\tau_{\text{tot}} < 3$ because the additional optical path length can increase the polarized reflectance. Note that while, the importance of this parallax effects is sensitive to cloud top height, we have not explicitly explored that concept here.

5.4.2 Step Cloud Retrievals

Performing bispectral and polarimetric cloud retrievals on the step cloud reflectances we can begin to diagnose how horizontal photon transfer influences cloud retrievals. Focusing on the bispectral retrievals first, we see in panel (a) and (b) of Figure 5.6 that the bispectral retrieval of $r_e(2.13\,\mu\text{m})$ and $\tau_{\text{tot}}(2.13\,\mu\text{m})$ are both influenced by 3-D effects near the illuminating and shadowing side of the cloud scene. The significant increase in the $0.865\,\mu$m reflectance on the illuminating side results in a over-estimated bump in the retrieved $\tau_{\text{tot}}(2.13\,\mu\text{m})$. While the shadowed side on the other hand is darkened, reducing the τ_{tot} retrieval and in one case near cloud edge reducing it so much that it falls outside of the bispectral LUT-space resulting

in a failed retrieval.

The bispectral $r_e(2.13\,\mu\text{m})$ retrieval also exhibits 3-D effects that are dependent on the $2.13\,\mu\text{m}$ reflectance biases observed previously. On the illuminating side of the thick-cloud region we observe a decrease in the $r_e(2.13\,\mu\text{m})$ retrieval because of the increased reflectance, $I(2.13\,\mu\text{m})$. The bispectral retrieval uses droplet absorption to infer r_e, so an increase in the $I(2.13\,\mu\text{m})$ 3-D reflectance is construed here as a reduced droplet size because smaller droplets are less absorptive. As is evident in, Figure 5.6 the τ_{tot} retrieval largely follows the behavior of the $I(0.865\,\mu\text{m})$ reflectance, while the bispectral r_e retrieval has biases associated with 3-D effects that are dependent on the both the VNIR and SWIR reflectances. This is evident in the region just outside the thick cloud on the illuminating and shadowing side. In this region, some multiply-scattered $I(0.865\,\mu\text{m})$ photons are able to either scatter from the τ_{thk} region and into the τ_{thn} region. This source of increased VNIR reflectances increases the $\tau_{\text{tot}}(2.13\,\mu\text{m})$ retrieval moderately, but also increases the $r_e(2.13\,\mu\text{m})$ retrieval. This occurs because the bispectral LUT exhibits a strong correlation between VNIR and SWIR reflectances when τ_{tot} is small, resulting in biases due to 3-D effects associated with either spectral band. As discussed previously in chapter 4 this region of the LUT is a source of numerous retrieval errors. It should also be noted that the noisiness in the r_e retrieval in the thin cloud region is likely attributable to small Monte Carlo fluctuations in the reflectances that are exacerbated by the sensitivity of this region of the LUT to even small changes in cloud reflectance.

In contrast to the bispectral retrievals, the polarimetric retrieval of $r_e(\text{pol})$ in

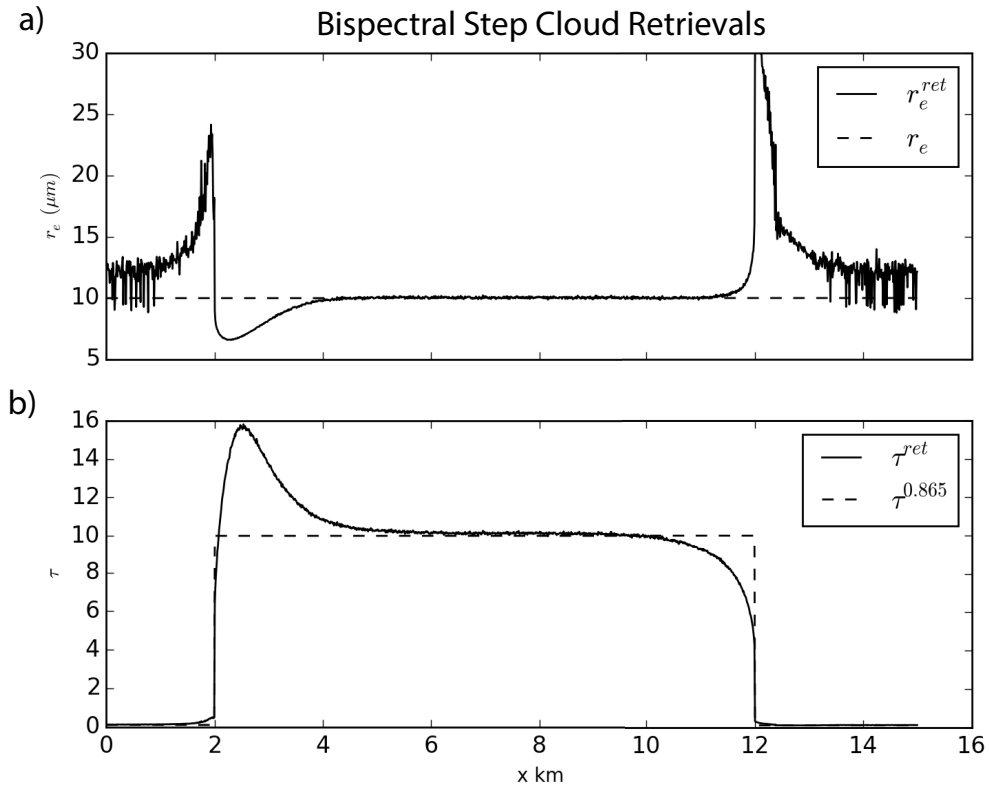

Figure 5.6: The 1-D and 3-D step cloud model retrievals using the bispectral (2.13 μm) (panel a) and polarimetric (panel b) techniques. Note that the original properties of the scene are $r_e = 10\,\mu$m, $\tau_{\text{thk}} = 10$, $\tau_{\text{thn}} = 0.1$.

the step cloud case is more spatially consistent. The r_e(pol) retrieval is accurate throughout most of the scene, but has a small $< 1\,\mu$m dip near the illuminating cloud edge to the left of the thick cloud. There is another jump very slight change in the retrieval near the shadowed cloud side at 12 km. This is consistent with the results in Figure 5.4(a), where we saw the positions of the supernumerary and primary bows were very stable even near the cloud edges. In contrast, the v_e(pol) retrieval appears to sensitive to the step cloud edges, with a jump down to a lower v_e just before the cloud step at 2 km and then a rapid increase within the thick illuminated cloud edge. On the shadowed cloud edge, v_e drops to it's lowest value as the supernumerary bow peaks are depressed (as demonstrated in Figure 5.4(b)). Within the cloud, the v_e(pol) retrieval oscillates between two grid point values at 0.02 and 0.03. This oscillation could be an artifact of the retrievals sensitivity to noise in the 3-D monte carlo reflectances. In practice, observational v_e(pol) retrievals behave in a similar manner, with locally variable oscillations [*Alexandrov et al.*, 2015].

The τ_{tot}(pol) retrieval is another story. This retrieval, which is based on the constrained bispectral LUT approach, discussed in subsection 2.3.2, largely shares the same sensitivity to 3-D effects present in the bispectral τ_{tot} retrieval. Because these retrievals are effectively the same, the 3-D effects induced in the τ_{tot}(pol) follow the same behavior as the $\tau_{\text{tot}}(2.13\,\mu\text{m})$ retrieval discussed here and throughout the literature [*Várnai and Marshak*, 2002b].

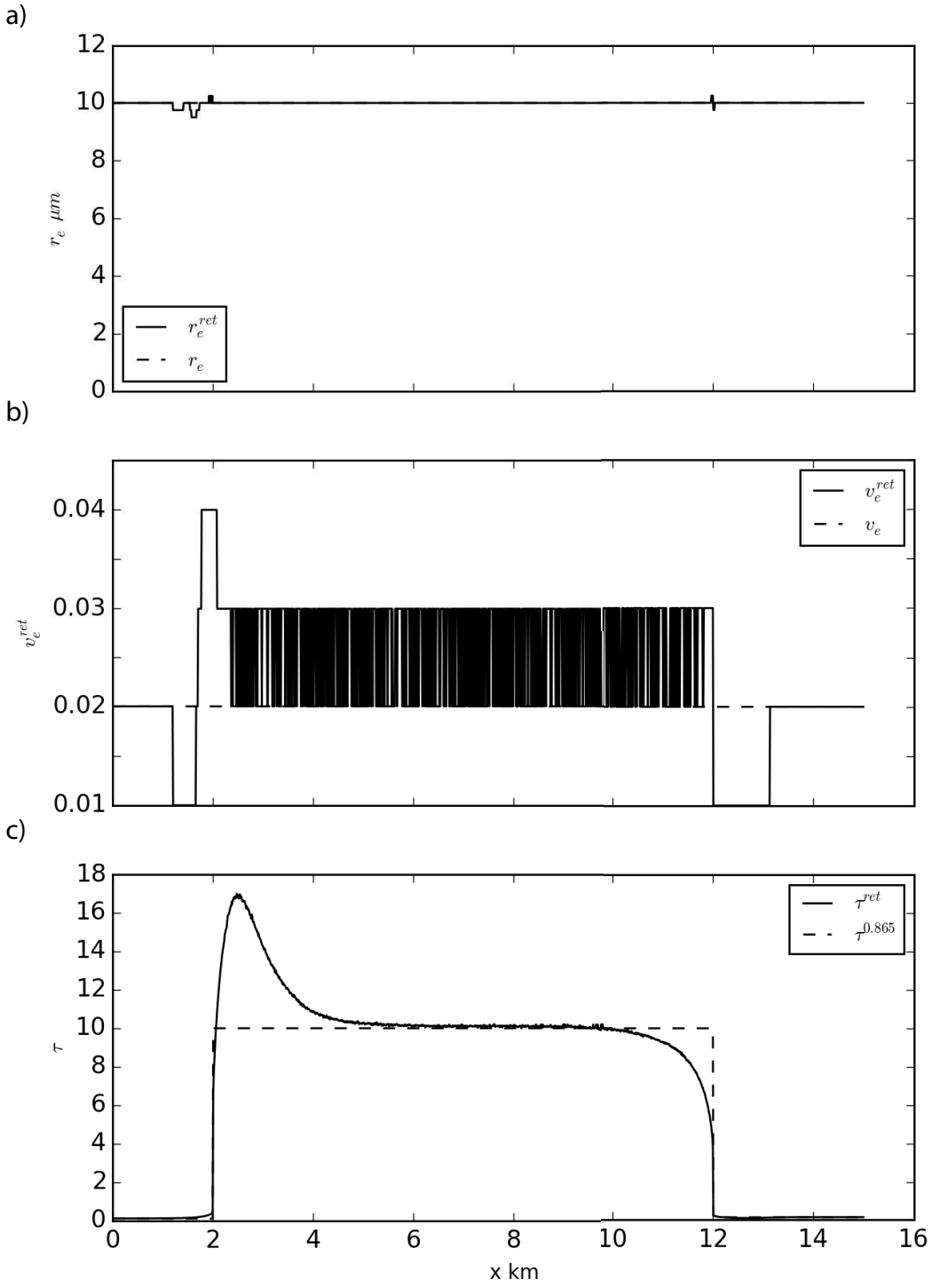

Figure 5.7: Polarimetric retrievals of r_e(pol), v_e(pol), and τ(pol) (panel a,b, and c repsectively) for the 3-D reflectances observed in the step cloud model. Note that the original properties of the scene are $r_e = 10\,\mu$m, $v_e = 0.02$, and $\tau_{\text{thk}} = 10$, $\tau_{\text{thn}} = 0.1$.

5.4.3 Fractal Cloud Reflectances

The spatial variability of the step cloud is too simplified to extend our understanding of 3-D effects much further. The fractal cloud scene introduces the sort of spatial inhomogeneity in cloud LWP and optical thickness required for a more rigorous study. To that end, we first analyze the spatial variability of the nadir viewing total reflectances of the fractal cloud scene in Figure 5.8 for $SZA = -60°$. These nadir viewing reflectances make it clear that there are significant differences between the 3-D and 1-D reflectances for this inhomogeneous cloud scene. For very large SZA, the influence of shadowing and illuminating effects dominates over the influence of radiative smoothing. This is evident in the $I(0.865\,\mu\text{m})$ band, where large-scale illuminating/shadowing effects are evident. In this case, higher reflectances appear on sunward side of thick cloud regions and lower reflectances on the shadowed side. Even for this really oblique SZA, radiative smoothing still dominates 3-D effects at small-scale. For example, there is a clear reduction in the high-frequency oscillations of the 1-D $I(0.865\,\mu\text{m})$ total reflectance due to radiative smoothing. In the more strongly absorbing bands like $I(2.13\,\mu\text{m})$ and $I(3.75\,\mu\text{m})$ this high SZA case leads to significant roughening of large scale features due to the impact of the shadowing/illuminating effects at the large scale.

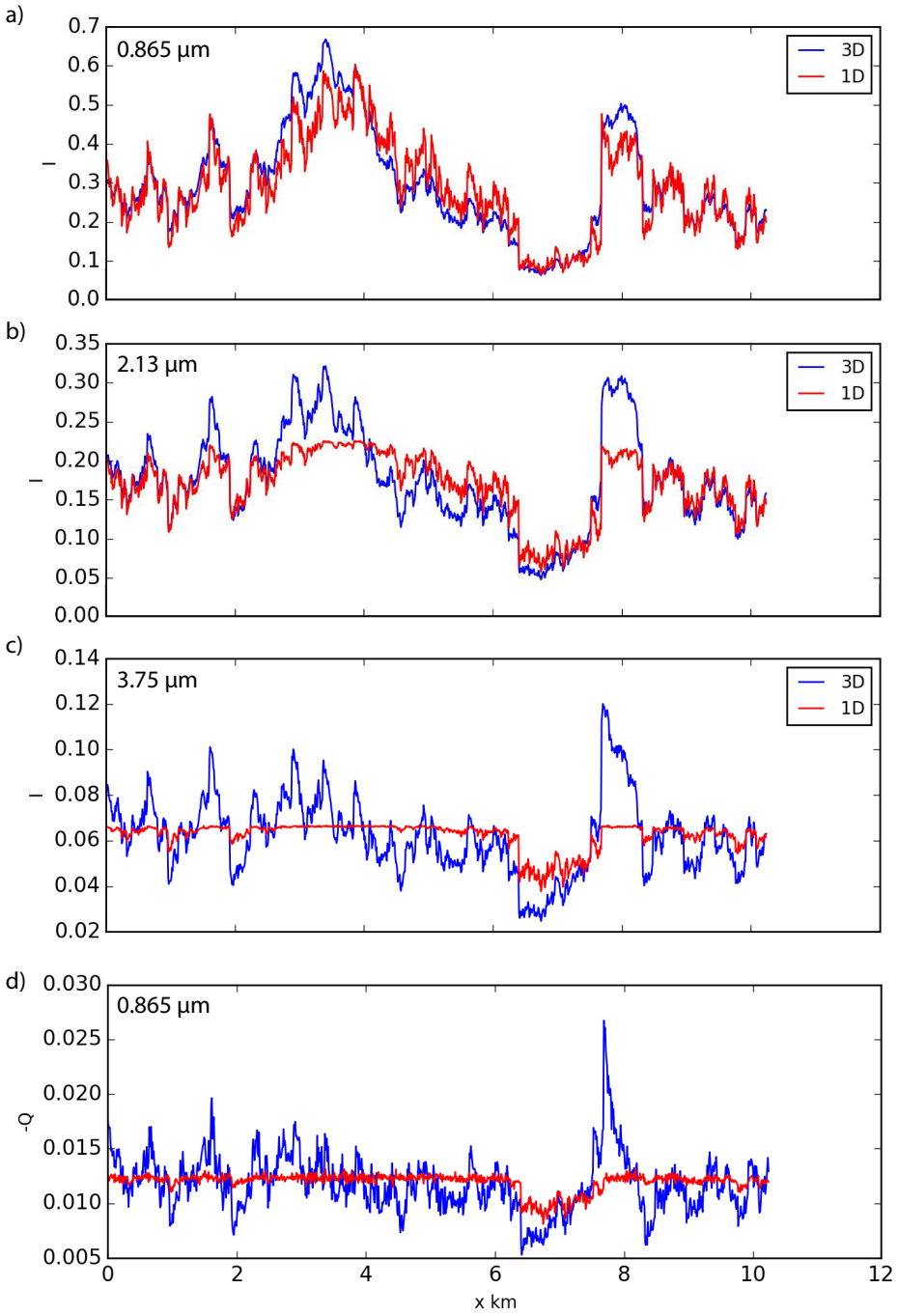

Figure 5.8: Nadir viewing fractal cloud total reflectances for $\lambda = 0.865$, 2.13, and 3.75 μm in panel (a), (b) and (c) respectively. All reflectances are observed at the following geometry: SZA = 60°, VZA = 0°, and RAA = 0°. In addition to the total reflectances, the polarized reflectance for $\lambda = 0.865\,\mu$m is in panel (d).

The most extreme example of spatial roughening is observed in the polarized reflectances. The 1-D polarized reflectance is nearly constant throughout this scene, but the 3-D polarized reflectances have significantly higher spatial variability. As demonstrated in the step cloud study, the angular variability of 3-D polarized reflectances is significantly different from 1-D polarized reflectances. To that end, we can address the angular and spatial variability of the polarized reflectance in the fractal cloud scene in Figure 5.9 in the same manner as we did for the step cloud. One consequence of the microphysical homogeneity of the scene is that the 1-D polarized reflectance field is nearly constant throughout all the regions of the cloud and at all viewing angles. The only exception to this is in the thin regions with $\tau_{\text{tot}} < 3$ where the influence of multiple scattering introduces subtle differences in 1-D reflectance bow features before saturating around $\tau_{\text{tot}} > 3$. This means that nearly all of the variability in the bias plot in Figure 5.9(c) is a result of the 3-D reflectance field. The bias between 3-D and 1-D reflectances is shown here as a spatial/angular map, displaying how the spatial inhomogeneity of optical thicknesses influences the angular scattering features of the cloud. There are few important features in the angular and spatial variability of thsi bias:

- The magnitude and variability in the bias between 3-D and 1-D reflectances is again greatest in the primary and supernumerary cloudbow features.

- The locations of large spikes in the τ_{tot} appear to define boundaries between illuminating and shadowing features, a finding consistent with the step cloud case.

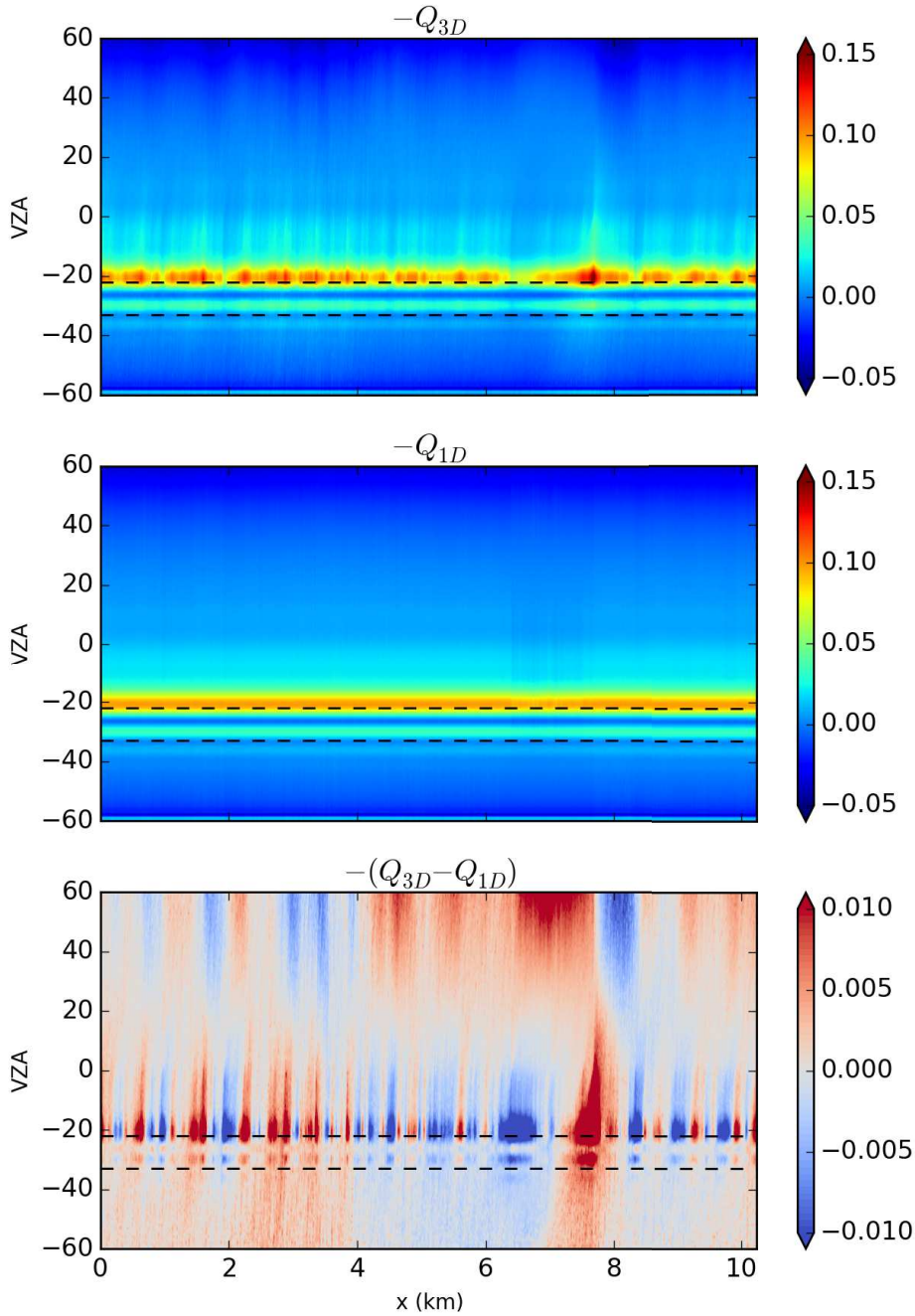

Figure 5.9: The spatial and angular dependency of the 1-D and 3-D polarized reflectance of the fractal cloud scene is shown in panel (a) and (b) respectively. The bias between the two reflectances is introduced in panel (c). Viewing angles that correspond to the scattering geometries of the primary and supernumerary bow are highlighted with dashed black lines.

- For a scene with homogeneous r_e and v_e, the bias between 3-D and 1-D reflectances is much smaller at viewing angles where the polarized phase function $-P_{12}$ crosses zero (e.g. 20°).

5.4.3.1 Radiative Smoothing and Roughening

The reliable spectral slope of the fractal scene ($\beta = 5/3$) allows us to test beyond simple illuminating/shadowing effects, but can allow us to probe the behavior of radiative smoothing. The power spectral density (PSD) can help diagnose these 3-D effects in the fractal cloud case[2]. As described in subsection 5.3.3, the PSD can identify the characteristic scale break associated with radiative smoothing caused by horizontal photon transfer. In this section we will focus first on the total reflectance, where known features of the 3-D reflectance PSD's can be demonstrated. The PSD's for three different viewing angle geometries (VZA$-60°$ (a), VZA $= -20°$ (b), and VZA $= 0°$ (c)) are shown in Figure 5.10. Examining the angular variability of the PSD allows us to develop an understanding how the smoothness of the scene changes with viewing geometry. Numerous studies discuss reflectance scale breaks for nadir viewing geometries [*Davis et al.*, 1997b]. This is perhaps because the influence of radiative smoothing dominates in nadir viewing geometries over the influence of illuminating/shadowing 3-D radiative effects. However, there still has not been much discussion of viewing angle dependence of the cloud reflectance PSD. These results indicate that the location of this scale break and the small-scale

[2]Note that the fractal case used in this section of the study has a different aspect ratio, with resolution ($\Delta x = 50\,\mathrm{m}$) and cloud geometrical thickness ($H = 50\,\mathrm{m}$) altered to span an appropriate range of spatial scales in order to resolve scale breaks.

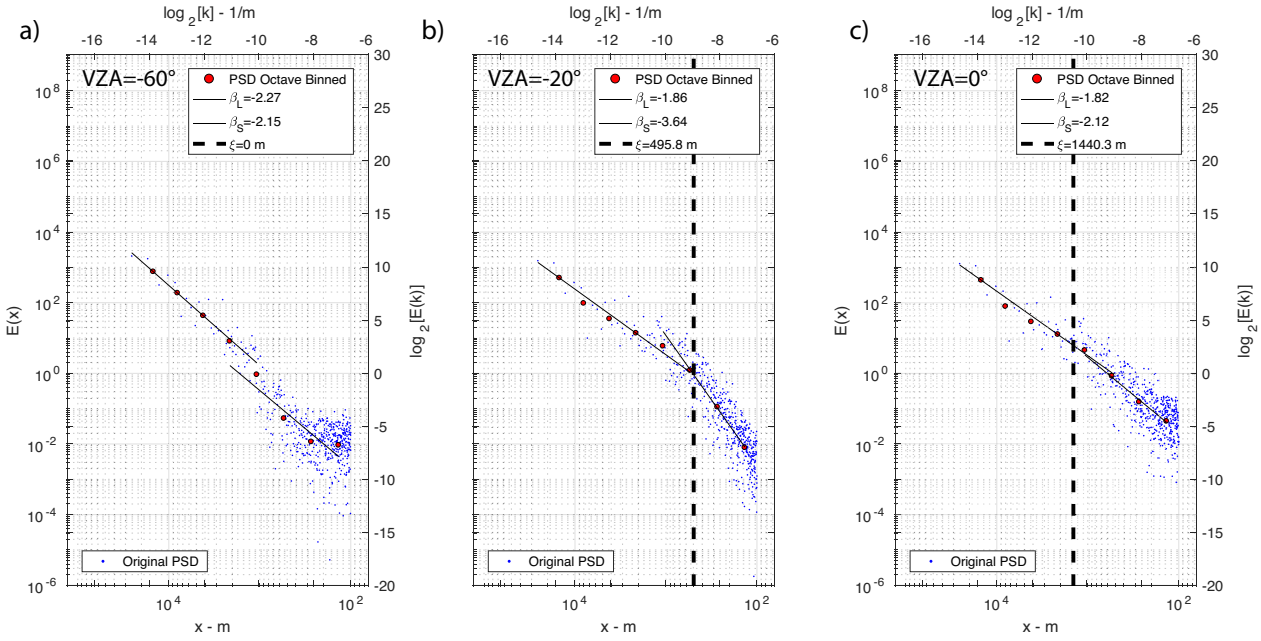

.

Figure 5.10: Spectral power distributions of the fractal cloud scene total reflectances. These PSD's demonstrate that for VZA $= -60°$, VZA $= -20°$, and VZA $= 0°$ (panel a, b, and c respectively) the PSD displays different spectral slope and scale break properties. For more information on interpreting these figures, refer back to Figure 5.2

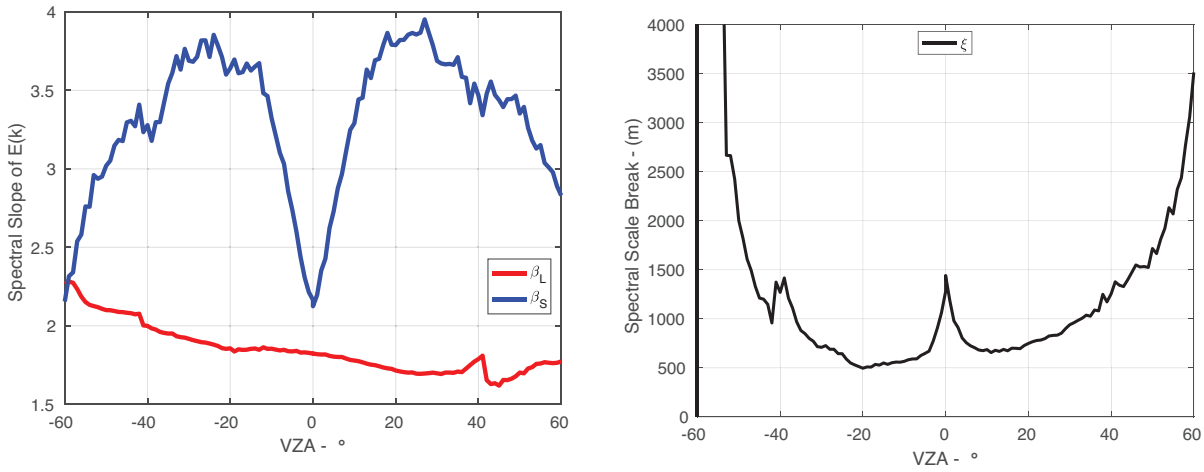

Figure 5.11: Panel (a) displays the angular variability of the large scale (β_{L}) and small scale (β_{S}) spectral slopes. Panel (b) depicts the scale break defined using the large scale and small scale curve-fits.

spectral slope (associated with radiative smoothing) are highly dependent on the viewing geometry. Analyzing all of the viewing angle geometries, we can obtain the VZA dependence of the small and large-scale spectral slopes, in addition to the anticipated scale break. To that end, Figure 5.11 reveals that the difference between the small and large scale spectral slope plummets near nadir-viewing geometries. For most viewing geometries, the large scale spectral slope is approximately similar to the expected $k^{-5/3}$ relationship, however the small scale variability diverges from this behavior when there is significant radiative smoothing. In addition, the scale break (ξ) calculated using the spectral slopes, indicates that the scale-break near nadir is larger than the minimum scale break observed at VZA $\approx -20°$ (this VZA corresponds to the primary bow scattering angle). In addition, the rapid decrease of the small scale spectral slope for large viewing angles leads to scale breaks that become large and probably non-physical.

At oblique viewing geometries (i.e. $\pm 60^{\circ}$) the fractal cloud case sometimes exhibits more than one scale break regime (refer to Figure 5.10(a)). One scale break around $\approx$ 1 km and another approaching 100 m resolution. The presence of this small-scale break is associated with a very small spectral slope (β) and can result in contamination of the spectral slope fit. These flat small-scale slopes are characteristic of spectral "white noise", indicating that these spatial scales are increasingly uncorrelated and equally probable.[3] One way to test these ideas is to run a small-window smoothing filter through the reflectances at -60° and observe how the PSD changes. If it is truly a noisy signal then we will find that the small-scale averaging window does not alter the PSD at these small scales. However, we find that the PSD is indeed modified after applying this filter. Given this result, it is most likely that this white noise is associated with Monte Carlo noise in the modeled reflectances at these oblique viewing angles. Note that for this directly back-scattering viewing geometry such Monte Carlo noise is common.

To our knowledge an examination of the power spectral density of polarized cloud reflectances has never been performed. We find that the PSD of the polarized reflectance, behaves in a significantly different manner than the total reflectance or cloud LWP field, with a few characteristic properties:

- The small-scale spectral slope in the primary and supernumerary cloudbow angles exhibits radiative smoothing similar to the total reflectance.

- At nadir viewing, $\beta_S = \beta_L \approx 5/3$, despite exhibiting roughening at intermedi-

[3]It is also interesting to note that in signal analysis, stochastic signals with spectral slopes of -2

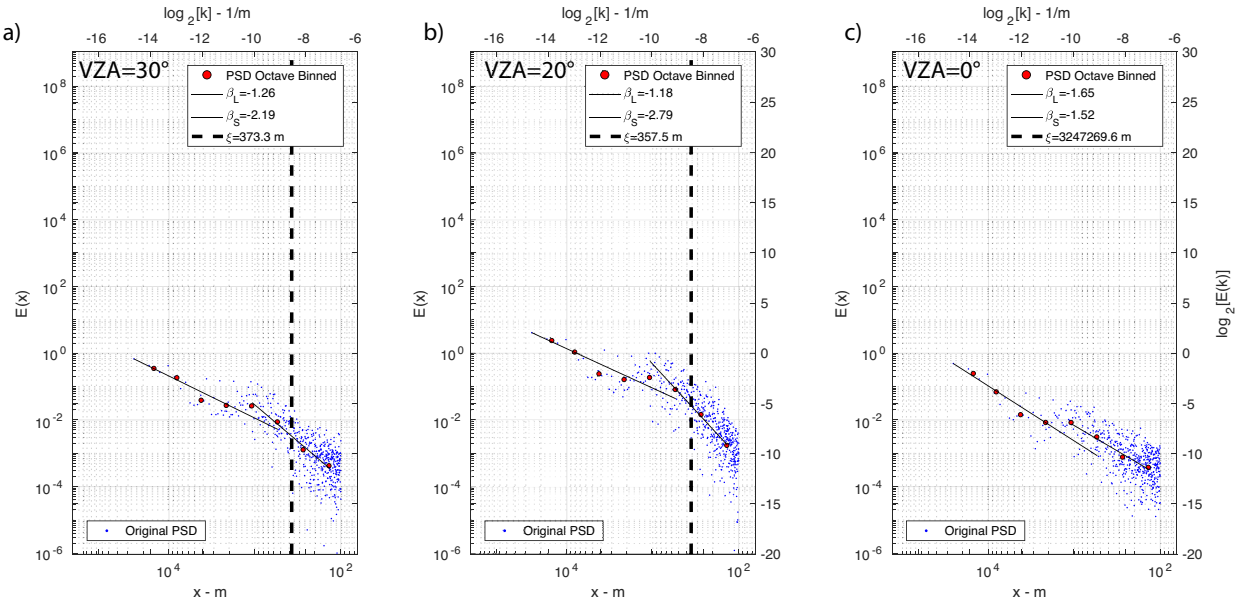

Figure 5.12: Power spectral distributions of the fractal cloud scene polarized reflectances. These PSD's demonstrate that for VZA$-60°$, VZA $= -20°$, and VZA $= 0°$ (panel a, b, and c respectively) the PSD displays different spectral slope and scale break properties. For more information on interpreting these figures, refer back to Figure 5.2

ate scales.

- At intermediate scales there is typically a more pronounced knee, associated with roughening (rather than smoothing), indicating that polarized reflectance fluctuations at this scale are greater than those of optical depth.

- For viewing angles where $Q \approx 0$ the small scale slopes become flatter, this could be an artifact of Monte Carlo noise.

The variability of the spectral slopes for the polarized reflectance is shown in Figure 5.13. These results demonstrate that the primary and supernumerary bow spectral slopes behave like the total reflectance, with a large-scale spectral slope

are described as "brown(ian) noise" because the spectral slope -2 is characteristic of the diffusion length scale of Brownian stochastic signals.

similar to $\beta = 5/3$ and a smoothed small-scale spectral slope. This similarity is largely the result of these cloudbow features exhibiting the greatest sensitivity to τ_{tot} variability. We were able to confirm that this feature was a function of the cloudbow scattering angle and not VZA by identifying the same feature in the PSD for SZA $= -40°$ at different VZA that also corresponded to the cloudbow features for that solar geometry. The constant $\beta = 1.6 \approx 5/3$ slope at nadir viewing reveals a promising feature of polarized reflectances. For example it could possibly be used to provide a method for probing the scaling features of the physical scene via remote sensing, without the influence of radiative smoothing. Again, we tested the SZA dependence of this feature to determine if this was a scattering angle dependent or nadir viewing feature of the polarized reflectance. Examining the SZA $= 40°$ polarized PSD revealed that the viewing angle where the small and large-scale slopes cross moved to VZA $= +20°$, an indication that this too was a scattering angle dependent phenomenon.

The presence of the pronounced roughening at intermediate scales makes it algorithmically difficult to determine the scale break for the polarized reflectance PSD. By visual inspection, this intermediate roughening scale between large and small scale variability consistently occurred around 1 km. It has been demonstrated that for total reflectance PSD's, increased absorption and large SZA led to greater roughening at intermediate scales (refer to fig 12.19 in *Marshak and Davis* [2005]). For a strongly absorbing/depolarizing reflectance, this roughening is a characteristic of the domination of single-scattering illuminating and shadowing effects over the multiply-scattered radiative smoothing effects. The roughening of the PSD for po-

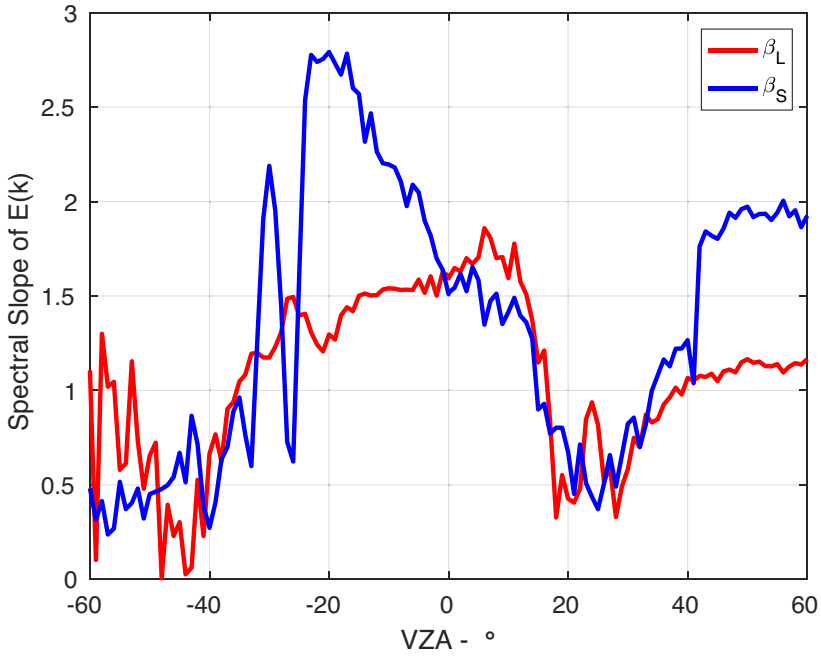

Figure 5.13: The angular variability of the large scale (β_{L}) and small scale (β_{S}) spectral slopes. Panel (b) depicts the scale break defined using the large scale and small scale curve-fits. Note that the oscillations in the small scale slope between $VZA = -20°$ and $-40°$ are associated with the primary and supernumerary cloud-bows.

larized reflectances is likely similarly related to the importance of single-scattering, and the scale where roughening occurs is likely associated with a depolarization length-scale. Further research is required in order to develop this idea further with regard to polarized reflectances.

5.4.4 Fractal Cloud Retrievals

Performing bispectral and polarimetric retrievals on the fractal cloud model will help to illustrate how radiative smoothing and roughening can impact the retrievals in the spatially inhomogeneous cloud scene. The results of these retrievals are shown in Figure 5.14. Where it is evident that both the bispectral $\tau_{\mathrm{tot}}(2.13\,\mu\mathrm{m})$

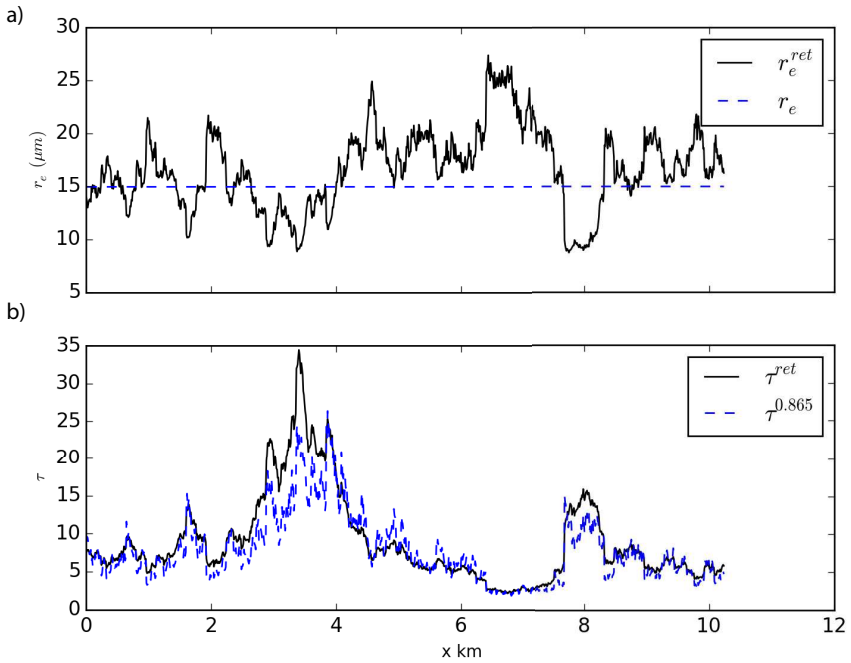

Figure 5.14: Bispectral retrievals of fractal cloud properties for $SZA = -60°$ and $VZA = 0°$. There are clear, systematic biases in the $r_e(2.13\,\mu\text{m})$ retrieval (solid black line) and $r_e = 15\,\mu\text{m}$ (blue dashed line). The $\tau(2.13\,\mu\text{m})$ retrieval on the other hand is doing comparatively better.

and $r_e(2.13\,\mu\text{m})$ suffer from 3-D radiative effect biases. In the case of $\tau_{\text{tot}}(2.13\mu\text{m})$ these biases largely follow the spatial structure of the $I(0.865\,\mu\text{m})$ reflectances in Figure 5.8(a). The retrieval biases observed here are expected in such low-sun conditions dominated by illuminating and shadowing effects.

For the $r_e(2.13\,\mu\text{m})$ retrieval, shown in Figure 5.14(b), the illuminating and shadowing effects of both the $I(0.865\,\mu\text{m})$ and $I(2.13\,\mu\text{m})$ reflectances influence the retrieval. As discussed previously for the step cloud case, in thick cloud regions, the illuminating effects in the SWIR band dominates the r_e bias leading to $r_e < 15\,\mu\text{m}$ (for example, in the thick regions near 2 km and 8 km). Whereas in the thin cloud regions, the co-variability of the shadowing effects in both the VNIR and SWIR leads to an r_e bias with $r_e > 15$

Previously, the polarized reflectances in Figure 5.9(c) revealed strong sensitivity to 3-D effects in certain scattering angles. However, despite this the polarimetric retrievals in Figure 5.15 demonstrates far less sensitivity to the highly inhomogeneous cloud field. For example, the r_e(pol) retrieval in Figure 5.15(a) retrieval is highly stable throughout the retrieval scene. This result is consistent both with our own results in the step cloud case as well as other studies [*Alexandrov et al.*, 2012a]. On the other hand, v_e(pol) retrieval in Figure 5.15(b) again indicates some instability, leaping between two possible solutions for v_e. This variability, the retrieval does not suffer large biases. In section 5.5 we will discuss reasons why the polarimetric v_e(pol) retrieval does not exhibit any variability despite clear impacts on the 3-D polarized reflectances.

5.5 Summary and Discussion

In the step cloud case the broadness of the illuminating or shadowing features were found to be dependent on multiple scattering, the single scattering albedo, and depolarization. This dependence on the single scattering albedo leads us to believe that strongly absorbing bands, or reflectances dominated by single scattering (like the polarized reflectance) will reduce the broadness of illuminating and shadowing effects. However, despite the spatial extent of 3-D effects being lessened for these absorbing and depolarizing bands we also found that the local illuminating and shadowing effect biases were more severe. We also demonstrated that the influence of 3-D effects in polarized reflectances was highly dependent on viewing geometry,

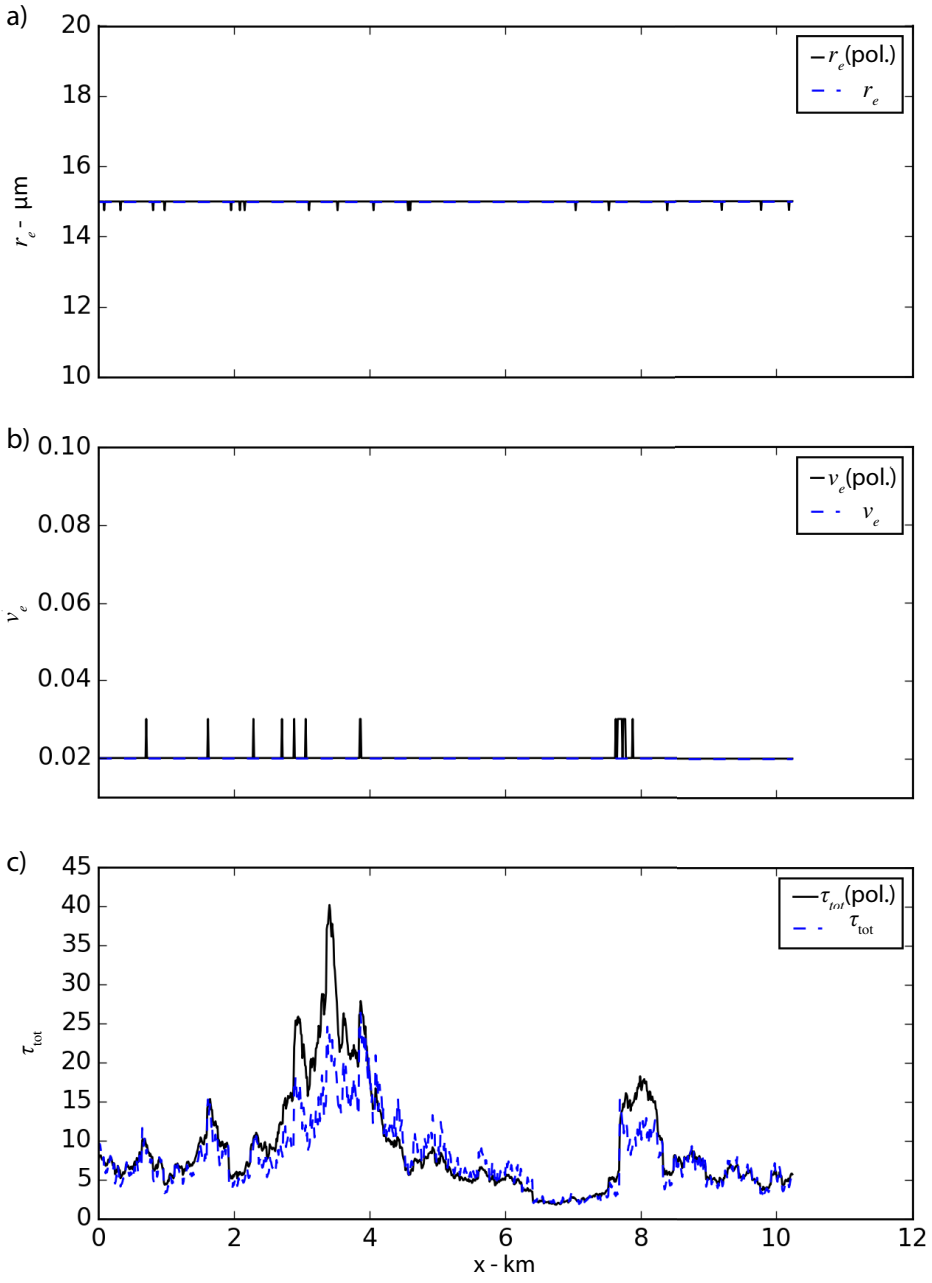

Figure 5.15: Polarimetric retrievals of r_e(pol), v_e(pol) and $\tau_{\rm tot}$(pol) (panels a,b, and c respectively) of the fractal cloud scene for $SZA = -60°$ and $VZA = 0°$. There are clear, systematic biases in the $r_e(2.13\,\mu{\rm m})$ retrieval (solid black line) and $r_e = 15\,\mu{\rm m}$ (blue dashed line). The $\tau_{\rm tot}$(pol) retrieval on the other hand is doing comparatively worse.

with the greatest illuminating and shadowing effects impacting the primary and supernumerary cloudbow scattering angles.

The bispectral retrievals of the step cloud scene helped solidify our understanding of the impacts of illuminating and shadowing effects on cloud remote sensing. In our low sun experiments ($SZA = -60°$) we found that 3-D effect bias of the $r_e(2.13\,\mu\text{m})$ retrieval was complicated. The scene average retrieval was found to be biased high, despite expecting that illuminating effects in the SWIR band would lead to a low-biased retrieval. This resulted in r_e retrievals in the τ_{thn} region were biased high due to illuminating effects in the VNIR band in this region. The change in VNIR reflectance, coupled with the the correlated dependency of the VNIR and SWIR reflectances for small τ_{tot}, led to systematically high-biased r_e. This coupled dependency can become more or less important depending on the difference between τ_{thn} and τ_{thk}. In this case, because τ_{thn} was very small compared to τ_{thk} this bias was enhanced. Further study should examine the behavior of this bias as a function of the ratio of τ_{thn} to τ_{thk}.

The polarimetric retrieval of $r_e(\text{pol})$ was found to be highly robust to the influence of the step cloud, with $< 1\,\mu\text{m}$ biases within $\approx 100\,\text{m}$ of the cloud edges. This step cloud case study was incapable of reproducing the systematic high bias in the $v_e(\text{pol})$ retrieval that was presented in *Alexandrov et al.* [2012a]. We were however able to demonstrate that the $v_e(\text{pol})$ retrieval was influenced by inhomogeneity in the step cloud case. We find that the $v_e(\text{pol})$ retrieval is biased low on the shadowing cloud side from cloud edge to $\approx 1\,\text{km}$ away, whereas on the illuminating side the $v_e(\text{pol})$ retrieval is biased low in the thin cloud region, but high in the thick cloud

region. More work needs to be done to explore the behavior of these biases as a function of other values of v_e and other forms of inhomogeneity (e.g., r_e inhomogeneity). In general, 3-D effects that lead to decreases in the v_e(pol) retrieval could further low bias this retrieval in addition to the low biases discussed in chapter 4.

We find significant spatial inhomogeneity of the $-(Q_{3D} - Q_{1D})$ biases in the fractal cloud field. As in the step cloud case, we examined how this variability changes with viewing angle in order to develop an understanding as to how it may be able to influence multi-angular polarimetric retrievals. The fractal cloud also enabled us to examine the PSD of polarized reflectances, revealing several interesting features. The spectral variability in the primary and supernumerary cloud bow angles ($\Theta = 140, 150°$ in this case) was reminiscent of the scale breaks observed in total reflectance fields. This similarity leads us to believe that 3-D radiative effects are likely also smoothing the polarized reflectances. We also found that at around $\Theta = 120°$, near the secondary bow angle, the spectral slope of the polarized PSD as large and small scales were equal to one another ($\beta_L = \beta_S \approx 5/3$). The equivalence of the spectral slope at this angle to the physical spectral slope of $\beta = 5/3$ indicates that if this effect is also present in observational data it could be used as a proxy to remotely sense the physical spectral slope.

The Fourier transform (and curve-fitting) approach used to characterize radiative smoothing encountered numerous difficulties. For one, a higher-order fractal model with an aspect ratio ($H/\Delta x$) more appropriate for radiative smoothing studies because it could span larger orders of magnitude in spatial scale. Future studies should also consider replacing or expanding on the octave binning scheme. A bin-

ning scheme that provides more data-points for curve fitting would be of a great asset to this analysis. A future study might consider using a sliding-octave-binning scheme that could provide numerous data points and a smooth PSD for fitting. Such a modification would make handling the cases with intermediate roughening scales in the polarized reflectance easier to discern and fit the large and small scale features without including the enhancement in the knee of the PSD. Additionally, as *Oreopoulos et al.* [2000] and others have pointed out, the fourier PSD is not quite as robust at small-scales as a short-lag autocorrelation. It is possible that such an approach would be able to help distinguish small-scale features from Monte Carlo variability. In a future study, the autocorrelation of the polarized reflectances (as a function of viewing angle) should be examined.

Again, the fractal cloud model revealed no major r_e(pol) retrieval biases. The 3-D effects observed in this study didn't appear to alter the angular pattern of polarized reflectances, rather it increased and decreased reflectances in specific angles. This is perhaps unsurprisingly, given the finding of others who have looked into polarimetric r_e(pol) retrieval sensitivities ([*Alexandrov et al.*, 2012a]). The fractal cloud case also demonstrated that the v_e(pol) was unaffected by any clear retrieval bias. A future study might test whether the selected homogeneous v_e of the fractal/step cloud case influences the polarimetric retrieval bias. Additionally, the role of 3-D effects in a microphysically inhomogeneous (i.e., r_e variability) scene would also be very important.

As discussed briefly in section 5.2, there are polarimetric instruments that make use of the DOLP for the purposes of their retrievals. The behavior of total

and polarized reflectances in the $\lambda = 0.865\,\mu$m spectral band is quite different, and this can lead to some significant consequences for the 3-D DOLP. The total and polarized reflectances have vastly different radiative smoothing scales and this could induce more complicated 3-D effects for the DOLP. While the polarimetric retrievals implemented in this study do not make use of the DOLP, it will be important for future studies to consider this sort of 3-D radative effect.

Bibliography

Ackerman, A. S., P. V. Hobbs, and O. B. Toon (1995), A model for particle microphysics, turbulent mixing, and radiative transfer in the stratocumulus-topped marine boundary layer and comparisons with measurements, *Journal of the Atmospheric Sciences*, *52*(8), 1204–1236.

Ackerman, A. S., M. P. Kirkpatrick, D. E. Stevens, and O. B. Toon (2004), The impact of humidity above stratiform clouds on indirect aerosol climate forcing, *Nature*, *432*(7020), 1014–1017.

Ackerman, A. S., M. C. vanZanten, B. Stevens, V. Savic-Jovcic, C. S. Bretherton, A. Chlond, J.-C. Golaz, H. Jiang, M. Khairoutdinov, S. K. Krueger, D. C. Lewellen, A. Lock, C.-H. Moeng, K. Nakamura, M. D. Petters, J. R. Snider, S. Weinbrecht, and M. Zulauf (2009), Large-Eddy Simulations of a Drizzling, Stratocumulus-Topped Marine Boundary Layer, *Monthly Weather Review*, *137*(3), 1083–1110, doi:10.1175/2008MWR2582.1.

Agee, E. M., T. S. Chen, and K. E. Dowell (1973), A Review of Mesoscale Cellular Convection, *Bulletin of the American Meteorological Society*, *54*(10), 1004–1012, doi:10.1175/1520-0477(1973)054⟨1004:AROMCC⟩2.0.CO;2.

Alexandrov, M. D., B. Cairns, C. Emde, A. S. Ackerman, and B. van Diedenhoven (2012a), Accuracy assessments of cloud droplet size retrievals from polarized reflectance measurements by the research scanning polarimeter , *Remote Sensing of Environment*, *125*, 92–111, doi:10.1016/j.rse.2012.07.012.

Alexandrov, M. D., B. Cairns, and M. I. Mishchenko (2012b), Rainbow Fourier transform, *Journal of Quantitative Spectroscopy and Radiative Transfer*, *113*(18), 2521–2535, doi:10.1016/j.jqsrt.2012.03.025.

Alexandrov, M. D., B. Cairns, A. P. Wasilewski, A. S. Ackerman, M. J. McGill, J. E. Yorks, D. L. Hlavka, S. E. Platnick, G. Thomas Arnold, B. van Diedenhoven, J. Chowdhary, M. Ottaviani, and K. D. Knobelspiesse (2015), Liquid water cloud properties during the Polarimeter Definition Experiment (PODEX), *Remote Sensing of Environment*, *169*, 20–36, doi:10.1016/j.rse.2015.07.029.

Baker, M. B., and J. Latham (1979), The Evolution of Droplet Spectra and the Rate of Production of Embryonic Raindrops in Small Cumulus Clouds, *Journal of the Atmospheric Sciences*, *36*(8), 1612–1615, doi:10.1175/1520-0469(1979)036⟨1612:TEODSA⟩2.0.CO;2.

Beals, M. J., J. P. Fugal, R. A. Shaw, J. Lu, S. M. Spuler, and J. L. Stith (2015), Holographic measurements of inhomogeneous cloud mixing at the centimeter scale, *Science*, *350*(6256), 87–90, doi:10.1126/science.aab0751.

Behrangi, A., T. Kubar, and B. Lambrigtsen (2012), Phenomenological Description of Tropical Clouds Using CloudSatCloud Classification, *Monthly Weather Review*, *140*(10), 3235–3249, doi:10.1175/MWR-D-11-00247.1.

Bennartz, R. (2007), Global assessment of marine boundary layer cloud droplet number concentration from satellite, *Journal of Geophysical Research: Atmospheres*, *112*(D2), D02,201, doi:10.1029/2006JD007547.

Boers, R., and R. Mitchell (1994), Absorption feedback in stratocumulus clouds influence on cloud top albedo, *Tellus A*, *46*(3), 229–241, doi:10.1034/j.1600-0870.1994.00001.x.

Boers, R., J. R. Acarreta, and J. L. Gras (2006), Satellite monitoring of the first indirect aerosol effect: Retrieval of the droplet concentration of water clouds, *Journal of Geophysical Research: Atmospheres*, *111*(D22), D22,208–13, doi:10.1029/2005JD006838.

Bony, S., and J. Dufresne (2005), Marine boundary layer clouds at the heart of cloud feedback uncertainties in ....

Brenguier, J.-L., H. Pawlowska, L. Schüller, R. Preusker, J. Fischer, and Y. Fouquart (2000), Radiative Properties of Boundary Layer Clouds: Droplet Effective Radius versus Number Concentration, *Journal of the Atmospheric Sciences*, *57*(6), 803–821, doi:10.1175/1520-0469(2000)057⟨0803:RPOBLC⟩2.0.CO;2.

Brenguier, J.-L., H. Pawlowska, and L. Schüller (2003), Cloud microphysical and radiative properties for parameterization and satellite monitoring of the indirect effect of aerosol on climate, *Journal of Geophysical Research*, *108*(D), 8632, doi:10.1029/2002JD002682.

Brenguier, J. L., F. Burnet, and O. Geoffroy (2011), Cloud optical thickness and liquid water path – does the k coefficient vary with droplet concentration?, *Atmospheric Chemistry and Physics*, *11*(18), 9771–9786, doi:10.5194/acp-11-9771-2011.

Bréon, F. M., and M. Doutriaux-Boucher (2005), A comparison of cloud droplet radii measured from space, *Geoscience and Remote Sensing, IEEE Transactions on*, *43*(8), 1796–1805, doi:10.1109/TGRS.2005.852838.

Bréon, F. M., and P. Goloub (1998), Cloud droplet effective radius from spaceborne polarization measurements, *Geophysical Research Letters*, *25*(11), 1879–1882.

Cahalan, R., W. Wiscombe, A. Davis, and A. Marshak (1997), The Landsat Scale Break in Stratocumulus as a Three-Dimensional Radiative Transfer Effect: Implications for Cloud Remote Sensing, *http://dx.doi.org/10.1175/1520-0469(1997)054¡0241:TLSBIS¿2.0.CO;2*, *54*(2), 241–260, doi:10.1175/1520-0469(1997)054⟨0241:TLSBIS⟩2.0.CO;2.

Cahalan, R. F., W. Ridgway, W. J. Wiscombe, and T. L. Bell (1994), The albedo of fractal stratocumulus clouds, *Journal of the Atmospheric Sciences*, doi:10.1175/1520-0469(1994)051⟨2434:TAOFSC⟩2.0.CO;2.

Cairns, B., E. E. Russell, J. D. LaVeigne, and P. M. W. Tennant (2003), Research scanning polarimeter and airborne usage for remote sensing of aerosols, *Optical Science ...*, pp. 33–44, doi:10.1117/12.518320.

Cho, H. M., Z. Zhang, K. Meyer, M. Lebsock, S. Platnick, A. S. Ackerman, L. Di Girolamo, L. C Labonnote, C. Cornet, J. Riedi, and R. E. Holz (2015), Frequency and causes of failed MODIS cloud property retrievals for liquid phase clouds over global oceans, *Journal of Geophysical Research: Atmospheres*, *120*(9), 4132–4154, doi:10.1002/2015JD023161.

Cornet, C., L. C-Labonnote, and F. Szczap (2009), Three-dimensional polarized Monte Carlo atmospheric radiative transfer model (3DMCPOL): 3D effects on polarized visible reflectances of a cirrus cloud, *Journal of Quantitative Spectroscopy and Radiative Transfer*, *111*(1), 174–186, doi:10.1016/j.jqsrt.2009.06.013.

Costantino, L., and F. M. Breon (2013a), Satellite-based estimate of aerosol direct radiative effect over the South-East Atlantic, *Atmospheric Chemistry and Physics Discussions*, *13*(9), 23,295–23,324, doi:10.5194/acpd-13-23295-2013.

Costantino, L., and F. M. Breon (2013b), Aerosol indirect effect on warm clouds over South-East Atlantic, from co-located MODIS and CALIPSO observations, *Atmospheric ....*

Davies, R. (1978), The Effect of Finite Geometry on the Three-Dimensional Transfer of Solar Irradiance in Clouds, *Journal of Atmospheric Sciences*, *35*(9), 1712–1725, doi:10.1175/1520-0469(1978)035⟨1712:TEOFGO⟩2.0.CO;2.

Davis, A., A. Marshak, and W. Wiscombe (1996), Scale invariance of liquid water distributions in marine stratocumulus. Part I: Spectral properties and stationarity issues, *Journal of the Atmospheric Sciences*, *53*(11), 1538–1558, doi:10.1175/1520-0469(1996)053⟨1538:siolwd⟩2.0.co;2.

Davis, A., A. Marshak, and R. Cahalan (1997a), The Landsat scale break in stratocumulus as a three-dimensional radiative transfer effect: Implications for cloud remote sensing, *Journal of the Atmospheric Sciences*, *54*(2), 241–260, doi:10.1175/1520-0469(1997)054⟨0241:tlsbis⟩2.0.co;2.

Davis, A., R. Cahalan, W. Wiscombe, and A. Marshak (1997b), The Landsat Scale Break in Stratocumulus as a Three-Dimensional Radiative Transfer Effect: Implications for Cloud Remote Sensing, *http://dx.doi.org/10.1175/1520-0469(1997)054¡0241:TLSBIS¿2.0.CO;2*, *54*(2), 241–260, doi:10.1175/1520-0469(1997)054⟨0241:TLSBIS⟩2.0.CO;2.

Davis, A. B., and A. Marshak (2001), Multiple Scattering in Clouds: Insights from Three-Dimensional Diffusion/P˜ 1 Theory, *Nuclear science and engineering*.

Davis, A. B., and A. Marshak (2010), Solar radiation transport in the cloudy atmosphere: a 3D perspective on observations and climate impacts, *Reports on Progress in Physics*, *73*(2), 026,801, doi:10.1088/0034-4885/73/2/026801.

De Haan, J. F., P. B. Bosma, and J. W. Hovenier (1987), The adding method for multiple scattering calculations of polarized light, *Astronomy and Astrophysics*, *183*, 371–391.

Deirmendjian, D. (1964), Scattering and polarization properties of water clouds and hazes in the visible and infrared, *Applied Optics*, *3*(2), 187–196.

Deschamps, P. Y., F. M. Breon, M. Leroy, A. Podaire, A. Bricaud, J. C. Buriez, and G. Seze (1994), The POLDER mission: instrument characteristics and scientific objectives, *IEEE Transactions on Geoscience and Remote Sensing*, *32*(3), 598–615, doi:10.1109/36.297978.

Diner, D. J., F. Xu, M. J. Garay, J. V. Martonchik, B. E. Rheingans, S. Geier, A. Davis, B. R. Hancock, V. M. Jovanovic, M. A. Bull, K. Capraro, R. A. Chipman, and S. C. McClain (2013), The Airborne Multiangle SpectroPolarimetric Imager (AirMSPI): a new tool for aerosol and cloud remote sensing, *Atmospheric Measurement Techniques*, *6*(8), 2007–2025, doi:10.5194/amt-6-2007-2013.

Donner, L. J., B. L. Wyman, R. S. Hemler, L. W. Horowitz, Y. Ming, M. Zhao, J.-C. Golaz, P. Ginoux, S. J. Lin, M. D. Schwarzkopf, J. Austin, G. Alaka, W. F. Cooke, T. L. Delworth, S. M. Freidenreich, C. T. Gordon, S. M. Griffies, I. M. Held, W. J. Hurlin, S. A. Klein, T. R. Knutson, A. R. Langenhorst, H.-C. Lee, Y. Lin, B. I. Magi, S. L. Malyshev, P. C. D. Milly, V. Naik, M. J. Nath, R. Pincus, J. J. Ploshay, V. Ramaswamy, C. J. Seman, E. Shevliakova, J. J. Sirutis, W. F. Stern, R. J. Stouffer, R. J. Wilson, M. Winton, A. T. Wittenberg, and F. Zeng (2011), The Dynamical Core, Physical Parameterizations, and Basic Simulation Characteristics of the Atmospheric Component AM3 of the GFDL Global Coupled Model CM3, *Journal of Climate*, *24*(13), 3484–3519, doi:10.1175/2011JCLI3955.1.

Feingold, G., I. Koren, H. Wang, H. Xue, and W. A. Brewer (2010), Precipitation-generated oscillations in open cellular cloud fields, *Nature*, *466*(7308), 849–852, doi:doi:10.1038/nature09314.

Fridlind, A. M., and A. S. Ackerman (2011), Estimating the Sensitivity of Radiative Impacts of Shallow, Broken Marine Clouds to Boundary Layer Aerosol Size Distribution Parameter Uncertainties for Evaluation of Satellite Retrieval Requirements, *Journal of Atmospheric and Oceanic Technology*, *28*(4), 530–538, doi:10.1175/2010JTECHA1520.1.

Gerber, H., G. Frick, S. P. Malinowski, J. L. Brenguier, and F. Burnet (2005), Holes and entrainment in stratocumulus., *Journal of the Atmospheric Sciences*, *62*(2).

Gerber, H., G. Frick, S. P. Malinowski, and H. Jonsson (2013), Entrainment in Unbroken stratocumulus, *Journal of Geophysical Research: Atmospheres*.

Hansen, J. E., and L. D. Travis (1974), Light scattering in planetary atmospheres, *Space Science Reviews*, *16*(4), 527–610.

Henrich, F., H. Siebert, E. Jäkel, R. A. Shaw, and M. Wendisch (2010), Collocated measurements of boundary layer cloud microphysical and radiative properties: A feasibility study, *Journal of Geophysical Research: Atmospheres (1984–2012)*, *115*(D24), 685, doi:10.1029/2010JD013930.

IPCC (2013), Climate Change: The Assessment Reports of the Intergovernmental Pane on Climate Change.

Jiang, J. H. (2009), Aerosol-CO Relationship and Aerosol Effect on Ice Cloud Particle Size: Analyses from Aura MLS and Aqua MODIS Observations, *Journal of Geophysical Research*, pp. 1–30.

Jiang, J. H., H. Su, C. Zhai, V. S. Perun, A. Del Genio, L. S. Nazarenko, L. J. Donner, L. Horowitz, C. Seman, J. Cole, A. Gettelman, M. A. Ringer, L. Rotstayn, S. Jeffrey, T. Wu, F. Brient, J.-L. Dufresne, H. Kawai, T. Koshiro, M. Watanabe, T. S. L'Ecuyer, E. M. Volodin, T. Iversen, H. Drange, M. D. S. Mesquita, W. G. Read, J. W. Waters, B. Tian, J. Teixeira, and G. L. Stephens (2012), Evaluation of cloud and water vapor simulations in CMIP5 climate models using NASA "A-Train" satellite observations, *Journal of Geophysical Research: Atmospheres*, *117*(D14), D14,105, doi:10.1029/2011JD017237.

Kaufman, Y., I. Koren, L. Remer, and D. Rosenfeld (2005), The effect of smoke, dust, and pollution aerosol on shallow cloud development over the . . . , *Proceedings of the National Academy of Sciences*.

Kay, J. E., B. R. Hillman, S. A. Klein, Y. Zhang, B. Medeiros, R. Pincus, A. Gettelman, B. Eaton, J. Boyle, R. Marchand, and T. P. Ackerman (2012), Exposing Global Cloud Biases in the Community Atmosphere Model (CAM) Using Satellite Observations and Their Corresponding Instrument Simulators, *Journal of Climate*, *25*(15), 5190–5207, doi:10.1175/JCLI-D-11-00469.1.

King, M. D., W. P. Menzel, Y. J. Kaufman, D. Tanré, B.-C. Gao, S. Platnick, S. A. Ackerman, L. A. Remer, R. Pincus, and P. A. Hubanks (2003), Cloud and aerosol

properties, precipitable water, and profiles of temperature and water vapor from MODIS, *IEEE Transactions on Geoscience and Remote Sensing*, *41*(2), 442–458, doi:10.1109/TGRS.2002.808226.

Klein, S. A., and D. L. Hartmann (1993), The Seasonal Cycle of Low Stratiform Clouds, *Journal of Climate*, *6*(8), 1587–1606, doi:10.1175/1520-0442(1993)006⟨1587:TSCOLS⟩2.0.CO;2.

Kolmogorov, A. N. (1941), The local structure of turbulence in incompressible viscous fluid for very large Reynolds numbers, *Dokl Akad Nauk SSSR*.

Koren, I., and G. Feingold (2013), Adaptive behavior of marine cellular clouds, *Scientific Reports*, *3*, –, doi:doi:10.1038/srep02507.

Kubar, T. L., and D. L. Hartmann (2009), Understanding the importance of microphysics and macrophysics for warm rain in marine low clouds. Part II: Heuristic models of rain formation, *Journal of the Atmospheric ...*, doi:10.1175/2009JAS3071.1.

Latham, J., and R. L. Reed (1977), Laboratory studies of the effects of mixing on the evolution of cloud droplet spectra, *Quarterly Journal of the Royal Meteorological Society*, *103*(436), 297–306, doi:10.1002/qj.49710343607.

Lebsock, M., and H. Su (2014), Application of Active Spaceborne Remote Sensing for Understanding Biases Between Passive Cloud Water Path Retrievals, *Journal of Geophysical Research: Atmospheres*, pp. n/a–n/a, doi:10.1002/2014JD021568.

Lebsock, M. D., G. L. Stephens, and C. Kummerow (2008), Multisensor satellite observations of aerosol effects on warm clouds, *Journal of Geophysical Research: Atmospheres*, *113*(D15), doi:10.1029/2008JD009876.

Liang, L., L. Di Girolamo, and S. Platnick (2009), View-angle consistency in reflectance, optical thickness and spherical albedo of marine water-clouds over the northeastern Pacific through MISR-MODIS fusion, *Geophysical Research Letters*, *36*(9), L09,811, doi:10.1029/2008GL037124.

Liu, Y., and D. J. Diner (2017), Multi-Angle Imager for Aerosols, *Public Health Reports*, *132*(1), 14–17, doi:10.1177/0033354916679983.

Loeb, N. G., and R. Davies (1996), Observational evidence of plane parallel model biases: Apparent dependence of cloud optical depth on solar zenith angle, *Journal of Geophysical Research: Atmospheres (1984–2012)*, *101*(D1), 1621–1634, doi:10.1029/95JD03298.

Logan, N. A. (1965), Survey of some early studies of the scattering of plane waves by a sphere, *Proceedings of the IEEE*, *53*(8), 773–785, doi:10.1109/PROC.1965.4055.

Lohmann, U., P. Stier, C. Hoose, S. Ferrachat, S. Kloster, E. Roeckner, and J. Zhang

(2007), Cloud microphysics and aerosol indirect effects in the global climate model ECHAM5-HAM, *Atmospheric Chemistry and Physics*, *7*(13), 3425–3446, doi:10.5194/acp-7-3425-2007.

Lovejoy, S. (1982), Area-perimeter relation for rain and cloud areas, *Science*, *216*(4542), 185–187.

Marbach, T., P. Phillips, A. Lacan, and P. Schlussel (2013), The 3MI Mission: Multi-Viewing -Channel -Polarisation Imager of the EUMETSAT Polar System - Second Generation (EPS-SG) dedicated to aerosol and cloud monitoring, in *Sensors, Systems, and Next-Generation Satellites XVII*, p. 88890I, International Society for Optics and Photonics, doi:10.1117/12.2028221.

Marshak, A., and A. B. Davis (2005), *3D Radiative Transfer in Cloudy Atmospheres*, Physics of Earth and Space Environments, Springer-Verlag, Berlin/Heidelberg, doi:10.1007/3-540-28519-9.

Marshak, A., A. Davis, W. Wiscombe, and R. Cahalan (1995), Radiative smoothing in fractal clouds, *Journal of Geophysical Research: Atmospheres (1984–2012)*, *100*(D12), 26,247–26,261, doi:10.1029/95JD02895.

Marshak, A., L. Oreopoulos, A. B. Davis, W. J. Wiscombe, and R. F. Cahalan (1999), Horizontal radiative fluxes in clouds and accuracy of the independent pixel approximation at absorbing wavelengths, *Geophysical Research Letters*, *26*(11), 1585–1588, doi:10.1029/1999GL900306.

Marshak, A., S. Platnick, T. Várnai, G. Wen, and R. F. Cahalan (2006), Impact of three-dimensional radiative effects on satellite retrievals of cloud droplet sizes, *Journal of Geophysical Research: Atmospheres*, *111*(D9), D09,207, doi:10.1029/2005JD006686.

Martin, G. M., D. W. Johnson, and A. Spice (1994), The measurement and parameterization of effective radius of droplets in warm stratocumulus clouds, *Journal of the Atmospheric Sciences*, *51*(13), 1823–1842.

Martins, J. V., R. Fernandez-Borda, B. McBride, R. Espinosa, and L. Remer (2017), Combination between in-situ and remote sensing of tropospheric aerosols, in *The 16th Electromagnetic Light Scattering Conference*, College Park, MD.

Meyer, K., S. Platnick, L. Oreopoulos, and D. Lee (2013), Estimating the direct radiative effect of absorbing aerosols overlying marine boundary layer clouds in the southeast Atlantic using MODIS and CALIOP, *Journal of Geophysical Research: Atmospheres*, *118*(10), 4801–4815, doi:10.1002/jgrd.50449.

Mie, G. (1908), Beiträge zur Optik trüber Medien, speziell kolloidaler Metallösungen, *Annalen der Physik*, *330*(3), 377–445, doi:10.1002/andp.19083300302.

Miles, N. L., J. Verlinde, and E. E. Clothiaux (2000), Cloud Droplet Size Distri-

butions in Low-Level Stratiform Clouds, *Journal of the Atmospheric Sciences*, *57*(2), 295–311, doi:10.1175/1520-0469(2000)057⟨0295:CDSDIL⟩2.0.CO;2.

Miller, D. J., Z. Zhang, A. S. Ackerman, S. Platnick, and B. A. Baum (2016), The impact of cloud vertical profile on liquid water path retrieval based on the bispectral method: A theoretical study based on large-eddy simulations of shallow marine boundary layer clouds, *Journal of Geophysical Research: Atmospheres*, *121*(8), 4122–4141, doi:10.1002/2015JD024322.

Min, M., and Z. Zhang (2014), On the influence of cloud fraction diurnal cycle and sub-grid cloud optical thickness variability on all-sky direct aerosol radiative forcing, *Journal of Quantitative Spectroscopy and Radiative Transfer*, *142*, 25–36, doi:10.1016/j.jqsrt.2014.03.014.

Mishchenko, M. I., B. Cairns, L. D. Travis, G. Kopp, C. F. Schueler, B. A. Fafaul, R. J. Hooker, H. B. Maring, T. Itchkawich, J. E. Hansen, G. Kopp, C. F. Schueler, B. A. Fafaul, R. J. Hooker, H. B. Maring, and T. Itchkawich (2007), Accurate Monitoring of Terrestrial Aerosols and Total Solar Irradiance: Introducing the Glory Mission, *dx.doi.org*, *88*(5), 677–691, doi:10.1175/BAMS-88-5-677.

Nakajima, T., and M. D. King (1990), Determination of the Optical Thickness and Effective Particle Radius of Clouds from Reflected Solar Radiation Measurements. Part I: Theory, *Journal of the Atmospheric Sciences*, *47*(15), 1878–1893, doi:10.1175/1520-0469(1990)047⟨1878:dototа⟩2.0.co;2.

Nicholls, S., and J. Leighton (1986), An observational study of the structure of stratiform cloud sheets: Part I. Structure, *Quarterly Journal of the Royal Meteorological Society*, *112*(472), 431–460, doi:10.1002/qj.49711247209.

Noble, S. R., and J. G. Hudson (2015), MODIS comparisons with northeastern Pacific in situ stratocumulus microphysics, *Journal of Geophysical Research: Atmospheres*, *120*(16), 8332–8344, doi:10.1002/2014JD022785.

Oreopoulos, L., and R. Davies (1998), Plane parallel albedo biases from satellite observations. Part I: Dependence on resolution and other factors, *Journal of Climate*, *11*(5), 919–932.

Oreopoulos, L., and S. Platnick (2008), Radiative susceptibility of cloudy atmospheres to droplet number perturbations: 2. Global analysis from MODIS, *Journal of Geophysical Research: Atmospheres (1984–2012)*, *113*(D14), 4042, doi:10.1029/2007JD009655.

Oreopoulos, L., A. Marshak, R. F. Cahalan, and G. Wen (2000), Cloud three-dimensional effects evidenced in Landsat spatial power spectra and autocorrelation functions, *Journal of Geophysical Research: Atmospheres (1984–2012)*, *105*(D11), 14,777–14,788, doi:10.1029/2000JD900153.

Pincus, R., S. Platnick, S. A. Ackerman, R. S. Hemler, and R. J. Patrick Hofmann

(2012), Reconciling Simulated and Observed Views of Clouds: MODIS, ISCCP, and the Limits of Instrument Simulators, *Journal of Climate*, *25*(13), 4699–4720, doi:10.1175/JCLI-D-11-00267.1.

Platnick, S. (2000), Vertical photon transport in cloud remote sensing problems, *Journal of Geophysical Research: Atmospheres (1984–2012)*, *105*(D18), 22,919–22,935.

Platnick, S., M. D. King, S. A. Ackerman, W. P. Menzel, B. A. Baum, J. C. Riedi, and R. A. Frey (2003), The MODIS cloud products: algorithms and examples from terra, *IEEE Transactions on Geoscience and Remote Sensing*, *41*(2), 459–473, doi:10.1109/TGRS.2002.808301.

Pontikis, C. A. (1996), Parameterization of the droplet effective radius of warm layer clouds, *Geophysical Research Letters*, *23*(19), 2629–2632, doi:10.1029/96GL02452.

Pontikis, C. A., and E. M. Hicks (1993), Droplet Activation as Related to Entrainment and Mixing in Warm Tropical Maritime Clouds, *Journal of the Atmospheric Sciences*, *50*(13), 1888–1896, doi:10.1175/1520-0469(1993)050⟨1888:DAARTE⟩2.0.CO;2.

Pruppacher, H. R., and J. D. Klett (1978), Diffusion Growth and Evaporation of Water Drops and Ice Crystals, in *Microphysics of Clouds and Precipitation*, pp. 412–463, Springer Netherlands, Dordrecht, doi:10.1007/978-94-009-9905-3_13.

Quaas, J., and O. Boucher (2005), Constraining the first aerosol indirect radiative forcing in the LMDZ GCM using POLDER and MODIS satellite data, *Geophysical Research Letters*.

Quaas, J., Y. Ming, S. Menon, T. Takemura, M. Wang, J. E. Penner, A. Gettelman, U. Lohmann, N. Bellouin, O. Boucher, A. M. Sayer, G. E. Thomas, A. McComiskey, G. Feingold, C. Hoose, J. E. Kristjánsson, X. Liu, Y. Balkanski, L. J. Donner, P. A. Ginoux, P. Stier, B. Grandey, J. Feichter, I. Sednev, S. E. Bauer, D. Koch, R. G. Grainger, A. Kirkev aring g, T. Iversen, Ø. Seland, R. Easter, S. J. Ghan, P. J. Rasch, H. Morrison, J. F. Lamarque, M. J. Iacono, S. Kinne, and M. Schulz (2009), Aerosol indirect effects – general circulation model intercomparison and evaluation with satellite data, *Atmospheric Chemistry and Physics*, *9*(22), 8697–8717, doi:10.5194/acp-9-8697-2009.

Roebeling, R. A., A. J. Feijt, and P. Stammes (2006), Cloud property retrievals for climate monitoring: Implications of differences between Spinning Enhanced Visible and Infrared Imager (SEVIRI) on METEOSAT-8 and Advanced Very High Resolution Radiometer (AVHRR) on NOAA-17, *Journal of Geophysical Research: Atmospheres (1984–2012)*, *111*(D20), D20,210, doi:10.1029/2005JD006990.

Rosenfeld, D., G. Liu, X. Yu, Y. Zhu, J. Dai, X. Xu, and Z. Yue (2014), High-resolution (375 m) cloud microstructure as seen from the NPP/VIIRS

satellite imager, *Atmospheric Chemistry and Physics*, *14*(5), 2479–2496, doi:10.5194/acp-14-2479-2014.

Salby, M. L. (1996), Fundamentals of atmospheric physics.

Schröder, M., R. Bennartz, J. Fischer, and T. Ruhtz (2004), Airborne remote sensing of cloud radiative smoothing during the Baltex Bridge Cloud campaign, *Atmospheric Research*, *72*(1-4), 107–127, doi:10.1016/j.atmosres.2004.03.011.

Schutgens, N., and R. A. Roebeling (2009), Validating the validation: the influence of liquid water distribution in clouds on the intercomparison of satellite and surface observations, *Journal of Atmospheric and Oceanic Technology*, *26*(8), 1457–1474, doi:10.1175/2009jtecha1226.1.

Seethala, C., and Á. Horváth (2010), Global assessment of AMSR-E and MODIS cloud liquid water path retrievals in warm oceanic clouds, *Journal of Geophysical Research: Atmospheres*, *115*(D13), D13,202, doi:10.1029/2009JD012662.

Shaw, R. A. (2003), Particle-turbulence interactions in atmospheric clouds, *Annual Review of Fluid Mechanics*, *35*(1), 183–227, doi:10.1146/annurev.fluid.35.101101.161125.

Slingo, A., S. Nicholls, and J. Schmetz (1982), Aircraft observations of marine stratocumulus during JASIN, *Quarterly Journal of the Royal Meteorological Society*, *108*(458), 833–856, doi:10.1002/qj.49710845807.

Stamnes, K., S.-C. Tsay, W. Wiscombe, and K. Jayaweera (1988), Numerically stable algorithm for discrete-ordinate-method radiative transfer in multiple scattering and emitting layered media, *Applied Optics*, *27*(12), 2502–2509, doi:10.1364/AO.27.002502.

Stephens, G. L., and C. D. Kummerow (2007), The Remote Sensing of Clouds and Precipitation from Space: A Review, *Journal of the Atmospheric Sciences*, *64*(11), 3742–3765, doi:10.1175/2006JAS2375.1.

Stevens, B., A. S. Ackerman, and B. A. Albrecht (2001), Simulations of trade wind cumuli under a strong inversion, *Journal of the Atmospheric Sciences*, *58*(14), 1870–1891, doi:10.1175/1520-0469(2001)058⟨1870:sotwcu⟩2.0.co;2.

Stevens, B., D. H. Lenschow, G. Vali, H. Gerber, A. Bandy, B. Blomquist, J. L. Brenguier, C. S. Bretherton, F. Burnet, T. Campos, S. Chai, I. Faloona, D. Friesen, S. Haimov, K. Laursen, D. K. Lilly, S. M. Loehrer, S. P. Malinowski, B. Morley, M. D. Petters, D. C. Rogers, L. Russell, V. Savic-Jovcic, J. R. Snider, D. Straub, M. J. Szumowski, H. Takagi, D. C. Thornton, M. Tschudi, C. Twohy, M. Wetzel, and M. C. van Zanten (2003), Dynamics and chemistry of marine stratocumulus–DYCOMS-II, *Bulletin of the American Meteorological Society*, *84*(5), 579–593, doi:10.1175/BAMS-84-5-579.

Stevens, B., C.-H. Moeng, A. S. Ackerman, C. S. Bretherton, A. Chlond, S. de Roode, J. Edwards, J.-C. Golaz, H. Jiang, M. Khairoutdinov, M. P. Kirkpatrick, D. C. Lewellen, A. Lock, F. Müller, D. E. Stevens, E. Whelan, and P. Zhu (2005), Evaluation of Large-Eddy Simulations via Observations of Nocturnal Marine Stratocumulus, *Monthly Weather Review*, *133*(6), 1443–, doi:10.1175/MWR2930.1.

Suzuki, K., G. L. Stephens, S. C. van den Heever, and T. Y. Nakajima (2011), Diagnosis of the Warm Rain Process in Cloud-Resolving Models Using Joint CloudSat and MODIS Observations, *dx.doi.org*, doi:10.1175/JAS-D-10-05026.1.

Szczodrak, M., P. H. Austin, and P. B. Krummel (2001), Variability of Optical Depth and Effective Radius in Marine Stratocumulus Clouds, *Journal of the Atmospheric Sciences*, *58*(19), 2912–2926, doi:10.1175/1520-0469(2001)058⟨2912:VOODAE⟩2.0.CO;2.

Tampieri, F., and C. Tomasi (1976), Size distribution models of fog and cloud droplets in terms of the modified gamma function, *Tellus*, *28*(4), 333–347, doi:10.1111/j.2153-3490.1976.tb00682.x.

Thomas, G. E., and K. Stamnes (1999), Radiative Transfer in the Atmosphere and Ocean, Cambridge University Press, Cambridge, doi:10.1017/cbo9780511613470.

Twomey, S. (1977), The Influence of Pollution on the Shortwave Albedo of Clouds, *Journal of the Atmospheric Sciences*, *34*(7), 1149–1152, doi:10.1175/1520-0469(1977)034⟨1149:TIOPOT⟩2.0.CO;2.

van de Hulst, H. (1980), Multiple light scattering: tables, formulas and applications.

Várnai, T., and R. Davies (1999), Effects of cloud heterogeneities on shortwave radiation: Comparison of cloud-top variability and internal heterogeneity, *Journal of the Atmospheric Sciences*, *56*(24), 4206–4224.

Várnai, T., and A. Marshak (2001), Statistical Analysis of the Uncertainties in Cloud Optical Depth Retrievals Caused by Three-Dimensional Radiative Effects, *Journal of the Atmospheric Sciences*, *58*(12), 1540–1548, doi:10.1175/1520-0469(2001)058⟨1540:SAOTUI⟩2.0.CO;2.

Várnai, T., and A. Marshak (2002a), Observations of three-dimensional radiative effects that influence MODIS cloud optical . . . , *Journal of the Atmospheric Sciences*.

Várnai, T., and A. Marshak (2002b), Observations of three-dimensional radiative effects that influence MODIS cloud optical thickness retrievals, *Journal of the Atmospheric Sciences*, *59*(9), 1607–1618, doi:10.1175/1520-0469(2002)059⟨1607:ootdre⟩2.0.co;2.

Wallace, J. M., and P. V. Hobbs (2006), Atmospheric science: an introductory survey.

Wang, H., and G. Feingold (2009), Modeling Mesoscale Cellular Structures and Drizzle in Marine Stratocumulus. Part I: Impact of Drizzle on the Formation and Evolution of Open Cells, *Journal of the Atmospheric Sciences*, *66*(11), 3237–3256, doi:10.1175/2009JAS3022.1.

Wang, Z., S. Cui, J. Yang, H. Gao, C. Liu, and Z. Zhang (2017), A novel hybrid scattering order-dependent variance reduction method for Monte Carlo simulations of radiative transfer in cloudy atmosphere, *Journal of Quantitative Spectroscopy and Radiative Transfer*, *189*(C), 283–302, doi:10.1016/j.jqsrt.2016.12.002.

Warren, S., C. Hahn, J. London, R. Chervin, and R. Jenne (1988), Global distribution of total cloud cover and cloud type amounts over the ocean, *Tech. rep.*

Wendisch, M., and P. Yang (2012), Theory of atmospheric radiative transfer.

Werner, F., H. Siebert, P. Pilewskie, T. Schmeissner, R. A. Shaw, and M. Wendisch (2013), New airborne retrieval approach for trade wind cumulus properties under overlying cirrus, *Journal of Geophysical Research: Atmospheres*, *118*(9), 3634–3649, doi:10.1002/jgrd.50334.

Wilcox, E. M. (2012), Direct and semi-direct radiative forcing of smoke aerosols over clouds, *Atmospheric Chemistry and Physics*, *12*(1), 139–149, doi:10.5194/acp-12-139-2012.

Wiscombe, W. J. (1979), *Mie scattering calculations: Advances in technique and fast, vector-speed computer codes, NCAR Tech*, National Center for Atmospheric Research, Boulder, Colorado.

Wood, R. (2012), Stratocumulus clouds, *Monthly Weather Review*, *140*(8), 2373–2423, doi:10.1175/MWR-D-11-00121.1.

Wood, R., and D. L. Hartmann (2006), Spatial variability of liquid water path in marine low cloud: The importance of mesoscale cellular convection, *19*(9), 1748–1764, doi:10.1175/JCLI3702.1.

Zhang, M. H., W. Y. Lin, S. A. Klein, J. T. Bacmeister, S. Bony, R. T. Cederwall, A. D. Del Genio, J. J. Hack, N. G. Loeb, U. Lohmann, P. Minnis, I. Musat, R. Pincus, P. Stier, M. J. Suarez, M. J. Webb, J. B. Wu, S. C. Xie, M. S. Yao, and J. H. Zhang (2005), Comparing clouds and their seasonal variations in 10 atmospheric general circulation models with satellite measurements, *Journal of Geophysical Research: Atmospheres (1984–2012)*, *110*(D15), 1–308, doi:10.1029/2004JD005021.

Zhang, Z., and S. Platnick (2011), An assessment of differences between cloud effective particle radius retrievals for marine water clouds from three MODIS spectral bands, *Journal of Geophysical Research: Atmospheres*, *116*(D20), D20,215, doi:10.1029/2011JD016216.

Zhang, Z., S. Platnick, P. Yang, A. K. Heidinger, and J. M. Comstock (2010), Effects of ice particle size vertical inhomogeneity on the passive remote sensing of ice clouds, *Journal of Geophysical Research: Atmospheres (1984–2012)*, *115*(D17), doi:10.1029/2010JD013835.

Zhang, Z., A. S. Ackerman, G. Feingold, S. Platnick, R. Pincus, and H. Xue (2012), Effects of cloud horizontal inhomogeneity and drizzle on remote sensing of cloud droplet effective radius: Case studies based on large-eddy simulations, *Journal of Geophysical Research: Atmospheres*, *117*(D19), n/a–n/a, doi:10.1029/2012JD017655.

Zhang, Z., K. Meyer, S. Platnick, L. Oreopoulos, D. Lee, and H. Yu (2013), A novel method for estimating shortwave direct radiative effect of above-cloud aerosols using CALIOP and MODIS data, *Atmospheric Measurement Techniques Discussions*, *6*(6), 9993–10,020, doi:10.5194/amtd-6-9993-2013.

Zhang, Z., F. Werner, H. M. Cho, and G. Wind (2016a), A framework based on 2-D Taylor expansion for quantifying the impacts of subpixel reflectance variance and covariance on cloud optical thickness and effective ..., *Journal of ...*, doi:10.1063/1.4975502.

Zhang, Z., F. Werner, D. Miller, S. Platnick, A. Ackerman, L. DiGirolamo, K. Meyer, A. Marshak, G. Wind, and G. Zhao (2016b), *Progress in Understanding the Impacts of 3-D Cloud Structure on MODIS Cloud Property Retrievals for Marine Boundary Layer Clouds*.

Zhou, C., M. D. Zelinka, A. E. Dessler, and P. Yang (2013), An Analysis of the Short-Term Cloud Feedback Using MODIS Data, *Journal of Climate*, *26*(13), 4803–4815, doi:10.1175/JCLI-D-12-00547.1.

Zinner, T., G. Wind, S. Platnick, and A. S. Ackerman (2010), Testing remote sensing on artificial observations: impact of drizzle and 3-D cloud structure on effective radius retrievals, *Atmospheric Chemistry and Physics*, *10*(19), 9535–9549, doi:10.5194/acp-10-9535-2010.